



# Sub-micrometre texturing of silicon heterojunction bottom cell for Perovskite-Silicon tandem application

Laxmi Narasimha Raju Pusapati

# Sub-micrometre texturing of silicon heterojunction bottom cell for Perovskite-Silicon tandem application

by

Laxmi Narasimha Raju Pusapati

in partial fulfilment of the requirements for the degree of  
**Master of science**  
in Sustainable Energy Technology  
at the Delft University of Technology,  
to be defended publicly on Wednesday ,August 30, 2023 at 9:30.

Student number:	5549361
Thesis committee:	
Prof.dr. Olindo Isabella	TU Delft, ESE-PVMD, Supervisor
Prof.dr. Ferdinand Grozema	TU Delft, Grozema group, Professor
Dr.ir. Rene van Swaaij	TU Delft, ESE-PVMD, Associate Professor
Ir. Yifeng Zhao	TU Delft, ESE-PVMD, Daily supervisor
Ir. Katarina Kovacevic,	TU Delft, ESE-PVMD, Daily Supervisor

An electronic version of this thesis is available at <http://repository.tudelft.nl/>.



# Acknowledgements

It has been an incredible pleasure to do my thesis with the PVMD group. Their generous support to explore a variety of ideas within the framework of this thesis has been a wonderful learning experience. Working in the clean-room has been a demanding and exciting experience.

I would like to express my profound gratitude to Dr. Olindo Isabella, Ir. Yifeng Zhao, and Ir. Katarina Kovacevic for their time and support. Their advice and recommendations were quite helpful in improving this work. Their continuous support has been extremely motivating during difficult times while performing experiments.

I also want to thank Hande Aydogmus for all of her help at the polymer lab at the Else Kooi Laboratory (EKL) and Dr. Paula Perez Rodriguez for the AFM equipment training. In addition, I would like to thank Charles de Boer, Brian van den Bulk, Anja van Langen-Suurling, Roald van der Kolk and Chris Soukras (Ph.D. Conessa Boj Lab) for their instructions and insightful suggestions about the use of lithography, dry etching, and wet bench tools at the Kavli Institute of Nanoscience, Delft.

Finally, the past few months spent working on my master's thesis have been both challenging and thrilling. I owe an immense amount of gratitude to my friends and family for their unwavering encouragement, which enabled me to persevere and complete this Master's journey with many treasured memories.

*LNR Pusapati*  
Delft, August 2023

# Abstract

The photovoltaic (PV) market is currently dominated by crystalline silicon (c-Si) technology, which accounts for 95% of the production. However, the record single-junction c-Si solar cell has achieved a record efficiency of 26.81% approaching the theoretical efficiency limit of 29.43%. In an effort to overcome this barrier, multi-junction devices are being investigated, and perovskite/Si tandem technology is attracting a lot of interest. This is because it is compatible with well-established c-Si technology and is comparatively less expensive.

Recently, two-terminal (2T) monolithic tandem devices with a c-Si bottom cell and a perovskite top cell have achieved an impressive 33.7% efficiency. By utilizing a solution-based process it allows for fabricating high-quality perovskite layers. However, problems develop when the bottom cell's light trapping features exceed the thickness of the perovskite layer. To ensure uniform coverage of high-quality perovskite layer, the light trapping features must be lowered to sub-micrometre ( $< 1 \mu\text{m}$ ) height.

This thesis investigates three methods for creating sub-micron features on the c-Si bottom cell. The first two approaches include wet-chemical processing from the top-down and bottom-up techniques. Using a poly-Si etch solution, the top-down approach aims to lower the height of large surface features from 3-5  $\mu\text{m}$  to less than 1  $\mu\text{m}$ . This method resulted in substantial reflection losses and poor passivation due to surface-induced roughness, even though the peak height was lowered to 0.9  $\mu\text{m}$ . In order to tackle this issue, an additive was added to the mixture, producing a morphology with a 1.1  $\mu\text{m}$  lower peak height, compared to an initial peak height of 3  $\mu\text{m}$ . Further, the passivation has seen a two-fold increase in minority carrier lifetime. This increase is attributed to the reduced surface roughness that was inspected through SEM images. However, the surface still contained nano-scale features whose origination could be related to the cleaning procedure followed or the (i)a-Si:H layer growth.

The second method is a bottom-up approach and uses KOH,  $\text{K}_2\text{SiO}_3$ , and a surface additive to create sub-micron features on a flat Si wafer. Once the chemical concentrations were optimized, the peak height was effectively lowered to less than 0.8  $\mu\text{m}$  at an F-ratio of  $F = 2.0$ . But, this experiment is conducted at a temperature of 80° C. Many non-uniformities in pyramid distribution were observed as well as nano-scale roughness for F-ratio of  $F=0$ . This seemed to be resolved with better pyramid homogeneity and reduced nano-scale roughness by lowering the temperature to 70° C. While, maintaining a peak height below 0.8  $\mu\text{m}$  at  $F=2.0$ . Moreover, this approach also exhibited lower reflection losses which is close to reflection observed from large pyramidal features (3 $\mu\text{m}$ ).

The last method includes the use of lithography to produce 2D periodic inverted nano pyramids. This process flow showed that patterns with critical dimensions close to 100 nm may be transferred using high-throughput nano-imprinting lithography. By using a much rigid soft mold that did not showcase any pattern distortion. However, the limitations in mask opening created issues with the nano-pyramid formation. This further requires the optimization of suitable hard mask layers.

To sum up, these methods demonstrate the possibility of producing effective sub-micron features, which is promising for perovskite/Si tandem technological advancements.

# Contents

<b>Acknowledgements</b>	<b>i</b>
<b>Abstract</b>	<b>ii</b>
<b>1 Introduction</b>	<b>1</b>
1.1 c-Si based technology . . . . .	1
1.2 Deposition of perovskite layer: Challenges . . . . .	3
1.3 Thesis outline and research goals . . . . .	3
<b>2 Solar cell: Fundamentals</b>	<b>5</b>
2.1 Photovoltaics . . . . .	5
2.1.1 Working principle of a solar cell . . . . .	6
2.2 Energy conversion limits . . . . .	7
2.2.1 Fundametal losses . . . . .	7
2.2.2 Optical losses . . . . .	8
2.2.3 Recombination losses . . . . .	9
2.3 Multi junction devices . . . . .	10
2.3.1 Perovskite/Si tandem device . . . . .	10
2.4 Light propagation and behavior . . . . .	11
2.4.1 Imapct of surface morphology on light trapping . . . . .	11
2.4.2 Influence of interference and scattering . . . . .	13
2.4.3 Prospects of periodical nano textures . . . . .	14
<b>3 Processing and characterization of surface textures</b>	<b>18</b>
3.1 Plasma-based techniques for etching and deposition . . . . .	18
3.1.1 Plasma based etching . . . . .	18
3.1.2 Plasma based deposition . . . . .	20
3.2 Electron beam lithography . . . . .	21
3.3 Thermal Nano Imprint Lithography . . . . .	22
3.4 Chemical based etching technique . . . . .	23
3.4.1 Cleaning techniques . . . . .	25
3.5 Scanning electron microscopy . . . . .	26
3.6 Atomic force microscopy . . . . .	27
3.7 Spectrophotometry . . . . .	27
3.8 Photoconducatace lifetime measurement . . . . .	28
<b>4 Wet-chemical processing for varying surface morphology</b>	<b>30</b>
4.1 Poly-Si etching : Top-down approach . . . . .	30
4.1.1 Topographical characterization . . . . .	31
4.1.2 Optical characterization . . . . .	33
4.1.3 Passivisation testing . . . . .	34
4.1.4 HNA etching . . . . .	37
4.2 Creation of nano pyramids though chemical texturing . . . . .	41
4.2.1 Texturing process . . . . .	42
4.2.2 Effect of $K_2SiO_3$ . . . . .	44
4.2.3 Effect of additive concentration . . . . .	46
4.2.4 Effect of KOH+K <sub>2</sub> SiO <sub>3</sub> with surface additives . . . . .	49
4.2.5 Effect of temperature . . . . .	54
<b>5 Lithography technique to vary the surface morphology</b>	<b>58</b>
5.1 Introduction . . . . .	58
5.1.1 Nano-imprinting lithography . . . . .	59



---

5.2	Master mold fabrication . . . . .	60
5.2.1	Dry etching . . . . .	63
5.3	Thermal imprinting . . . . .	65
<b>6</b>	<b>Conclusions</b>	<b>69</b>
6.1	Poly-Si etching - Top-Down approach . . . . .	69
6.2	KOH + K <sub>2</sub> SiO <sub>3</sub> etching : Bottom up approach . . . . .	70
6.3	Nano imprinting lithography . . . . .	71
6.4	Outlook . . . . .	71
<b>A</b>	<b>Poly-Si etching</b>	<b>73</b>
<b>B</b>	<b>KOH + K<sub>2</sub>SiO<sub>3</sub></b>	<b>75</b>

# List of Figures

1.1	Forecast of market share of different solar cell technologies. Adapted from [3] . . . . .	2
1.2	The external quantum efficiency (EQE) comparison for SHJ (bottom-cell) (blue line) (a) and perovskite (Top-cell) (b) .Adapted from [7]. . . . .	2
1.3	Schematic of tandem devices considered for optical study by K.Jager [15] . . . . .	3
2.1	The unit cell of a diamond structure, depicting the crystal lattice of silicon. Adapted from [17] . . . . .	5
2.2	P-N junction formation with the contact of different semiconductors dopants. Adapted from [19] . . . . .	7
2.3	The fundamental losses for device with multiple junctions. Adapted from [6] . . . . .	8
2.4	Schematic representation of the different bulk recombination process. Adapted from [23]	10
2.5	Schematic of a two junction tandem device 4T configuration (left) and 2T configuration (right). Adapted from [24] . . . . .	11
2.6	Effect of light rays being reflected at the interface of a solar cell . . . . .	12
2.7	Schematic of upright pyramid (right) an inverted pyramid (left) with their respective lattice orientations. Adapted from [31] . . . . .	13
2.9	The effect of smaller pyramids on reflection illustrated through AID and weighted average reflectance measurements. Adapted from [36] . . . . .	14
2.8	Distribution of scattered light for Rayleigh and Mie phenomena. Daped from [32] . . .	15
2.10	Variation in LPE (a) and $J_{ph}$ enhancement (b) factors varying with grating size. Adapted from [39] . . . . .	16
2.11	Variation in current density with improving aspect ratio. Adapted from [40] . . . . .	17
3.1	Process of etching a substrate using CF <sub>4</sub> molecules. Adapted from [41] . . . . .	19
3.2	Schematic of CCP based RIE chamber (left) and ICP based RIE chamber (Right) [42] . .	19
3.3	Schematic of the PECVD tool used for (i)a:Si:H layer at EKL. Adapted from [46] . . . . .	20
3.4	Schematic representation of the SiH <sub>3</sub> reaction upon diffusion to the surface [45] . . . . .	21
3.5	Raith EBPg 5000+ . . . . .	22
3.6	Indication of equipment (Left) and process curve for Thermal imprinting (Right). . . . .	23
3.7	Schematic of Si bonding at different crystal orientations [100] (top) and [111] (bottom). Adapted from [57] . . . . .	24
3.8	Schematic of a general SEM column with different components. Adapted from [69] . . .	26
3.9	Schematic of the IS that measures the reflected and transmitted light by placing the sample at the front or backport of the sphere. Adapted from [38] . . . . .	28
3.10	Schematic of Sinton WCT-120 instrument setup. Adapted from [46]. . . . .	29
4.1	3D height of an AFM characterized LONGI CZ sample. . . . .	31
4.2	Top view inspection of 1.5 minutes poly-etched sample . . . . .	31
4.3	Variation in average peak height and RMS roughness for poly-etched wafers . . . . .	32
4.4	SEM inspection of 6 minutes poly-Si etched wafer, depicting the morphology at different instances of etching . . . . .	32
4.5	Reflectance measurement for poly-etched wafers at different etch timing . . . . .	33
4.6	Lifetime measurements for poly-etched (PE) and post-cleaned (PC) samples with varying etching time and thickness. . . . .	34
4.7	Cross-sectional SEM images of textured LONGI CZ wafers before cleaning (a) and after cleaning (b). . . . .	35
4.8	Cross-sectional SEM images of Poly-Si etched wafer after 1.5 minutes of etching, before cleaning (a) and after cleaning + passivation (b). . . . .	35

4.9	Cross-sectional SEM images of Poly-Si etched wafer after 6minutes of etching, before cleaning (a) and after cleaning + passivation (b). . . . .	36
4.10	Cross-sectional SEM images of Poly-Si etched wafer after 16 minutes of etching, before cleaning (a) and after cleaning + passivation (b). . . . .	37
4.11	Variation in peak height and RMS roughness for HNA etched wafers. . . . .	38
4.12	Reflectance measurement for HNA-etched wafers at different etch timing . . . . .	39
4.13	Lifetime measurements for HNA etched samples with 10nm bi-layer thickness. . . . .	39
4.14	Cross-sectional SEM images of HNA etched wafer after 1.5 minutes of etching, before cleaning (Left) and after cleaning + passivation (Right). . . . .	40
4.15	Cross-sectional SEM images of HNA etched wafer after 2 minutes of etching, before cleaning (Left) and after cleaning + passivation (Right). . . . .	40
4.16	Cross-sectional SEM images of Poly-Si etched wafer after 3 minutes of etching, before cleaning (Left) and after cleaning + passivation (Right). . . . .	41
4.17	Variation in peak height and RMS roughness for increasing $K_2SiO_3$ addition. . . . .	43
4.18	SEM inspection of surface morphology at different $K_2SiO_3$ concentrations. . . . .	43
4.19	SEM inspection of surface morphology at different $K_2SiO_3$ concentrations. . . . .	45
4.20	Weighted average reflectance variation for different F-ratio concentration. . . . .	45
4.21	Variation in peak height and RMS roughness at different additive concentrations. . . .	46
4.22	Variation in peak height at 5.5% additive (MTH 2.6) concentration. . . . .	47
4.23	Surface morphology inspection at different additive concentrations of 1.4% (a) and 2.4% (b) after 10 minutes of etching. . . . .	47
4.24	Surface morphology inspection for 5.5% additive concentration after 5 minutes of etching at lower magnification (a) and higher magnification (b). . . . .	48
4.25	Surface morphology inspection at 5.5% additive concentration after 20 minutes of etching at lower magnification (a) and higher magnification (b). . . . .	48
4.26	Weighted average reflectance variation for additive concentration of 1.4% and 2.4%. . . .	49
4.27	Optical and mean slope relation for 5.5% additive concentration at $F=0$ . . . . .	49
4.28	Variation in peak and height and RMS roughness at varying F-ratio and 5.5% additive concentration. . . . .	50
4.29	Surface morphology variations for $F=0.5$ , $80^\circ C$ after 5 minutes of etching at lower magnification (a) and higher magnification (b) and 20 minutes of etching at lower magnification (c) and higher magnification (d). . . . .	51
4.30	Surface morphology variations for $F=1.0$ , $80^\circ C$ after 5 minutes of etching at lower magnification (a) and higher magnification (b) and 20 minutes of etching at lower magnification (c) and higher magnification (d) . . . . .	51
4.31	Surface morphology variations for $F=1.5$ , $80^\circ C$ after 5 minutes of etching at lower magnification (a) and higher magnification (b) and 20 minutes of etching at lower magnification (c) and higher magnification (d). . . . .	52
4.32	Surface morphology variations for $F=2.0$ , $80^\circ C$ after 5 minutes of etching at lower magnification (a) and higher magnification (b) and 20 minutes of etching at at lower magnification (c) and higher magnification (d). . . . .	53
4.33	Weighted average reflectance and etching rate variations at different F-ratios . . . . .	54
4.34	Variation in peak and height and RMS roughness at $70C$ and $75C$ temperatures . . . . .	55
4.35	Surface morphology variations for $F=0$ at $75C$ . . . . .	55
4.36	Surface morphology variations for $F=0$ at $70C$ . . . . .	56
4.37	Surface morphology variations for $F=2.0$ at $70C$ . . . . .	56
4.38	Weighted average and etching rate variations at different F-ratios and temperature . . .	57
5.1	Process flow description for replication of nanometer scale features. Adapted from [87]	58
5.2	Schematic representation of a Lift-process used to fabricate master mold for nano imprinting. Adapted from [88] . . . . .	59
5.3	Process for fabrication of inverted nano pyramids using T-NIL technique. Adapted from [90] . . . . .	60
5.4	Schematic of process flow devised for fabricating Inverted nano-pyramids . . . . .	60
5.5	2D periodic gratings dosage test . . . . .	62
5.6	2D periodic gratings dosage test without any PEC . . . . .	62



5.7	Stress-induced deformation of resist sidewalls at 250W DC bias (a) and 150W DC bias (b).	64
5.8	RIE etching at 75W DC bias after 30s (a) and 2 minutes (b) of etching. . . . .	64
5.9	Inspection of the master mold after SiO <sub>2</sub> (a) and Si (b) etching. . . . .	65
5.10	PDMS mold inspected for a 900 nm periodic pattern . . . . .	65
5.11	Inspection of a hPDMS mold (Right) casted from the master mold (Left) . . . . .	66
5.12	Inspection of imprinted features onto to the substrate after TNIL . . . . .	67
5.13	Plasma descum process performed for 5s on the Si substrate top-view (left) and Cross-sectional (Right). . . . .	67
5.14	Lack of diffraction pattern on the Si substrate after chemical etching . . . . .	68
B.1	The variation in peak height at different KOH concetration . . . . .	75
B.2	Peak height variation for F=0 at MTH 3.5% surface additive . . . . .	76
B.3	SEM characterization of a wafer etched in F=1.0 at 80°C solution . . . . .	76
B.4	SEM characterization of a wafer etched in F=1.0 at 80°C solution . . . . .	76

# List of Tables

2.1	Theoretical efficiency predicted for different junction devices. [24]	10
3.1	Deposition parameters of i1 and i2 layers considered for a bilayer passivation	21
3.2	Chemical cleaning techniques indicating the contamination removed	25
4.1	Morphological parameters of the AFM characterized CZ-wafers	30
4.2	Effect of mean slope variation on weighted average reflectance	34
4.3	Effect of weighted average reflectance and mean slope variation for HNA etched sample	38
5.1	Etch rate (nm.min) of resist materials at different gas mixtures in dry-etching	61
5.2	Parameters used for RIE etching of SiO <sub>2</sub> , Si and resist	63
A.1	Morphological parameters for a 1.5 minutes poly-etched sample	73
A.2	Morphological parameters for a 6 minutes poly-etched sample	73
A.3	Morphological parameters for a 11 minutes poly-etched sample	73
A.4	Morphological parameters for a 16 minutes poly-etched sample	73
A.5	Morphological parameters for a 1.5 minutes HNA sample	74
A.6	Morphological parameters for a 2 minutes HNA sample	74
A.7	Morphological parameters for a 2.5 minutes HNA sample	74
A.8	Morphological parameters for a 3 minutes HNA sample	74
B.1	Peak height variation for F=0 at an additive concentration of 5.5%	77
B.2	Peak height variation for F=0.5 at an additive concentration of 5.5%	77
B.3	Peak height variation for F=1.0 at an additive concentration of 5.5%	77
B.4	Peak height variation for F=1.5 at an additive concentration of 5.5%	77
B.5	Peak height variation for F=2.0 at an additive concentration of 5.5%	77
B.6	Peak height variation for F=0 at an additive concentration of 5.5% and 75C temperature	77
B.7	Peak height variation for F=0 at an additive concentration of 5.5% and 70C temperature	78
B.8	Peak height variation for F=2.0 at an additive concentration of 5.5% and 75C temperature	78
B.9	Peak height variation for F=2.0 at an additive concentration of 5.5% and 75C temperature	78

# Introduction

Solar energy provides a promising path for harnessing a key source of energy, sunlight, satisfying our needs for heat and electricity sustainably. One method of transforming solar energy into electricity is through concentrated solar power, where the heat is extracted from sunlight helps drive a steam turbine. On the other, a direct conversion of sunlight to electricity is achieved through photovoltaic (PV) technology. Considering, the ultimate goal of this sustainable energy source lies in achieving cost parity with conventional fuel sources like coal and natural gas for power generation. It made photovoltaics (PV) emerge as a crucial alternative and its lower LCOE <sup>1</sup>, has gradually improved its competitiveness over the years [1]. Further, the developments made in PV technology to improve its performance led to the introduction of various new technologies which are classified into four generations[2].

1. **First generation** : Cell technologies related crystalline silicon and GaAs.
2. **Second generation** : Includes the development of thin-film PV cells, microcrystalline silicon, amorphous silicon, copper indium gallium selenide (CIGS) and Cadmium based technologies.
3. **Third generation** : It includes technologies which are primarily aimed to improve the performance and cost reductions of PV cells. By incorporating cells based on organic compounds, dye-sensitized solar cells, quantum dots, perovskites solar cells, concentrated solar and multijunction junction solar cells.
4. **Fourth generation** : It employs composite PV technology in which nano particles embedded in polymer layers produce a single multi-spectrum light absorption layer. This cell technique, also known as nano photovoltaics, currently remains a long way from commercialization.

The first-generation technology, c-Si, holds a significant market share with 95% of all solar cells being produced. However, it has a theoretical efficiency limit, which could reduce its capability to compete against traditional fossil fuel sources. Multijunction solar cells (a third generation of PV technology), such as perovskite/Si tandem devices offer a possible answer. Through this technology, different absorber layers in these cells collect different spectrum of light, allowing for a broader range of solar radiation absorption and more effective power generation. Together, the perovskite/Si tandem devices push the frontiers of PV technology, making them an appealing prospect for the PV industry.

Hence, this chapter will discuss in brief about c-Si based technologies and why Silicon Heterojunction Technology (SHJ) is the most suitable for application in a perovskite/Si tandem device. Followed by the current challenges in the upscaling of this technology. Finally, the aim to solve one of the aforementioned challenges will be discussed.

## 1.1. c-Si based technology

Though c-Si based technologies are dominating the PV market for a long time. The outlook for this PV technology over the coming years is illustrated in Figure 1.1, which showcases that TOPcon (Tunnel oxide Passivating contact) cell technology will have a majority of market share, followed by SHJ technology [3]. In comparison with other c-Si technologies, TOPcon offers high-temperature processing of its supporting

---

<sup>1</sup>LCOE of utility-scale Solar PV



layers, suitable for most depositions of  $\text{SnO}_2$  Electron Transport Layer (ETL) for a perovskite[4]. But, this cell utilizes a front dielectric stack for both passivation and anti-reflection coating. These layers create insulation, hindering the electrical connection with top cell. Many such issues persist in this technology making it less attractive for tandem integration when compared to its alternative silicon heterojunction solar cells (HJTs). This technology is being adapted for the Si bottom cell in most state-of-the-art tandem device fabrication due to its simplicity of manufacturing and significantly better integration with the top-cell (Perovskites).[4]

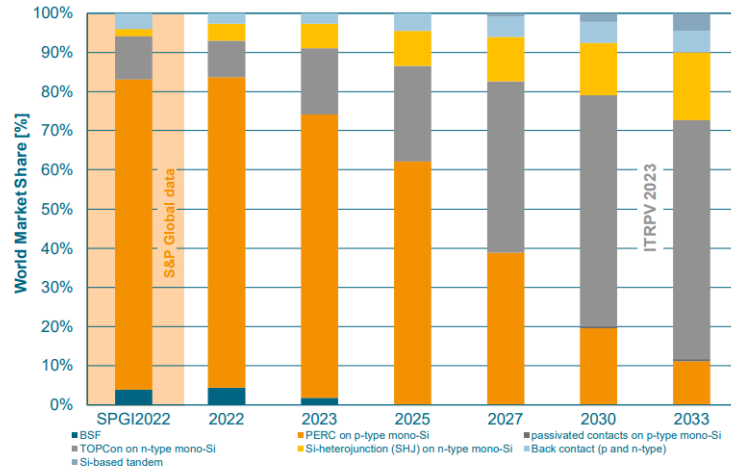


**Figure 1.1:** Forecast of market share of different solar cell technologies. Adapted from [3]

The current record-efficient SHJ solar cell, has an efficiency of 26.81% achieved by LONGI,[5] which is close to the theoretical efficiency limit of 29.43% [6]. This indicates the difficulty in further efficiency improvements considering the Shockley-Queisser Efficiency (SQE) limit of 29.4%, by considering the Auger recombination process (cite). This is where multi-junction devices offer a potential solution by implementing wider bandgap materials on the top and narrower bandgap materials on the bottom. This allows larger energy photons to be absorbed in the top sub-cell, leaving the sub-band gap photons to be utilized by the bottom cell. Therefore integration of this cell with the perovskite, which has a better bandgap tunability can provide efficient conversion of photons to electricity.

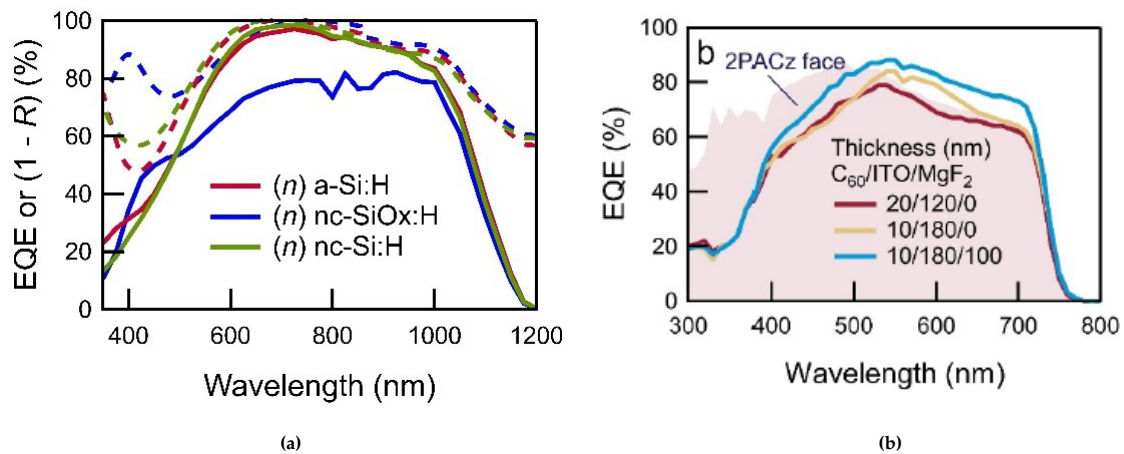


**Figure 1.2:** The external quantum efficiency (EQE) comparison for SHJ (bottom-cell) (blue line) (a) and perovskite (Top-cell) (b). Adapted from [7].

To better understand the effect of this bandgap variation in top and bottom cell a comparison of External Quantum Efficiency for perovskite and SHJ are provided as shown in Figure 1.2. Perovskite

(bandgap of 1.64-1.72 eV) donot indicate any absorption after a wavelength of 800 nm whereas SHJ as shown in Figure 1.2a shows good QE till a wavelength of 1200 nm. Apart from this, SHJ solar also has low parasitic absorption losses of the infrared light [8], this makes SHJ suitable for usage as the bottom cell in a tandem device. Foremost research on these cells using silicon heterojunction as the bottom sub-cell was conducted by the Albrecht group at Helmholtz-Zentrum Berlin (HZB) [9], which exhibited an efficiency of 18.1% and found that the bottom cell exhibits better infrared spectral response. Also, they performed these experiments in a low-temperature planar-perovskite solar using atomic layer deposition (ALD) grown SnO<sub>2</sub> electron transport layer, which is widely used in current champion devices.

## 1.2. Deposition of perovskite layer: Challenges

Over the years with several optical simulations and experiments the efficiency of PVK/Si tandem devices has steadily progressed. However, there still remain some challenges to be addressed to make this technology scalable to industrial production.

One, of the most crucial issue, is the deposition of a perovskite layer on top of a silicon bottom cell. In general silicon bottom cells are textured with pyramidal features that can reduce the reflection losses and provide higher current density. Implementing such features into tandem devices can further improve device performance [10].

However, the deposition of high-quality perovskites which is also necessary for better device performance can be achieved through solution-based techniques. Using them for deposition of the top layer on textures Si bottom cell has a drawback. The deposition of the perovskite layer needs to be conformal in order to avoid any shunting losses [4]. Since industrially processed textured c-Si solar cells have a texturing height in the range of 3-5  $\mu\text{m}$  [11]. The thickness of perovskite needs to be higher than the height of these features to uniformly cover the surface. But, most perovskites thin films are limited by their diffusion length, they have a thickness between 0.5 - 1  $\mu\text{m}$  [12]. This requires the height of textures present on Si bottom cell to be in the sub-micrometer range to allow high-quality perovskite layer deposition [13]. By implementing such features, the length of phonon path length in the perovskite absorber layer increases due to the reabsorption effect [14].

Moreover, an optical study performed by K.Jager [15] has modeled perovskite/Si tandem structures with different surface morphologies as shown in Figure 1.3. They showcased that a fully textured device will have a higher short-current density which directly correlates to the reduced reflection of light. In the process to achieve a fully-textured device, a rear texturing should be fabricated that can allow for a uniform coverage of the perovskite layer. This texturing could be achieved by considering the wet-chemical processing of creating pyramidal features on the c-Si substrate.[11].

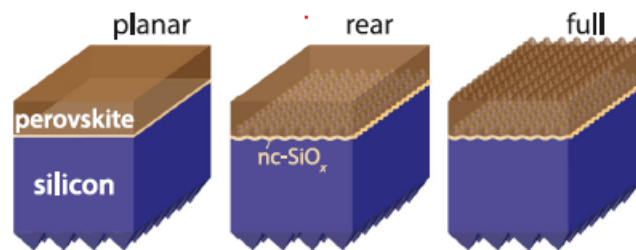


Figure 1.3: Schematic of tandem devices considered for optical study by K.Jager [15]

Apart from the above-mentioned challenge, there also exist other difficulties in the pathway of improving tandem device efficiency. Such as parasitic absorption, device stability, and optimal charge transport that require further optimization.

## 1.3. Thesis outline and research goals

As mentioned in the previous section 1.2, the challenge of creating textured morphology on a c-Si substrate. Based on this outline, the main objective was titled as *Optimization of surface morphology on silicon heterojunction bottom cell to allow for perovskite top cell deposition by solution-based techniques.*

It will involve investigating and experimenting in techniques that will allow for the reduction in height of textured features to less than 1  $\mu\text{m}$  which can aid in improving light trapping.

To achieve the desired texturing the following research goals will be addressed in this thesis:

1. Evaluate suitable wet-chemical processing technique for sub-micrometre light trapping features
  - (a) How can the existing textured samples be used for achieving smaller light-trapping features, through a top-down approach.
  - (b) How does the subsequent passivation layer development work for the top-down approach.
  - (c) Evaluating the effect of suitable chemicals that can provide a reduced etching rate for light trapping features on flat Si wafers.
  - (d) Understanding the etching kinetics and finding the suitable chemical concentrations that provide good nucleation and reduced peak height
2. Defining a process flow for the fabrication of 2D periodic inverted nano pyramids
  - (a) Evaluating suitable lithography techniques that can provide a reliable and high throughput for creating the periodic pattern
  - (b) Verify if the pattern transfer can be done using a photoresist mask, instead of a hard mask.

The structure devised to describe the texturing process and developments are as follows. First, in Chapter 2 fundamentals of solar cell operation and limitation will be presented. Alongside, an overview of the concept of light propagation and how it can differ to varying surface morphology will be discussed. Second, in Chapter 3 the experimental techniques used for characterizing and developing the textures will be presented. Third, in Chapter 4 the process development and surface morphological parameters of texturing achieved through wet-chemical processing will be presented along with the passivation tests performed. Fourth, in Chapter 5 fabrication of surface textures through the Nano-imprinting lithography technique will be presented. Finally, in Chapter 6 the conclusion and outlook will be discussed based on the obtained results.



# 2

## Solar cell: Fundamentals

It is crucial to understand the effect of implementing textured features onto a c-Si substrate. But, before this could be discussed, we need to understand the basic operation of a solar cell and why a tandem configuration is preferred.

### 2.1. Photovoltaics

The basic operation of solar cells is related to semiconductor device physics, since Si is the most widely utilized semiconductor material due to its abundance [16], we start by understanding its features before discussing the working principle of a solar cell.

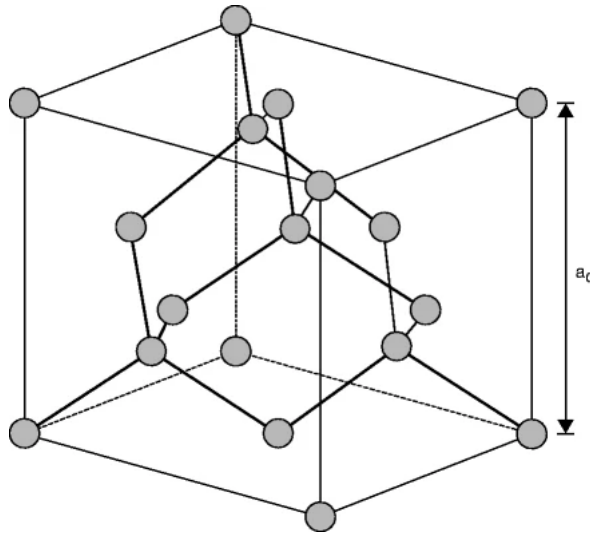


**Figure 2.1:** The unit cell of a diamond structure, depicting the crystal lattice of silicon. Adapted from [17]

Silicon (Si) being a part of the 4th group in a periodic table has 4 valence electrons, this provides it with an atomic arrangement as shown in 2.1 where each atom is bonded to four other atoms. This lattice structure is known as the diamond lattice and exhibits strong bonds. Further, Si exhibits energy bands, which are filled in the lower levels and empty at the top. The lower energy band is known as the valence band, whereas the higher energy band is known as the conduction band. When sunlight passes through the material, it causes the excitation of electrons into the conduction leaving holes behind, resulting in mobile/free electrons[18]. In general, the energy required for a free electron to be excited from valence to the conduction band is determined by the difference between the highest energy level of the valence band and the lowest energy of the conduction band, called the energy bandgap ( $E_g$ ). A detailed explanation of charge carrier generation will be provided in the next section.

However, the conduction and valence band energy levels fluctuate with crystal momentum. Where

the corresponding energy difference at the highest valence band and lowest conduction band is 1.12 eV. But, these energy levels of the conduction and valence bands are at distinct momentum levels. In such conditions, an electron must undergo a change in momentum caused by thermal vibrations in order to be excited. A phonon, which has a lower energy level and higher momentum than a photon, is absorbed by an electron in the lattice, allowing it to change momentum. [19]. This makes Si an indirect bandgap semiconductor compared to other materials like Ga which have a direct transition.

### 2.1.1. Working principle of a solar cell

The previous section provided an understanding of the energy required for an electron to be excited into the conduction band. It does not completely indicate the working of a solar cell. The main principle which governs the working of a solar cell is the Photovoltaic (PV) effect which was discovered by Becquerel in 1839, it is a process through which the PV cell utilizes the absorbed sunlight in the semiconductor material to generate potential difference. This potential difference is crucial to allow for the generated charge carriers to be separated. As stated by Albert Einstein, light comes in packets of energy (quanta) called photons. Which helps to generate the charge carriers. As mentioned in the previous section how the energy bandgap ( $E_g$ ) affects the excitation of charge carriers. This minimum amount of energy needs to be absorbed from a photon to allow the excitation of electrons into the conduction band, which creates an electron-hole pair. At the same time, these electrons and holes need to be separated and extracted to have a charge flow when connected to an external load.

Further, this separation is also required to avoid the recombination of the generated electron-hole pairs. This is achieved through a p-n junction device where materials doped with impurities are brought together. These impurities introduce an excess concentration of electrons, donated as an n-type region. Whereas excess in holes a p-type region is shown in Figure 2.2. When these two materials are brought together, a concentration gradient for majority carriers in n and p type regions occurs. This results in the movement of holes from p-type to n-type and electrons from n-type to p-type region. Further, this process leads to a depletion of charge carriers around the metallurgical junction<sup>1</sup> resulting in the exposure of positive ions on the n-type side and negative ions on the p-type side. This depletion of charge carriers around the metallurgical junction is called a depletion region, where an electric field is established due to the exposed ions on either side of the region. This leads to charge carriers entering the region being forced to travel or drifting in the opposite direction of their gradient. Finally, this process of diffusion continues until it reaches an equilibrium with the established electric field. Hence, this is called as a drift-diffusion method for charge-carrier separation.[18]

However, when sunlight is illuminated this equilibrium is removed allowing the charge carriers to flow from both the junction. To explain this consider an illustration where the n-region in Figure 2.2 is the photoactive area resulting in charge carriers being generated. For an effective charge separation, it is necessary to separate the holes to the left (p-region) and electrons to the right contact side. During photo generation, the concentration of the holes in the n-type area increases because they are the minority carriers. As a result, the concentration of minority charge carriers is substantially higher than in the depletion region. It creates a gradient for minority carriers, moving them towards the depletion region. Further with the presence of an electric field, they drift across the depletion region, as the majority of the minority carriers in this region have shifted (drifted) across the neutral region it causing the gradient to stay. This similar diffusion process causes the holes to drift toward the p-region also result in electrons (minority carriers) in the p-region undergoing a similar separation before they are collected. [20]

<sup>1</sup>The region at the interface of p and n-type semiconductors

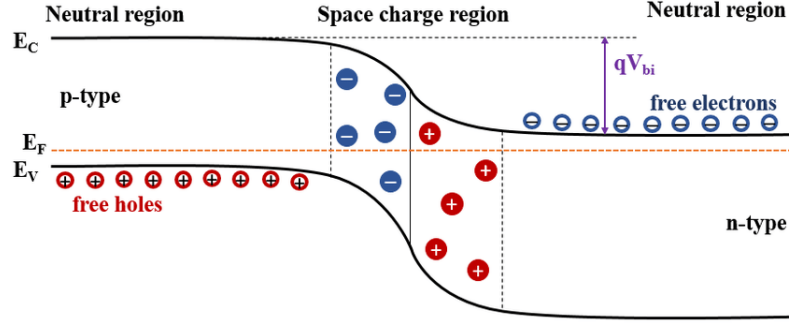


Figure 2.2: P-N junction formation with the contact of different semiconductor dopants. Adapted from [19]

## 2.2. Energy conversion limits

Though photovoltaic promises a potential path to convert sunlight into electricity. Their photo conversion efficiencies (PCE) appear low when compared to conventional gasoline/diesel engines. Therefore, it is necessary to understand the limits of achieving higher PCE, which will be presented in this section. As the solar cell cannot be an ideal or perfect device to convert energy, there exist some limits due to thermodynamic, spectral mismatch, and optical and electrical losses which are called as the fundamental losses. Based on certain physical assumptions, Shockley and Queisser (SQE) formulated the limiting efficiency in a solar cell. However, this limit assumes only radiative recombination and does not consider optical losses [18]. First, the fundamental losses depriving solar cell efficiency followed by optical and electrical losses will be discussed.

### 2.2.1. Fundamental losses

There are five fundamental losses considered to impact the efficiency of a PV device. These losses are intrinsic as they cannot be overcome by optimization of the device stack or materials. [6].

Photons typically have energies that differ from the bandgap of a semiconductor material. When the energy of photons striking the solar cell exceeds the bandgap of the material ( $E_{ph} > E_G$ ), electrons in the conduction band are excited to higher levels. This excess energy leads to the excitation of charge carriers higher into the conduction band level, which later on interaction with the phonons cools down to the band edge. This loss mechanism is called the "Thermalization loss". Similarly, an electron is not excited into the conduction band when the energy of the photons striking the solar cell is less than the bandgap of the material ( $E_{ph} < E_G$ ). This is referred to as "below bandgap" losses. [6]. Both the mentioned losses occur due to spectral mismatch between the energy of photons in the sunlight spectrum and the energy bandgap of semiconductor materials. The losses due to the mismatch are accounted through the ultimate conversion efficiency as determined in equation 2.1 for a single junction solar device. The terms  $P_{abs}$  and  $P_{use}$  indicate the fraction of energy absorbed by a solar cell and the energy it can deliver in a useful form, respectively.

$$\eta_{ult} = P_{use} * P_{abs} = \frac{E_G \int_0^{\lambda_G} \Phi(\lambda) * d\lambda}{\int_0^{\lambda_G} P(\lambda) * d\lambda} * \frac{\int_0^{\lambda_G} P(\lambda) * d\lambda}{\int_0^{\infty} P(\lambda) * d\lambda} \quad (2.1)$$

Based on Kirchhoff's law, a solar cell requires the preservation of equality between absorptivity and emissivity of radiation. This principle leads to a decrease in current as a result of radiative recombination, which ultimately reduces the conversion efficiency and is commonly referred to as "Emission loss". Fourthly, the solar cell works as a heat engine, where heat flows from a hot reservoir (Sun) to a cold reservoir (atmosphere). So, according to the second law of thermodynamics, the flow of heat from a hot to cold reservoir requires some work to be transferred from the system, this system loss is referred to as the "Carnot loss". Finally, the mismatch between the solid angle of the sun's thermal emission  $\Omega_{abs}$  and the solid angle of emission  $\Omega_{ems}$ , causes a reduction in free energy carriers. This loss mechanism is called as the "Boltzmann loss" which is a function of  $\ln(\frac{\Omega_{abs}}{\Omega_{ems}})$  as given in [21]. These five fundamental losses as depicted in the Figure (2.3) for a single junction device constitute the losses derived by the SQE

limit resulting in a theoretical efficiency of 33.1%<sup>2</sup>. [18]

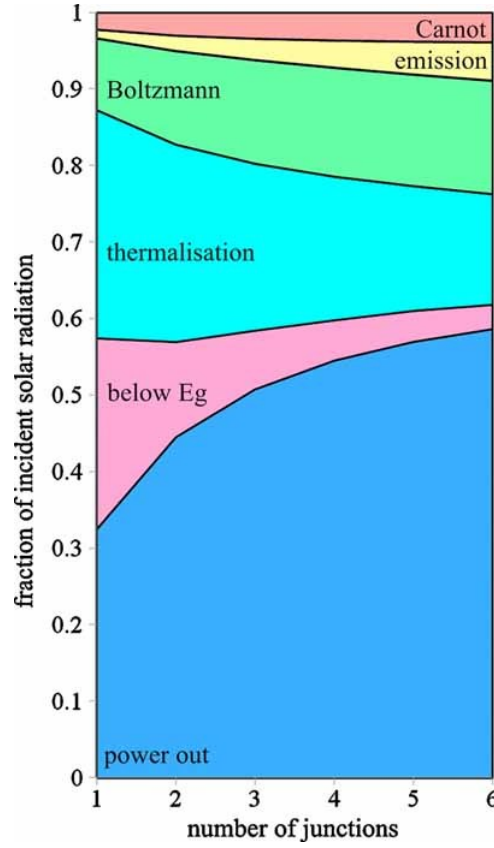


Figure 2.3: The fundamental losses for device with multiple junctions. Adapted from [6]

However, this theory only accounts for radiative losses to be occurring in a device that is not applicable to indirect bandgap semiconductor devices (eg: Si) and also other optical losses such as reflection, parasitic absorption, and non-contact losses are neglected. Hence, these extrinsic losses will be detailed in the following sections.

### 2.2.2. Optical losses

The optical losses can occur because of the following: reflection, and parasitic absorption. It also includes the losses due to shading by the metallic pattern present for the collection of charge carriers and connection to an external load.

The light traveling in a solar cell has to be absorbed in the bulk of the material to produce electron-hole pairs which are later separated through the drift-diffusion method as explained in Section 2.1.1. Before the photons from sunlight are absorbed, they undergo reflection, refraction, and transmission. These phenomena induce some losses, causing relatively fewer photons to be absorbed than those reaching the absorber layer. Firstly, reflection is the optical phenomenon of light reflecting away from the surface into the same medium it has entered from. Using Fresnel coefficients [20], it is possible to determine the amount of light reflected from a surface. For instance, an incident light that has reflected normally to surface allows us to determine the reflectivity as shown in Equation 2.2. Where  $n_{air}$  is the refractive index of air and  $n_{ARC}$  is the refractive index of the medium that light reaches.

$$R = \frac{|n_{air} - n_{ARC}|^2}{|n_{air} + n_{ARC}|^2} \quad (2.2)$$

Further, the light that is transmitted into the solar cell is not completely absorbed in the bulk. Since a solar cell is not limited to the absorber layer, but consists of other layers which support in an efficient

<sup>2</sup>This conversion limit is derived for AM1.5 spectrum for an energy bandgap of 1.34 eV

charge collection. Due to this, few incident photons are absorbed before they could reach the absorber layer. This phenomenon of light undergoing absorption in layers other than the absorber layer is called parasitic absorption. It refers to the optical absorption process which does not generate any electron/hole pair[22]. Account for the absorption of light along its path length in a c-Si semiconductor, the Lambert-Beer law as in equation 2.3 can be considered. The term ( $\alpha$ ) represents the absorption coefficient, which is a function of the wavelength of light and extinction coefficient ( $k$ ). This law plays a vital role in improving the light management of the device as it can help determine the light absorption at different depth.

$$I^{abs} = I_0 [1 - \exp(-\alpha d)] \quad (2.3)$$

Finally, the electrical connections made on the front side (light entering) have metallic strips printed on them for collection and transport of charge carriers to the circuit. But, these connections cover the surface of the solar cell reducing the area available for light coverage. This reduction in an active area of solar cells resulting in a reduction of light that can be absorbed. The loss of incident light is accounted for through Equation 2.4 which is the ratio of cell area not covered by the metallic strips ( $A_{cov}$ ) and the total area of the cell ( $A_{tot}$ ).[18]

$$C_{sh} = \frac{A_{sh}}{A_{tot}} \quad (2.4)$$

### 2.2.3. Recombination losses

It is evident from the fundamental and optical loss mechanism that it is not possible to completely absorb the entire solar energy spectra. Similarly, an electron which is excited into the conduction may undergo annihilation (recombination) with the holes in valence band. This process of charge - carrier recombination before they are collected at their respective contacts results in recombination losses. In a c-Si PV device these losses are branched into bulk and surface recombination. Indicating the location where a loss mechanism occurs.

Firstly, the presence of trap states at the surface of a c-Si semiconductor layer leads to surface recombination. This recombination occurs due to the presence of unbounded silicon atoms called dangling bonds, causing the generated charge carriers traveling towards the surface to recombine. These dangling bonds can be reduced by the deposition of suitable materials, which can form covalent bonds with the semiconductor surface.[18]

Secondly, in the lattice of a c-Si semiconductor charge -carrier recombination occurs due to the presence of trap/defect states as shown in Figure 2.4. This recombination process is called as the Shockley-Read-Hall (SRH) recombination. Depending on the location of these trap states, the mechanism of electron-hole pair recombination differs. The trap levels in this recombination are present within the forbidden band of a solar cell which occurs due crystal impurities or imperfections[18]. The mechanisms which occur in SRH are,

1. hole emission, where an electron jumps from the valence band to the trapped level
2. hole capture, an electron moves from the occupied trap to the valence band and recombines with the hole
3. electron emission. an electron jumps from the trapped level to the conduction band
4. electron capture, an electron moves from the conduction band to an unoccupied trap state

This mechanism can also dominate in direct bandgap materials, where they have low carrier densities or with high density of trap states.

The last recombination to be discussed is the Auger recombination process and is the most important at higher doping or charge carrier concentration [18]. In this process, the excess energy obtained due to the recombination of the electron-hole pair is transferred to electrons or holes which are excited into higher energy states as shown in Figure 2.4. Further elucidating, the momentum and energy of the recombining hole and electron is absorbed by an electron(hole) which leads to the excitation of an electron into higher energy levels of the conduction band and lower levels of the valence band for holes. Later they relax to their initial energy levels and transfer their energy as phonons (vibrational energy).[18].

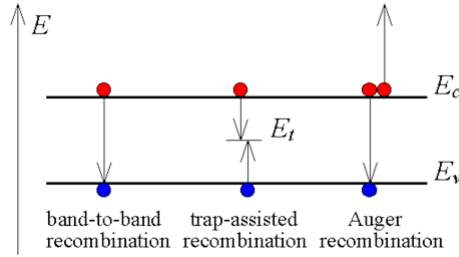


Figure 2.4: Schematic representation of the different bulk recombination process. Adapted from [23]

## 2.3. Multi junction devices

As discussed in the section earlier, a single-junction solar cell cannot achieve higher efficiencies (above Shockley-Queisser limits) due to the numerous loss mechanisms (Fundamental, Optical, and Recombination) stated. However, by introducing more *pn*-junctions to an existing device, efficiency can be increased. This occurs mostly as a result of improved solar spectrum utilization, which lowers spectral mismatch. Figure 2.3 illustrates how the thermalization and below  $E_G$  losses in a solar device decrease with increasing junctions. Though there is also an increase in Boltzman, emission, and Carnot losses. The overall result of improved spectrum utilization reduces these thermodynamic constraints. This improvement is reflected in the theoretical efficiency achieved for increasing the number of junctions as shown in the table 2.1

Theoretically, implementing these sub-cells seems simpler. However, it requires the selection of suitable semiconductor materials and junction configurations which can provide cost-effective and simple fabrication for utility-scale systems. Since Si is already a dominant PV technology with an energy bandgap of 1.12 eV. This narrow bandgap makes it a much more practical choice to implement this in a multijunction device for bottom cell application as mentioned in Section 1.1. While for a top cell, there are several materials with bandgap wider than c-Si and these include III-V, II-VI, and perovskites. The first two materials are difficult to deposit or grow on a c-Si due to the lattice mismatch, which results in reduced PCE. Moreover, their fabrication process is expensive and complex making them less viable for large-scale integration. However, an emerging technology in the PV field, perovskites brings in a cost-effective solution and wider energy bandgap. Making it more suitable for a top cell on a Si device.

Finally, fabricating many junctions into a device increases the process complexities, a two-junction or tandem device is the simplest way to manufacture these devices [4]. Therefore, this section will provide a brief introduction to c-Si and perovskite device technology along with their implementation as a tandem device.

Table 2.1: Theoretical efficiency predicted for different junction devices. [24]

Number of junctions	Theoretical efficiency
Single	29.43 %
Double	45 %
Triple	51 %
Four	55 %

### 2.3.1. Perovskite/Si tandem device

The fabrication of a tandem solar cell can be achieved in different ways, where each of them have their specific pros and cons. A monolithic tandem device (2T) is a simplest way of implementing this multi-junction approach and it involves the fabrication of a high bandgap cell on top of a low bandgap cell and with an interconnection layer in between for vertical transport of charge carriers. As shown in Figure 2.5 such devices are electrically connected in series where the output voltage is the sum of individual cell voltages. But the current measured will be the current produced by a limiting cell <sup>3</sup>[24]. This limitation requires the two sub cells to be designed for generating similar photocurrent. Also it

<sup>3</sup>A limiting cell, is the individual cell which is producing the least amount of current.

requires optimization of interface layers stack to facilitate efficient recombination of charger carriers from top and bottom cell.

In 4T devices, two independently manufactured solar cells are mechanically stacked on each other but consist of four electrodes as shown in Figure 2.5. This provides 4T cells to be operated at their maximum power point independently, eliminating the issue of current matching. But to independently extract power, they require discrete inverters, which increases the cost of these cells relative to 2T device[25]. Moreover, this device requires fabricating additional layer stack like TCO's, metal contact's relative to a 2T device. Further, increases the cost and complexity of their manufacturing.

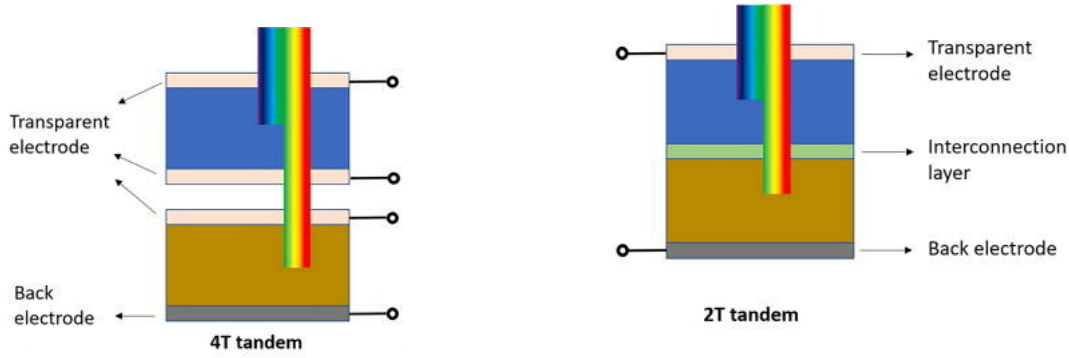


**Figure 2.5:** Schematic of a two junction tandem device 4T configuration (left) and 2T configuration (right). Adapted from [24]

Utilizing this 2T architecture, record-efficient solar devices of 31.25% and 32.5% were manufactured at Polytechnique Fédérale de Lausanne (EPFL) [26] and Helmholtz-Zentrum Berlin (HZB) [27] respectively. Though the device manufactured by HZB did not utilize a bottom-cell textured device and yet reached higher efficiency due to their reduction in recombination losses. While EPFL utilized a textured bottom cell, a hybrid process involving solution and evaporation techniques was used, it could be because of reduced quality in the perovskite that there is a lower PCE. Interestingly, a solution-based top-cell deposition onto textured bottom cell was achieved by King Abdullah University of Science and Technology (KAUST) with a record efficiency of 33.7% [28]. This highlights the necessity to incorporate light-trapping structures compatible with solution-based techniques.

## 2.4. Light propagation and behavior

The previously mentioned use of perovskite/Si tandem can utilize the light spectrum efficiently. But, to achieve better light propagation into solar we need light trapping strategies, which can be realized through a method called texturing. This section will discuss their importance.

### 2.4.1. Impact of surface morphology on light trapping

It is very important to begin with the rules of reflection and refraction in order to comprehend how light trapping is possible. According to the law of reflection, incident and reflected light rays always remain in the same plane when the angle of incident and reflected light is identical. When light enters a medium with a differing refractive index, it does so at an angle determined by Snell's law, as shown in Equation 2.5. A solar cell also undergoes this refraction as light travel from air to Si which have a different refractive index.

$$n_1 \sin \theta_1 = n_2 \sin \theta_2 \quad (2.5)$$

As light enters the solar cell, it must be absorbed in the active region to allow for better charge collection. Hence, a light ray must be trapped inside the cell for absorption to occur at a higher probability, and this strategy is known as light trapping. The path length of photons through the absorber is increased by using this technique, where the likelihood of electron hole pair absorption is higher.

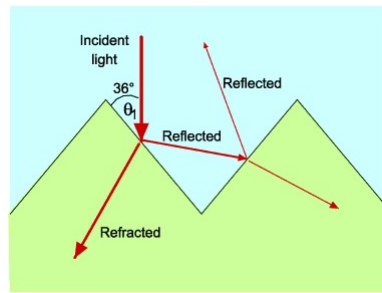


**Figure 2.6:** Effect of light rays being reflected at the interface of a solar cell

It was mentioned earlier that a flat surface is not ideal for reduced reflection losses. When light rays that are parallel to each other fall on a smooth or flat surface the reflected rays follow the law of reflection, this phenomenon is called the Specular reflection. In reality such surfaces do not exist and when parallel light rays interact with the interface they are reflected in random directions, such a reflection is called a diffused reflection. This interaction of light with a surface, exhibiting random roughness features, helps in tuning the path of incident light.

In a solar cell, such a surface with pyramidal features are created through the etching process, this develops a different etch direction [111] from the conventional [100] flat surface. As the light path is redirected through these features, they are reflected back onto the parallel surface improving the light coupling into the absorber material as shown in Figure 2.6. This property of creating an extended optical path for light coupling reduces the optical losses (reflection at the front surface) and is called as the double bounce effect.[29].

After these rays are refracted into the cell, its path length needs to be extended to allow for an increased probability of absorption. This is achieved through a concept known as total internal reflection. When light travels from a medium with a high refractive index to a medium with a lower index, the angle of incidence at the lower refractive index should be greater than the critical angle. When this phenomenon happens, light is reflected back into the same medium. This extends the path length of light travelling in the solar cell.

In mono c-Si where random pyramids are used for light trapping in the front surface are defined by their orientation planes. They have four [111] planes with the base being [100], the angle between these planes lead to an orientation angle  $54.7^\circ$  as shown in Figure 2.7. It was also proven through a ray optics simulation for random pyramidal textures, 44% of the light rays striking the surface is trapped [30]. Moreover, applying these textures on both sides of the wafers has a better potential for current generation, due to its light coupling properties. There is also an option of introducing these random pyramids which are either upright or inverted. It was shown through experimental and optical modelling that an inverted pyramid structure has better light trapping and electrical performance.[29]. This occurs because of an increasing light propagating distance, which a higher wavelength light has to undergo when compared to upright pyramids.



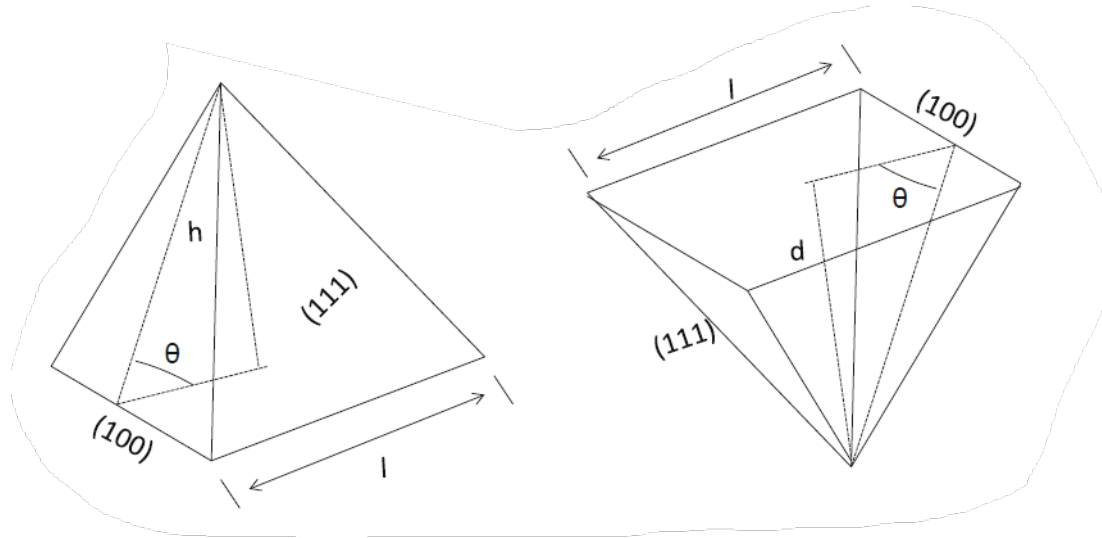


Figure 2.7: Schematic of upright pyramid (right) and an inverted pyramid (left) with their respective lattice orientations. Adapted from [31]

Finally, it is evident that surface texturing improves light trapping compared to planar structures, it should be noted that the [111] planar surface has a higher surface area covered which also increases the defects states. These defect states are the main reason for an increase in recombination losses. To solve these issues, a passivation layer deposition is necessary, which additionally has to provide an improved minority carrier lifetime. The optimization for this passivation layer is done with a hydrogenated intrinsic layer (*ia-Si:H*). Which will be discussed in Section 3.1.2.

### 2.4.2. Influence of interference and scattering

In the previously mentioned technique of the double-bounce effect, light rays interact with pyramidal features whose height or size is larger than the wavelength of light they are interacting with. Hence, using geometrical optics to indicate the reflection and transmission through Fresnel equations is possible. But, when the size of these particles reduces or becomes comparable to the wavelength of light then light-particle interactions take place, resulting in scattering and diffraction.[32].

$$x = \left( \frac{2 * \pi d}{\lambda} \right) * d \quad (2.6)$$

Furthermore, when a light wave interacts with an obstacle or nonhomogeneous feature these light waves are redirected to another path, this process is called as scattering. it is categorized into three parts depending on the Equation 2.6, where  $x$  is known as the size parameter and  $d$  is the size of particle.

1. If the size of the particle is much smaller than the wavelength of light then Rayleigh scattering takes place ( $x \ll 1$ ). The power radiated by this scattering, as shown in Equation (2.7), describes the effect of wavelength on scattering properties. Also, it is proportional to the 6th power of particle diameter. Considering these, smaller particle sizes at shorter wavelength regions have the highest Rayleigh scattering effect. Moreover, the scattering phenomena occur symmetrically as shown in Figure 2.8. [32].

$$\sigma_{\text{scattering}} = \frac{\frac{2}{3} \pi^5 d^6 \left( \frac{n^2 - 1}{n^2 + 2} \right)^2}{3 \lambda^4} \quad (2.7)$$

2. For particle size larger than or comparable to the wavelength of light a Mie scattering takes place ( $x \sim 1$ ). Similar to Rayleigh scattering this phenomenon is elastic in nature i.e. no change in wavelength or frequency is observed It is also elastic in nature. But, Mie scattering does not undergo a symmetrical distribution of light, rather it is larger in the forward direction as shown in Figure 2.8.
3. While, particles are in size much larger than the wavelength of light it interacts with, geometric scattering takes place. In general, for the ratio of particle diameter to wavelength of light greater

than 10, the interaction of light is defined through geometrical optics [31]. It also indicates the wave nature of light becomes less significant.

The theory of geometrical optics was used by Yablonovitch in 1986 to indicate the maximum limit to which the light trapping in a solar cell can be enhanced. In this theory, they demonstrated that by introducing a surface roughness onto Si wafer the absorption limit can be enhanced  $4n^2$  with certain assumptions as mentioned below. before escaping [33, 34].

1. The thickness of the substrate is larger than the wavelength of light.
2. A period for grating or random textures is much larger than the wavelength being used for light trapping.
3. Single pass absorption is negligible.

. Further, indicating that a light ray in a silicon with refractive index ( $n=3.5$ ) can make 50 passes in the wavelength range of 1000-1200 nm.

These principles are very much valid for large ( $> 2 \mu\text{m}$ ) pyramids and absorber thickness greater than  $100 \mu\text{m}$ . But, for surface features that have sub-micron-sized features, geometrical optics might not be valid. Therefore, a wave-optical phenomenon is necessary to describe such features [35]. It was showcased that smaller pyramids influence the angular intensity distribution (AID) due to scattering events at the peaks and edges of pyramids. Further from the AID experiment results conducted by Chen [36] for random pyramids with a mean height of  $0.43 \mu\text{m}$  as showcased in Figure 2.9a (Recipe C). This increase in the reflection of light to higher angles has resulted in increased reflection compared to smaller pyramids observed in Figure 2.9b. Similar results regarding weighted average reflectance were obtained for smaller pyramids experimented in this thesis, which will be illustrated in Chapter 4.

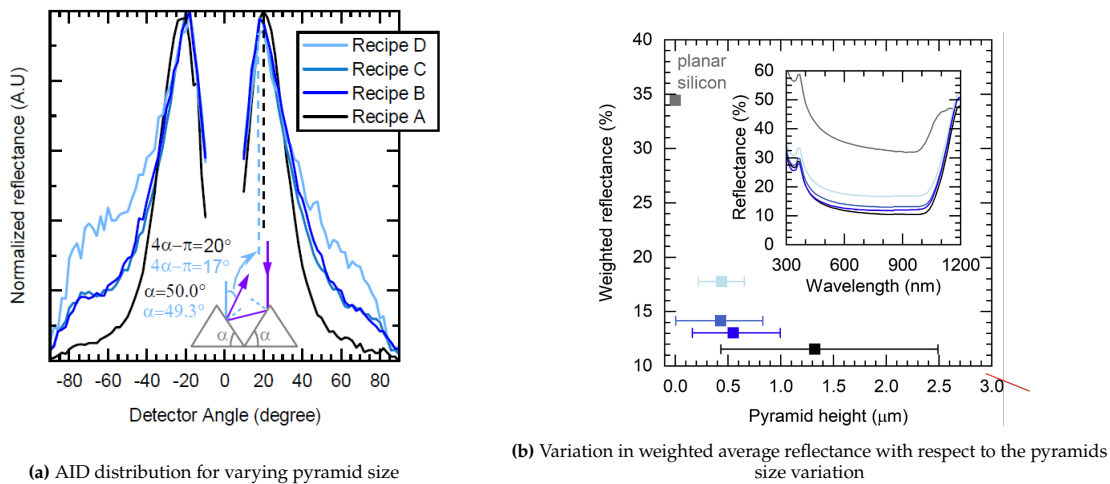


**Figure 2.9:** The effect of smaller pyramids on reflection illustrated through AID and weighted average reflectance measurements. Adapted from [36]

Therefore, to improve the optical performance of a device light trapping structures are crucial. It is possible to implement such a morphological variation on a device instead of a flat surface, to effectively trap light and reduce reflection by understanding the above-mentioned behavior of light propagation.

### 2.4.3. Prospects of periodical nano textures

As discussed earlier, perovskites are incompatible with micrometer pyramidal textures. This causes a loss in optical properties for the bottom cell as these structures allow for better light trapping in the absorber layer. [37]. Hence it is necessary to evaluate the optimal textured surface suitable for these applications. Apart from reducing the height of random pyramids, nano-scale periodic gratings is a concept that was widely investigated for thin-film solar cells, and it is interesting to study their effect for perovskite/Si tandems. As these structures have proven to provide angle selective scattering [38], which allows for manipulating the periodic structure to provide better enhancement of light path at

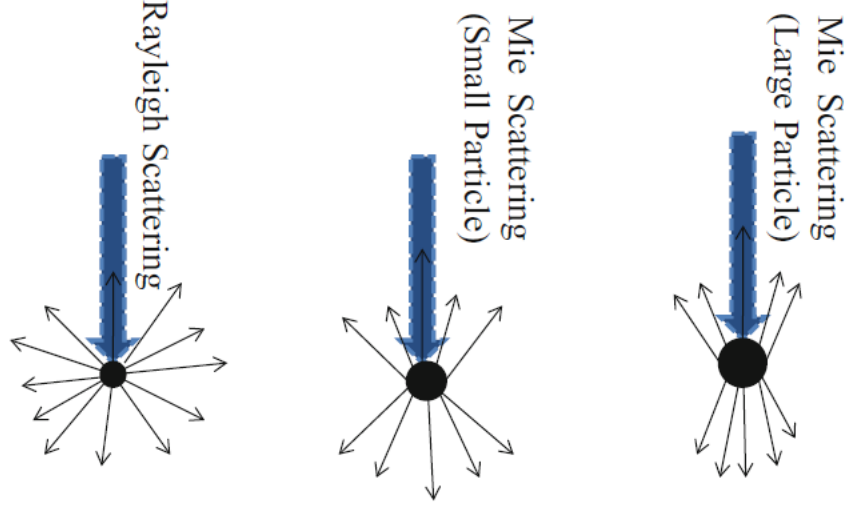


Figure 2.8: Distribution of scattered light for Rayleigh and Mie phenomena. Dapted from [32]

selective wavelength range. Since such control over random pyramidal features is not possible, it makes periodic gratings a potential area of interest.

To better evaluate the effect of light trapping in such thick solar cells light path enhancement (LPE) theory was formulated [39]. In this theory, the enhancement of the light path is determined by the LPE factor by considering negligible absorption losses and no interference effects due to the optically thick sample. Further by evaluating the mean path length of light ( $l_0$ ), before it escapes from the thick sample and probability of light out-coupling from the boundaries ( $P_{out}$ ) led to the derivation of LPE factor as shown in eq (2.8).

$$LPE = \frac{l_0}{P_{out}} \quad (2.8)$$

The calculation of the numerator involved averaging the polar diffraction angles over all diffraction orders, considering a double pass factor of 2 was multiplied. While the denominator was derived by calculating the intensity of light from escaping diffraction order and the intensity of light on the front side of the cell. Based on these a statistical model was devised for hexagonal and square lattices as shown in Equation 2.10 and 2.10 respectively to understand the effect of diffraction gratings.

$$LPE_{square} = \frac{4\pi n^2 \left(\frac{d}{\lambda}\right)^2}{M_{esc}} \quad (2.9)$$

$$LPE_{hexagonal} = \frac{4\pi n^2 \frac{2}{\sqrt{3}} \left(\frac{d}{\lambda}\right)^2}{M_{esc}} \quad (2.10)$$

The LPE theory previously stated considers statistical assumptions making it too simplified, hence it was modified by deriving the solar radiation and probability of out coupling through conical illumination [39]. Based on these derivations it was found that for square gratings (cross gratings) the best LPE was found for patterns that have  $d/\lambda \leq 1$ , where LPE factor crossed the  $4n^2$  limit. Compared to the Yablonovitch limit that was described earlier which assumes having a Lambertian front scatterer and 100% back reflector. The conventional random pyramids represent these Lambertian scatterers that scatter light evenly[34].

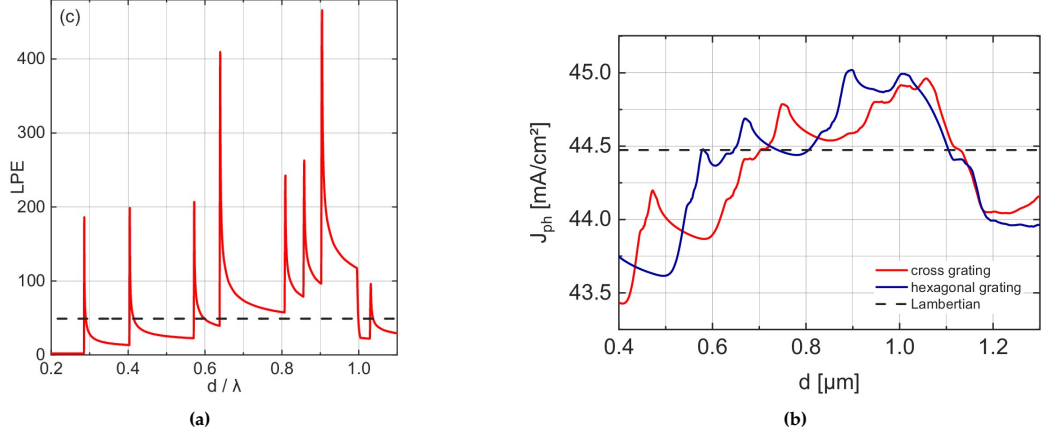


**Figure 2.10:** Variation in LPE (a) and  $J_{ph}$  enhancement (b) factors varying with grating size. Adapted from [39]

While with periodic grating the light enhancement factor can exceed the Yablonovitch limit for squared or hexagonal grating. This was also confirmed in the LPE theory based on the periodicity limits they estimated. This led to an indication that for a  $d/\lambda$  range of 0.64-0.7 and 0.8-1 a high LPE value was achieved as shown in Figure 2.10a. Moreover, by evaluating the effect of this pattern period with respect to the photo-current density, it was found that  $d$  in the range of  $0.75 \mu\text{m}$  to  $1 \mu\text{m}$  provided the highest results as shown in Figure 2.10b. Finally, by evaluating these results, it was considered to evaluate the fabrication of the bottom cell with inverted pyramids having a period in the range of  $0.8 \mu\text{m}$  to  $1 \mu\text{m}$ .

Secondly, the depth of periodic patterns is an important concept as it dictates the efficiency distribution into diffraction orders. In order to determine the depth of these features two constraints need to be remembered,

1. Height should be smaller than a micrometer or less than the thickness of the perovskite absorber.
2. The aspect ratio should be suitable for trapping light effectively.

So, based on optical modelling performed for sinusoidal 2D nano-textures [40]. It was indicated that for a layer stack with cosine wave structures. A higher short-current density can be achieved with increasing aspect ratio from 0.25 to 0.5 as shown in Figure 2.11. So, considering that a similar aspect ratio will provide better light trapping while maintaining the period range between  $0.8 \mu\text{m}$  to  $1 \mu\text{m}$ . It was decided to proceed with fabricating the pyramidal structures with these assumptions, which will be presented in a later Chapter 5.

The influence of short-circuit current density on wavelength may serve as an additional justification for keeping such a periodic range. The current density in perovskite top-cell decreases after a wavelength of  $750 \text{ nm}$ , as illustrated in Figure 1.2b. Since the bandgap of this perovskite, is approximately  $1.64 \text{ eV}$ , it results in the photons below this bandgap passing through the bottom cell to be absorbed more effectively. Additionally, employing structures that would increase the amount of light entering the bottom cell without reflection, could potentially improve the overall device performance. It would therefore be advantageous to implement light-trapping structures that can offer improved absorption in the range between  $750 \text{ nm}$  and beyond.

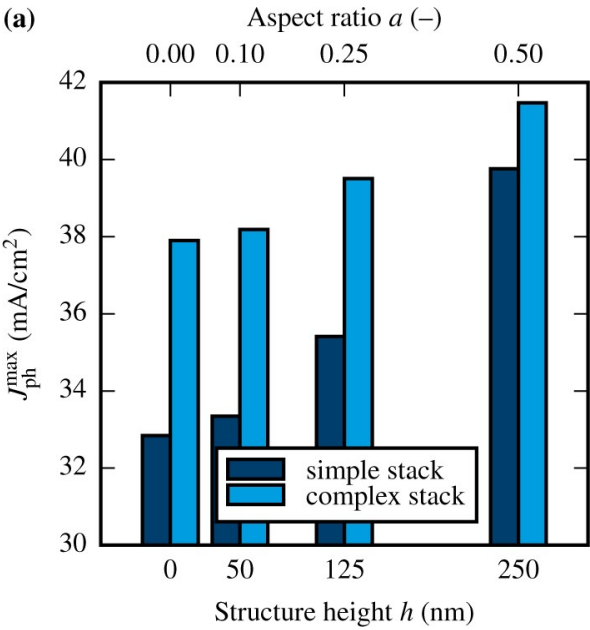


**Figure 2.11:** Variation in current density with improving aspect ratio. Adapted from [40]

## Processing and characterization of surface textures

In this chapter, the experiment tools used for characterizing, depositing, and patterning on the Si substrate years will be presented. Firstly, the plasma-based techniques used for deposition and etching along with their respective equipment used will be presented. Secondly, a description of the patterning done through E-beam and nano-imprinting alongside the wet-chemical processing techniques will be presented. Finally, the characterization setups used to analyze the topography, optical characteristics, and passivation will be presented.

### 3.1. Plasma-based techniques for etching and deposition

In the micro-electronic industry plasma-based process are widely used in device fabrication involving deposition and etching of layers. These techniques namely reactive ion etching and plasma-enhanced chemical vapor deposition are used in the thesis for deposition and patterning on Si substrate.

#### 3.1.1. Plasma based etching

Discussing the etching process, the pattern that has been exposed by a lithography step is transferred to the underneath layers by an etching technique called as reactive-ion etching (RIE). This process involves ions generated from a plasma that results in bombardment of the surface to create the desired pattern.

The generation of plasma takes place by applying a voltage between electrodes through, Capacitively Coupled Plasma (CCP) or Inductively Coupled Plasma (ICP) through a Radio-Frequency (RF) source. This RF source causes an oscillating electric field, which causes electrons to oscillate between the electrodes. This results in the collision of highly mobile electrons with slowly moving ions causing the ionization to occur and generating plasma. Further, the plasma also contains free electrons, ions, radicals and neutral species. The positive ions present are accelerated towards the substrate, due to the voltage difference present between plasma and negatively charged plate (Bias voltage). Causing ions to bombard the surface.[41]. The gases usually preferred for this process are inert under normal conditions but turn into highly reactive species under plasma. The most commonly used gases include, CF<sub>4</sub>, SF<sub>6</sub>, CHF<sub>3</sub>, Cl<sub>2</sub> and etc which undergo a reaction process as shown in 3.1 to etch relevant materials ,

1. Reactive species and neutral radicals/ions are generated due to the plasma created
2. The generated neutral ions/radicals are transported and adsorb on the surface of the substrate.
3. Reaction takes place at the surface of the substrate and then by-products are created.
4. The generated etch byproducts desorb from the surface of the substrate.

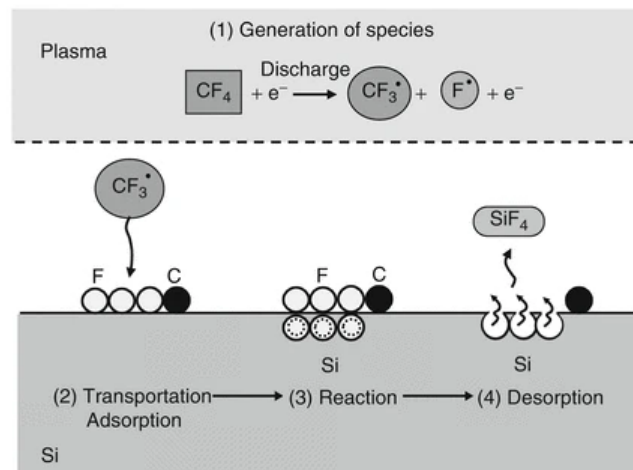


**Figure 3.1:** Process of etching a substrate using  $\text{CF}_4$  molecules. Adapted from [41]

The plasma and bias voltage in a CCP RIE reactor are controlled by a single plasma source generator. The power from the RF source is received by the electrode that is holding the substrate. On the other hand, an ICP-RIE reactor has two plasma source generators. In this configuration, the plasma is produced by the ICP, where an extra source powers the grounded upper electrode. In the meantime, the bias voltage is supplied by connecting the bottom electrode, which is holding the substrate, to the CCP source, as shown in Figure 3.2.[42]

The ICP-RIE is a preferred source that allows for high-density plasma to be generated. This increase in plasma density allows for better-etched surface quality, anisotropy (vertical sidewalls) and high etch rate [42]. These processes involve several chemical species suitable for etching different desired materials. Consequently, the reaction of these chemicals with the substrate varies with certain process conditions such as temperature, pressure, and power. These parameters are very crucial to be optimized for obtaining the relevant etch profile.

The ICP-RIE Oxford Estrelas 100 at Kavli Institute of Nanoscience, Delft is used to carry out the cryogenic etching procedure, also known as the cryo-process. This method makes use of the substrate holder's extremely low temperature to reduce the mask's etch rate and, most significantly, to produce a superior etch profile (Anisotropic) [43]. Through the use of a liquid nitrogen or water-cooled stage, the electrode's temperature can be adjusted to as low as  $-130^\circ\text{C}$ . In our application, the resist walls must be able to endure ion bombardment while maintaining strong vertical sidewall characteristics while having a very thin thickness of up to 110 nm.

Since the etching rate decreases at such low temperatures, the flow rate of gas species can be raised to boost the etching rate. Additionally, this procedure permits a significantly higher etch selectivity by

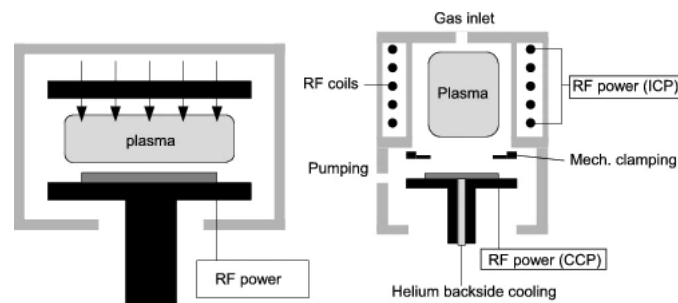


**Figure 3.2:** Schematic of CCP based RIE chamber (left) and ICP based RIE chamber (Right) [42]

reducing the amount of ion bombardment on the mask material [42]. However, it should be highlighted that carrier wafers, which are typically utilized for mounting smaller samples, cannot be used with the cryo process since the thermal pathway alters the etching parameters on the substrate, making it challenging to produce repeatable results.

Nevertheless, this method provides the selectivity and etching parameters needed to produce high-quality etching structures. In order to etch  $\text{SiO}_2$  and Si substrates that will be used in upcoming investigations.

### 3.1.2. Plasma based deposition

In a deposition process, the same dissociation process previously described through an RF source applied to an electrode creates a plasma. While for Plasma Enhanced Chemical Vapor deposition (PECVD) is a common technique used in the deposition of supporting layer-on solar cells (SHJ). For this process the equipment available at EKL, has a substrate placed on the grounded electrode, as shown in Figure 3.3. Further, the generated ions do not etch the surface, rather they are deposited due to varying process conditions and on the DC bias (which is lower in a PECVD tool compared to etching). Most importantly this process differs in the process gas flow used in comparison to plasma-etching process previously mentioned. For instance, in the deposition of *(i)*a-Si:H an important precursor gas required is silane ( $\text{SiH}_4$ ). The plasma generated through the  $\text{SiH}_4$  causes the generation of  $\text{H}$ ,  $\text{Si}$ ,  $\text{SiH}$ ,  $\text{SiH}_2$ ,  $\text{SiH}_3$  and other neutral radicals[44]. The next process involves transporting these radicals to the film surface through a voltage bias where they react with the hydrogen-terminated surface to form the *(i)*a-Si:H film. Further, the deposition process illustrated in Figure 3.4, involves the following steps [45].

1. Generation of reactive species
2. Transport of reactive species to the surface
  - (a) Desorption
  - (b) Recombination
  - (c) Abstraction
3. Transport of volatile products away from the surface

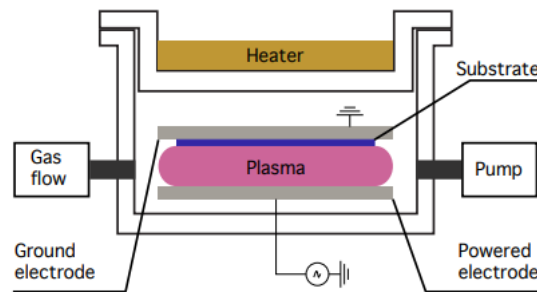


Figure 3.3: Schematic of the PECVD tool used for *(i)*a-Si:H layer at EKL. Adapted from [46]

The deposition of *(i)*a-Si:H as described previously is very crucial for developing a SHJ device. This deposition process as described previously is done in a Plasma-enhanced chemical vapor deposition (PECVD) technique. This further allows for the deposition of these layers at a lower temperature ( $< 200^\circ\text{C}$ ), eliminating the requirement of high thermal energy for dissociation. This makes PECVD process a suitable technique for the depositing *(i)*a-Si:H passivation layers[47].



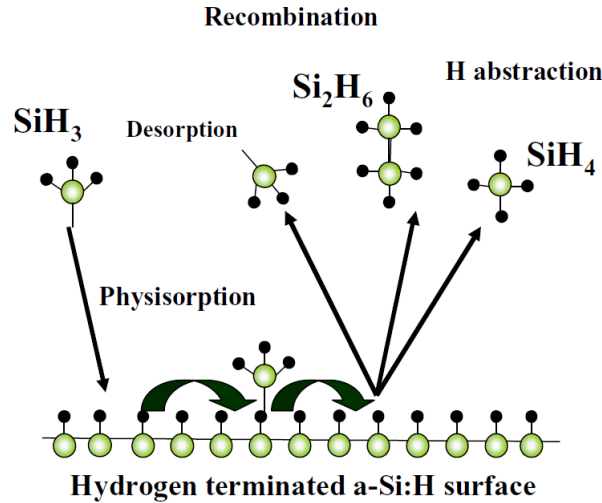


Figure 3.4: Schematic representation of the  $\text{SiH}_3$  reaction upon diffusion to the surface [45]

Passivation is a key property for enhancing the performance of solar cells. As the major issues discussed in 2.2.3 recombination losses induce a reduction in the overall performance. Hence to overcome such losses passivation schemes are introduced over a solar cell through passivation mechanisms usually applied to reduce such losses.[48]

The passivation layer strategy used in this thesis was related to an already optimized 10nm bi-layer approach by Giulia [49]. This method consisted of two layers: the first layer (i1) of *i*a-Si:H was deposited with silane, followed by the second layer (i2) with a particular dilution ratio of hydrogen to silane as shown in Table 3.1. Incorporating this two-layer method provides enhanced dangling bond passivation on the c-Si surface, by ensuring sufficient hydrogen diffusion to a-Si:H and c-Si interface [47].

Table 3.1: Deposition parameters of i1 and i2 layers considered for a bilayer passivation

Layer	T(°C)	Pressure (mbar)	Power density (mW/cm <sup>2</sup> )	Dilution ratio	Flow rate -Silane (sccm)	Frequency
i1a-Si:H	160	0.7	23.6	0	40	13.56
i2a-Si:H	160	1.4	23.6	3	10	13.56

### 3.2. Electron beam lithography

Lithography is crucial in enabling the development of integrated circuits (IC) in the semi-conductor industry enabling the creation of nanoelectronic, nanophotonic and biological devices. These lithography techniques are mainly divided into two categories namely optical and non-optical lithography [50]. In an optical lithography technique a photo-sensitive resist is coated on the substrate, later with the help of a mask, light is illuminated on the resist. So, the exposed photoresist undergoes a development procedure to remove the illuminated areas. The change in solubility of resist when exposed to light allows it to be removed during the development stage with certain chemicals. On the other hand, non-optical lithography as its name suggests does not involve any light exposure to create desired features. But involves electrons, ion-beams, and mechanical forces to create a pattern on the resist deposited. To create surface textures in the nano-meter scale both optical and non-optical techniques can be devised. These techniques can facilitate the creation of nano-scale features with much better control over the size.

A similar experiment using the optical lithography technique at Photovoltaics Materials and Devices (PVMd) group, TU Delft was performed by Thierry [51] to create honeycomb features on c-Si substrate. These features have a periodicity of 2-3  $\mu\text{m}$  and have been showcased to provide lesser reflection losses with a lower feature depth. But, the process flow required to create Inverted Nano Pyramids (INP), which have proven to provide good light trapping for c-Si substrates was not demonstrated in the group. This makes creating a process flow for the fabrication of INPs a good step for the comparison of different light-trapping features. However, the equipment used in the process of creating honeycomb structures

is an Advanced Semiconductor Manufacturing Lithography (ASML) stepper. This machine has an accuracy limit of 500 nm, making it difficult to create sub-micron periodical features. Therefore, the most feasible way to achieve these features was found to be by using Electron beam lithography (EBL).

E-beam lithography/ Electron beam Lithography is a process of creating a pattern on suitable resist through a focused electron beam. The created pattern on the resist is used as a mask to further transfer the pattern onto the substrate using the wet-chemical or previously mentioned RIE process. To create such patterns on the resist a compatible design should be provided to the system, which can be designed using a commercial CAD software L-edit [52]. Then the respective data is converted into the e-beam writer to create respective patterns[53]. For this process the E-beam lithography equipment Raith EBPG - 5000 plus available at the Kavli institute of nanoscience, TU delft, shown in Figure 3.5 was utilized.

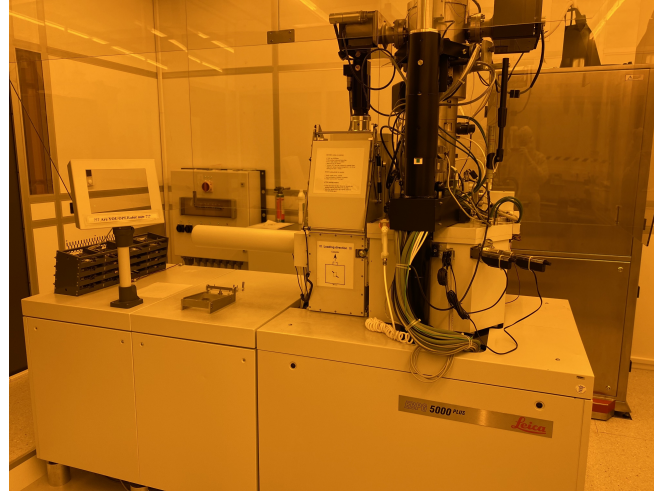


Figure 3.5: Raith EBPG 5000+

Important parameters that affect the pattern to be exposed are dependent on Beam dosage, spot size, beam current, beam step size, and beam step frequency. The exposure begins by finding the relevant Beam Step Size (BSS) required, determined by the dimension of the smallest feature to be exposed. Using the calculated BSS, the current and aperture required can be applied through pre-determined estimators at Kavli institute of nanoscience, Delft [54]. Finally with the desired dose the writing frequency of exposure is calculated as shown in Equation (3.1).

$$D\left(\frac{\mu C}{cm^2}\right) = \frac{I_{beam} * 100}{f_{exp} * BSS^2} \quad (3.1)$$

Since the resist exposed to electron beams has to further undergo a process of forward and back-scattering. These are two effects that occur due to electron-electron interaction and penetration into the resist material that undergoes scattering respectively. Due to this variation the complexity in electrons exposing the resist increases. The pattern required might undergo certain distortions with underdeveloped edges, due to the variation in e-beam dosage. To avoid such distortions the forward and backscattering electrons are approximated by a Gaussian model and provide a relative dosage in the pattern. This in general is referred to as the proximity effect correction (PEC) that provides the relative dose corrections in the patterns by avoiding any distortion. [54].

### 3.3. Thermal Nano Imprint Lithography

As the previously stated EBL, has a very high lead time for exposure and takes a lot of time in exposing multiple substrates. A technique called as nano-imprint lithography is considered to reduce the processing time. Imprint lithography is a pattern replication process where the topography from a master structure is defined onto a substrate. This technique allows for the replication of nano-scale features onto the substrate at a lesser process time. Thermal Nanoimprint Lithography (T-NIL) is one of the imprinting methods used to replicate nano patterns. In this process a thermally curable resist is coated onto the substrate, which upon heating above a glass transition temperature ( $T_g$ ) of resist making

the resist viscous. Then the templates on a mold are pressed against the substrate with a certain force, transferring the features onto the resist.[55].

Usually, PMMA is most widely used resist in T-NIL process because of its low shrinkage and therm co-efficient. This material has a glass transition temperature  $T_g = 110^\circ\text{C}$ . So usually a temperature between  $140^\circ\text{C}$  to  $180^\circ\text{C}$  is applied in the T-NIL process [55]. In this thesis, a daughter mold made from PDMS is used to replicate structures onto the PMMA substrate through EVG 501 bonder (EVG Group) as follows :

1. The process begins from an ambient temperature condition by placing the soft mold onto the bottom plat and Substrate over it.
2. The chamber then undergoes a vacuum process and raises its temperature to  $180^\circ\text{C}$ , which is maintained for 165 s.
3. After it reaches this temperature, a force of 1250N is applied by the top-plate as shown in Figure 3.6. This causes the features on the PDMS mold to be replicated onto the substrate. [56]
4. This force of 1250 N is maintained until temperature reaches  $80^\circ\text{C}$ . As this de-molding temperature allows for the substrate to withstand any thermal stress induced. Which might result in deformed nano features, if it is varied.
5. Finally, when the temperature reaches  $40^\circ\text{C}$ , the substrate is taken out.

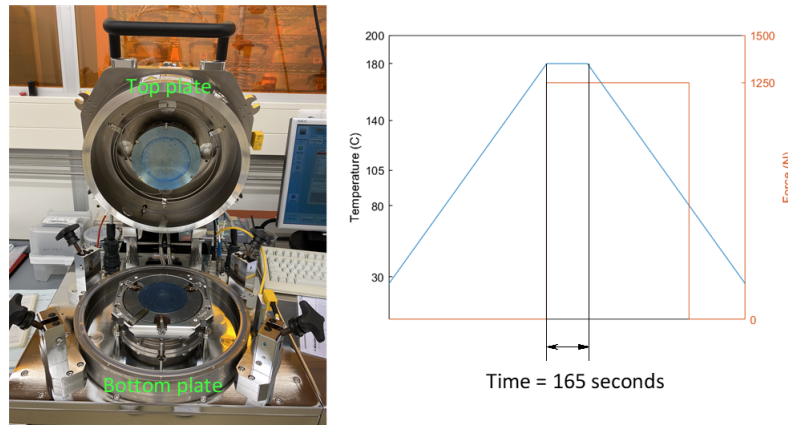


**Figure 3.6:** Indication of equipment (Left) and process curve for Thermal imprinting (Right).

Though a temperature between  $140 - 180^\circ\text{C}$  can be applied for the imprinting process to occur, it was demonstrated that a temperature of  $180^\circ\text{C}$  provides a better aspect ratio for the replicated pattern on substrate [56]. Hence, a similar temperature was used for processing.

### 3.4. Chemical based etching technique

Texturing is a crucial step in the solar cell manufacturing process, with its ability to improve light trapping and absorption in a tandem configuration as discussed in Chapter2. This texturing is usually done on a [100] crystal-oriented Si surface due to the lesser binding energy compared to a [111] orientation [14]. To create these pyramidal textures anisotropic method is usually used. It involves chemicals such as TMAH (Tetra methyl ammonium hydride), sodium hydroxide (NaOH) and potassium hydroxide (KOH), these chemicals are alkaline based and assist in etching the substrate and are called as alkaline-based etching.

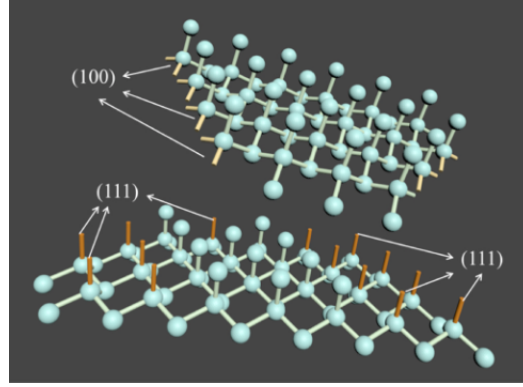
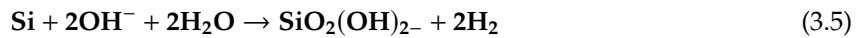
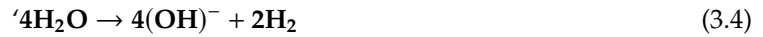


**Figure 3.7:** Schematic of Si bonding at different crystal orientations [100] (top) and [111] (bottom). Adapted from [57]

As shown in Figure 3.7, there is only one dangling bond (unbonded/loose) present for a [111] plane. While the [100] plane has 2 dangling bonds, which indicates Si has 3 covalent bonds attached and 2 covalent bonds for the [111] and [100] respectively. So, during etching the removal of surface breaking these bonds, and due to the relatively higher number of covalent bonds present for [111] surface it relatively requires more time to etch this surface. This makes [100] surface more suitable for creating texturing on the Si surface[57].



In alkaline based texturing process, where sodium hydroxide (NaOH), potassium hydroxide (KOH) could be used with (De-Ionized) DI water and other reactive agents like IPA. These KOH or NaOH ions contain hydroxyl group ( $\text{OH}^-$ ) ions which promote reaction with Si and forms  $\text{Si}(\text{OH})_4$  [58]. The main ion which initiates the oxidation process is the hydroxyl group ( $\text{OH}^-$ ) and their concentration is crucial in varying the solution etching kinetics. This process of KOH etching with Si is mainly initiated due to the presence of  $\text{OH}^-$  ions. Which are dissociated with the reaction of  $\text{H}_2\text{O}$  into  $\text{OH}^-$  ions. These ions react with Si forming  $\text{Si}(\text{OH})_2$ . Which are further reduced into  $\text{Si}(\text{OH})_4$ , as shown in Equation 3.2. Due to the high pH environment present, the orthosilicic acid ( $\text{Si}(\text{OH})_4$ ) is unstable and forms  $\text{Si}(\text{OH})_2^-$  as shown in Equation 3.3. The excess electrons present react with the water molecules forming  $\text{OH}^-$ . These  $\text{OH}^-$  ions generated at the Si surface are most crucial for the Si oxidation process to continue, instead of the bulk  $\text{OH}^-$  ions present in the solution [59]. This is also the reason a Si wafer (dummy wafer) was used only for activating the solution. Accompanied by the  $\text{OH}^-$  ions are the  $\text{H}_2$  bubbles, due to the reduction of water molecules as shown in Equation 3.4. It is these  $\text{H}_2$  bubbles that cause the lateral etching of Si acting as a mask [60]. The diameter of these bubbles vary in the solution and determines the size of the pyramids formed. It is also possible that the  $\text{H}_2$  bubbles might not be the main reason behind the size variation it could also be possible due to other molecules like  $\text{Si}(\text{OH})_4$  [61]. Overall, the KOH etching mechanism has many intermediary steps which are not entirely elaborated and for a much more detailed explanation, the article from Seidel [59] can be referred. Nevertheless, the stages in silicon etching can be described as follows [58]:

1. Diffusion of particles towards the silicon surface
2. Adsorption of reactive or non-reactive ions on silicon surface
3. Oxidation of silicon
4. Desorption of reaction products
5. Diffusion of reaction products into the solution

In addition to KOH, reactive agents like IPA are also used in the texturing process to allow for better wettability of Si surface as Si is hydrophobic in nature [31]. Discussing the important variables that can alter an etching process. The first one is the texturing time, which plays an important role in determining the quality of features created. As the time required for etching increases, the number, and size of texturing features increase. But having lesser or longer etching time could result in the creation of uneven and overlapping pyramids (Over-etching) respectively. Hence for an optimum textured surface, the solution concentration, temperature, and time need to be optimized [62].

Apart from depending on the AFM characterization—which will be covered later—in order to characterize the peak height. It was determined to use a wafer mass-based measurement to determine the amount of Si being etched. For this measurement, the wafers to be etched are weighed on a measuring scale with an accuracy of 1 mg both before ( $m_{before}$ ) and after ( $m_{after}$ ) etching. Mass loss ( $m_{loss}$ ) is the result of their difference. Based on the determined density ( $\rho_{Si}$ ) and wafer area ( $A_{wafer}$ ), which remained constant, the thickness loss ( $T_l$ ) was calculated using Equation 3.6. Finally, the mass loss ( $m_{loss}$ ) divided by the immersion time in the solution provides the etch rate.

$$\Delta T_l = \frac{m_{loss}}{\rho_{Si} * A_{wafer}} \quad (3.6)$$

### 3.4.1. Cleaning techniques

The creation of light-trapping features on c-Si solar cells can provide improved device performance through the alkaline texturing process described in the previous section. However, they also introduce enhanced surface recombination due to increased surface area and nano-scale surface roughness due to the wet-chemical processing techniques. [63]. For, SHJ solar cells, the interface between c-Si and (i)a-Si:H is crucial to form a good electronic interface, the presence of such roughness scale can impact the quality of amorphous layer deposited [64]. To remove these issues surface treatment procedures utilizing different chemicals were introduced [64],[65],[66].

This surface treatment process is separated into two stages: wet-chemical oxidation and oxidation removal. Wet-chemical oxidation is implemented first to remove contaminants from the wafer and reduce surface roughness. During this process, the compounds that act as oxidizing agents create an oxide layer at the Si contact. Some of the most common chemical utilised in this procedure, as well as their particular removal operations and chemicals utilised, are included in the table 3.2. Following the development of oxide, which is undesirable for surface passivation it is removed by using HF or  $NH_4F$  solutions. Since  $NH_4F$  solution induces defects that require further process steps, HF is most desirable for removing the oxide layer[67].

Cleaning process	Chemicals present	Contamination removed	Side effects	Reference
Piranha	$H_2SO_4 + H_2O_2$	Organic residues	Sulfate deposition	[67]
RCA-1	$NH_4OH + H_2O_2 + H_2O$	Organic residues	Metal ions redeposition & increased micro-surface roughness	[67],[65],[68]
RCA-2	$HCl + H_2O_2 + H_2O$	Metal ions	Micro-surface roughness	[67],[68]

**Table 3.2:** Chemical cleaning techniques indicating the contamination removed

Piranha cleaning involves a 1:3 solution of concentrated sulfuric acid ( $H_2SO_4$ ) and 30%  $H_2O_2$  at 120°C for 20 minutes. Although it is beneficial in removing organic residues such as photoresist, it causes sulfate contamination and increased roughness due to  $H_2O_2$  dissolution. The following cleaning steps, RCA-1 and RCA-2, remove organic and metal contaminants, respectively. Where RCA-1 cleaning employs a 1:1:5 ratio of  $NH_4OH:H_2O_2:H_2O$  at 75°C for 10 minutes, while RCA-2 uses a 1:1:5 ratio of  $HCl:H_2O_2:H_2O$  at 75°C for 10 minutes [64]. Because of the presence of  $H_2O_2$ , these procedures also result in the formation of a native oxide layer and also the oxygen bubbles that adhere to the surface induce roughness [68],[65]. Despite the oxide removal process involving HF dip being used it still indicated defect densities.

This finding was supported by a passivation test on an n-type <FZ>sample carried out by Dimitrios [66], where RCA cleaning demonstrated a higher lifetime than piranha cleaning. Apart from the  $H_2O_2$  dissociation the presence of the sulfate ions contaminating the surface could be a reason for this decline with piranha. Furthermore, the use of piranha solution necessitates a heating bath, making it less suitable on a hot plate and ultimately leading to its infeasibility for usage in experiments for this thesis.

The Nitric Acid Oxidation Cycle (NAOC) is an alternative to the cleaning solutions discussed above. It involves cleaning in 99%  $\text{HNO}_3$  at room temperature for 10 minutes, followed by 69.5%  $\text{HNO}_3$  at  $110^\circ\text{C}$  for 10 minutes. According to the previously mentioned experiment performed by Dimitrios [66], NAOC cleaning resulted in enhanced wafer lifetime when compared to RCA cleaning. In this procedure,  $\text{HNO}_3$  (99%) is used to remove organic residues, whereas  $\text{HNO}_3$  (69.5%) is utilised to remove metals. Similar to previous cases this wet-chemical oxidation of NAOC results in the formation of a thin oxide layer on the surface, which is later removed by the oxide removal process. The negligible surface roughness of NAOC reported, distinguishes it from other wet-chemical oxidation processes.

However, due to the contamination policy at Else Kooi Laboratory (EKL), using metal-contaminated wafers in the solutions involved for NAOC processing is prohibited. It was not feasible to investigate their effects in this thesis. As a result, a combination of  $\text{HNO}_3$  (99%) and RCA-2 cleaning was used to effectively clean and remove roughness caused by the texturing process through the oxide removal process. Moreover, using  $\text{HNO}_3$  (99%) does not require heating and prevents the reintroduction of impurities such as sulphur, making it more effective. Therefore, the selected cleaning technique involved dipping the wafers in concentrated fuming nitric acid (99%) for 10 minutes. Subsequently, the samples were rinsed in DI water for at least 5 minutes to avoid any  $\text{HNO}_3$  residuals in the following steps. Next, RCA-2 was used to remove any metal contamination. It consisted of heating a solution of hydrochloric acid (HCl), hydrogen peroxide ( $\text{H}_2\text{O}_2$ ), and water in a 1:1:5 ratio at  $75^\circ\text{C}$ . Afterward, the samples were rinsed in water again for 5 minutes.

### 3.5. Scanning electron microscopy

To analyse the surface morphology of the fabricated samples, scanning electron microscopy (SEM) is a useful way to image the surface with a spatial resolution in the nanometre scale. A SEM equipment comprises of electron generator, lenses and detectors to analyse the surface morphology of specimen. As shown in Figure (3.8), the topmost component in the schematic exhibiting a high voltage cable is connected to a assembly of components consisting of cathode and electrodes called as electron gun. The purpose of electron gun is to generate electrons at different accelerating voltages. Due to the presence of a potential difference between the cathode and anode, these electrons are accelerated downwards.

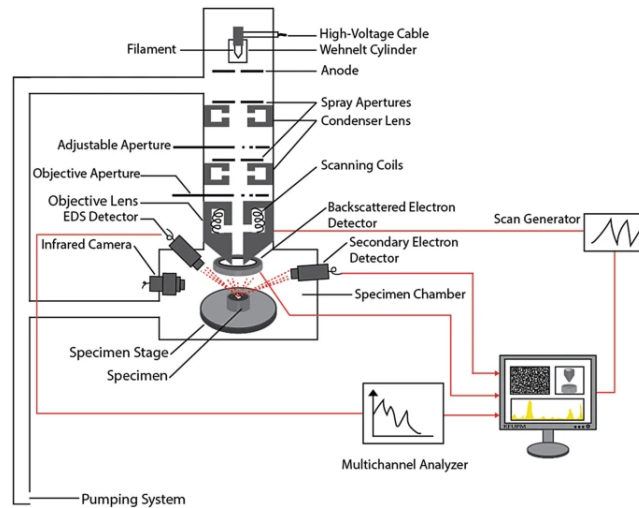


Figure 3.8: Schematic of a general SEM column with different components. Adapted from [69]

Finally, the accelerated electron through the lenses strikes the substrate which leaves the sample after being deflected. To be able to capture the signal/ electrons leaving the specimen after penetrating them, detectors are required. The signal emitted from the specimen consists of secondary scattered and back-scattered electrons, which generate their respective images.[69]. Here the secondary electrons occur due to the inelastic collisions between the electron beam and specimen, causing a displacement of electrons in the atoms. This results in secondary electrons. While, there are also electrons that penetrate through the sample and undergo elastic collisions with it, resulting in back-scattered electrons. This similar effect also occurs in the e-beam lithography step that causes forward and back-scattered



electrons.

Hitachi SE 8230 in EKL was employed for morphological analysis in the experiments. However, the most critical factors to consider for attaining high-resolution imaging of the substrate are the appropriate working distance and desirable beam voltage. A lower beam voltage can be used while maintaining the shortest working distance for top-view sample inspection. However, a considerably greater beam voltage may be necessary for cross-sectional images since it will enable us to catch more features that are deep into the substrate. Therefore, while using a trial-and-error approach to experiment and create a decent record, these elements must be taken into account.

### 3.6. Atomic force microscopy

Atomic force microscopy (AFM) is a high-resolution microscopy technique that allows finding the surface topography of the sample. Unlike SEM where the analysis of surface height is difficult, AFM provides a 3D resolution of the sample. This technique is suitable to perform on Si and polymers which are most likely to be used in this thesis.

Its mode of operation involves a cantilever beam with a tip that measures the depth profile of surface textures in a raster motion<sup>1</sup>. As it scans through the surf the deflections in the beam are captured by a Poisson sensitive photo detector (PSPD).

For the topography measurements performed a Bruker AFM Fast scan and Icon head are used, present in the Kavli Institute of Nanoscience, Delft. For the experiments performed a ScanAsyst mode with parameters optimization was used, which is Bruker patented Tapping mode. The scanners used have different physical limits, the Fast scan head has a scan limit of 30x30x3  $\mu\text{m}$ . While the Icon head has a limit of 100x100x10  $\mu\text{m}$ . Hence depending on the surface features height, an appropriate head was chosen.

These measurements are crucial in determining the peak height of features on the sample, based on which it is possible to determine the growth rate of pyramids. Moreover, it provides details of physical parameters like peak-valley height ( $S_z$ ), RMS surface roughness ( $S_q$ ), and Mean slope ( $S_{dq}$ ) that provide information as to how the surface morphology varies. The peak-peak height determines the difference in height of the highest point and the depth of the lowest point. While the RMS roughness determines the deviation of surface features' height from their average value. These two parameters are very much important to determine how the surface morphology height varies, crucial in reducing the texturing height.

### 3.7. Spectrophotometry

For conducting the optical measurements of varied surface morphology on a Si substrate a spectrophotometry setup Lamda 1050 by Perkin Elmer was used. This setup has two light sources, a deuterium arc lamp (D2 lamp) for ultraviolet (UV) light exhibited in the wavelength range of 300-320 nm and a tungsten halogen lamp used for a wavelength spectrum from 320-1200 nm. The range of light spectrum from these sources which strike on a diffraction grating, allows for selecting specific wavelengths of light to impinge on the sample. Later, the light travels through two detectors, a photomultiplier for UV light and PbS for the Infrared (IR) region of light. Since a switching occurs between these two detectors at 860 nm, a disturbance could be observed in most of the measurements. Since this deviation is very small and does not seem to impact the results negatively, no further action was taken to rectify this.

<sup>1</sup>Up/Down and side-side motion of the AFM probe

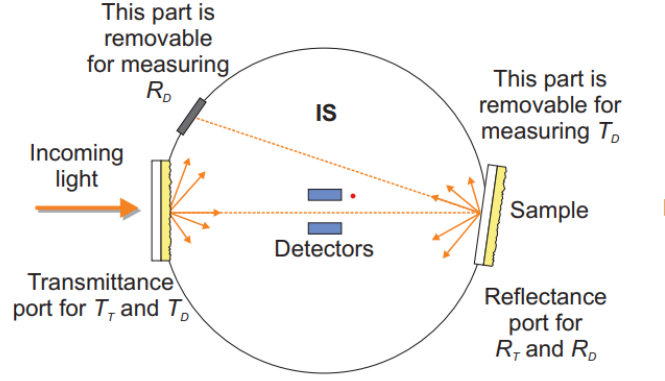


**Figure 3.9:** Schematic of the IS that measures the reflected and transmitted light by placing the sample at the front or backport of the sphere. Adapted from [38]

As the reflected or transmitted light needs to be detected for optical measurement (Reflection and Transmittance), the integrating sphere (IS) present does this work. It consists of a very highly reflective coated material. When the sample as shown in Figure 3.9 is placed at the back of an IS, it causes multiple internal reflections to take place in the IS. This allows for the measurement of Specular + Diffuse ( $R_T$ ) component of the reflected light. If the measurement of only the diffuse ( $R_D$ ) component is required then a square piece from the IS as shown in Figure 3.9. Since no subsequent supporting layers were measured on the Si sample, the transmittance measurements were not carried out. Moreover, the light that impinges on the sample falls at an angle of  $8^\circ$ , which remains the same for all measurements. Through this measurement setup, the total reflection of light can be measured in steps of wavelength, useful in determining the effectiveness of reducing the reflection losses. To further illustrate the effect of reflectance, the weighted average reflectance was used which normalizes the reflectance in a wavelength range as shown in Equation 3.7.

$$W_{ref} = \frac{\int_{400}^{1100} AM1.5(\lambda) * R(\lambda)}{\int_{400}^{1100} AM1.5(\lambda)} \quad (3.7)$$

### 3.8. Photoconducance lifetime measurement

Lifetime measurement is crucial for solar cells to determine the minority carriers' electrons or holes' lifetime before they decay back to the thermal equilibrium concentration after excitation. Photoconducance measurement help to determine this lifetime alongwith other parameters like implied  $V_{oc}$ , implied FF, and saturation current density ( $J_0$ ). In general, to determine the effective lifetime of a c-Si substrate, the bulk and surface recombination rates are considered as shown in Equation 3.8.

$$\frac{1}{\tau_{eff}} \approx \frac{1}{\tau_{bulk}} + \frac{1}{\tau_{surf}} \quad (3.8)$$

In the described Equation 3.8, the parameter  $\tau_{bulk}$  is related to the previously discussed Auger and Shockley-Read-Hall recombination. Another parameter  $\tau_{surf}$  related to the surface recombination determined by the surface recombination velocity. Since, CZ and FZ wafers are used for these tests, where  $\tau_{bulk}$  is large. Hence the previously defined Equation (3.8) is approximated to  $\tau_{surf}$ . Where the surface recombination relates to the (i)a-Si:H passivation layer deposited, the quality of this deposition will reflect in the lifetime measurement [70].

The effective lifetime in this thesis was determined by using phot-conducance decay method (PCM) through Sinton WCT-120 lifetime tester. It is done by solving the ambi - polar transport equation, which is defined for an  $n$ -type material, considering uniform generation rate and negligible electric field. This results in the effective lifetime in Equation 3.9. Where  $G$  is the generation rate for excess carriers (holes for  $n$ -type),  $\Delta p$  is the excess minority carrier hole concentration and  $\tau_{eff}$  is the minority carrier hole lifetime.



$$\tau_{eff} = \frac{\Delta p}{G - \frac{\partial \Delta p}{\partial t}} \quad (3.9)$$

Further, this method has two modes of calculating the lifetime. In each of these, the light is flashed for a different time period. One of the method is transient photoconductance mode, where a short pulse of light is illuminated that reduces rapidly. This gives out an assumption where the generation rate is negligible, deducing the lifetime as shown in Equation 3.9 to Equation (3.10). The other method, Quasi steady-state photoconductance method, involves flashing the light for a longer time period. This leads us to the assumption where the generation rate is much greater than the change in minority carrier concentration with respect to time and reduces the Equation 3.9 to Equation 3.11.

$$\tau_{eff} = \frac{\Delta p}{-\frac{\partial \Delta p}{\partial t}} \quad (3.10)$$

$$\tau_{eff} = \frac{\Delta p}{G} \quad (3.11)$$

The mentioned measurements were carried out in the PCD setup as shown in figure (3.10), which involves placing the substrate on a constant temperature plate with a xenon flashlight placed above it. When the light is flashed it induces conductance change in the sample, which is detected by a coil inductively coupled to a RF-bridge. This RF-bridge measures sheet conductance, which is later converted into an average excess minority carrier density ( $\delta P$ ) with the provided input data such as resistivity, optical constant, and substrate thickness. This analysis is carried out to mainly to calculate the effective lifetime for the (i)a-Si:H passivation layer deposited

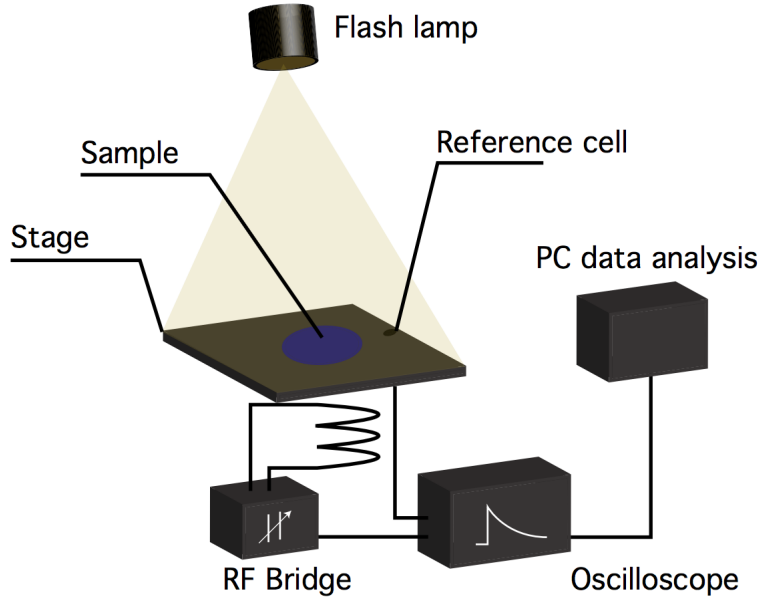


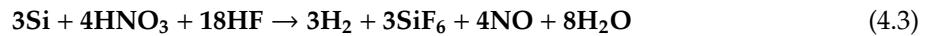
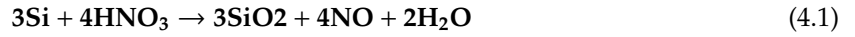
Figure 3.10: Schematic of Sinton WCT-120 instrument setup. Adapted from [46].

# Wet-chemical processing for varying surface morphology

## 4.1. Poly-Si etching : Top-down approach

As mentioned in Section 3.4 the conventional method of creating pyramidal features is by mostly employing alkaline texturing process. But, the height of these textures usually is in the range of 3-5  $\mu\text{m}$  [11], and hinder a quality deposition of the perovskite layer on the bottom cell. One way of reducing these heights is by following a top-down approach, where the height of created pyramids is reduced by a wet-chemical processing technique called as poly-Si etching. In this section, the effect of poly-Si etching in reducing the texturing height and its compatibility with the passivation layer deposition will be discussed.

This processing technique involves using HF and  $\text{HNO}_3$  in varying concentrations, with  $\text{H}_2\text{O}$  providing an isotropic etching. Moreover, it is also used as an additive for texture smoothening to help obtain rounded features [63]. Which is proven to be an economical way to improve the  $V_{oc}$  [71]. Here, the  $\text{HNO}_3$  solution creates an oxide layer, which is etched away by the HF reactant. A simple acid texturing process involves the following reaction steps [72],[73]:



Morphology properties	
RMS roughness (Sq)	0.429 $\mu\text{m}$
Peak height (Sz)	2.889 $\mu\text{m}$
Mean slope (Sdq)	47.9

**Table 4.1:** Morphological parameters of the AFM characterized CZ-wafers

In this experiment, n-type CZ-Si wafers produced by LONGI were considered for the top-down approach. Moreover, these wafers are already textured and have a peak height of 2.889  $\mu\text{m}$  obtained through AFM characterization as shown in Figure 4.1. Moreover, the usage of CZ wafers for solar cell production in the industry is predominant, this makes investigating on CZ wafers a more viable approach for industry scaling. The AFM analysis mentioned in Section 3.6 conducted provided the morphological information about the wafer surface as shown in Table 4.1. Since these wafers belong to the M2+ size category, their handling in the lab is difficult due to unsuitable wafer holders for such a large size. Hence, these wafers were cut into 4-inch size by using a laser cutter for relatively easier

processing. The characteristics mentioned in Table 4.1 act as a reference and help understand the variation in surface morphology with the poly-Si etching process.

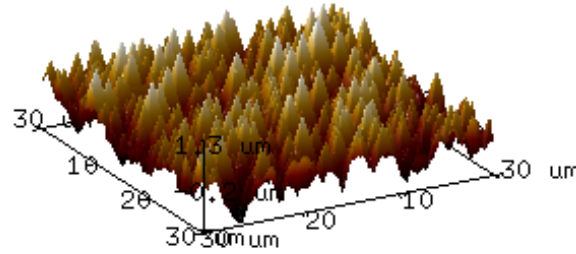


**Figure 4.1:** 3D height of an AFM characterized LONGI CZ sample.

Moreover, the laser-cutting process involved might contain residues of metal ions and other organic residues that can create defects. Hence, it requires wet-chemical cleaning techniques to remove such defects. Also, the chemical technique used to create pyramids on Si wafers will induce morphological changes. These changes will induce nano-scale roughness and chemical residues, which might impact the device's performance. For this reason, suitable wet-chemical techniques were evaluated to choose the most feasible procedure as mentioned in Section 3.4.1.

Hence, the process flow for these experiments begins with a cleaning step followed by a wet-chemical etching and passivation layer deposition. First, it is ideal to implement a cleaning technique to allow for removal of any contaminants that might result in performance reduction, with subsequent layer growth.

#### 4.1.1. Topographical characterization

To understand the morphology of the substrate after etching, AFM analysis and SEM characterization as described in chapter 3 was performed. First to understand the etching process, the wafers were etched for time steps of 6, 11 and 16 minutes. Prior to this, to activate the freshly mixed solution a Si wafer was immersed in the solution for 10-min. Later, the wafers were processed for the described etching time. A reduction in peak height along with a reduction in mean slope was observed from the AFM results obtained as shown in Figure 4.3 and Table 4.2.

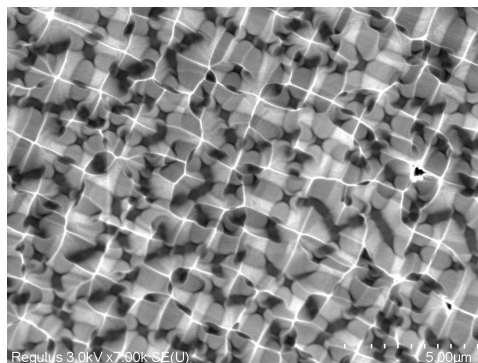


**Figure 4.2:** Top view inspection of 1.5 minutes poly-etched sample

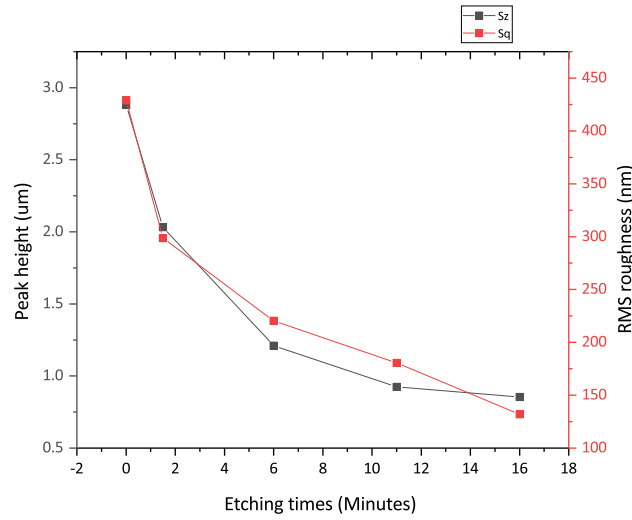


**Figure 4.3:** Variation in average peak height and RMS roughness for poly-etched wafers

Moreover, the subsequent topographical measurements (AFM) for poly-etched samples in the same solution showcased a deviation. As there was a variation in peak height observed for the subsequently etched samples in the same solution. The peak height at 6 min of etching deviated by  $0.25\mu\text{m}$  and the also mean slope by  $4.79^\circ$  as shown in Table A.1. This variation in height could also be analyzed from the SEM images, as shown in Figure 4.4 for a 6 minutes poly-etched sample. The surface, which had a very vigorous etching Figure 4.4b, resulted in flat crater like features between smaller pyramid peaks in comparison to the Figure 4.4a etched for the same time. Although this deviation in peak height has reduced for longer etch timings of 11 and 16 minutes to  $0.175\mu\text{m}$  and  $0.04\mu\text{m}$  as mentioned in Table A.3 and A.4 respectively. It showcases the variation in etch regime as more amount of Si is etched. Though, it is possible to observe a deviation in chemical kinetics due to random pyramidal height present. The poly-Si etching solution also exhibits very fast reaction to the newly mixed solution, which results in these deviations that can impact the reproducibility of results.

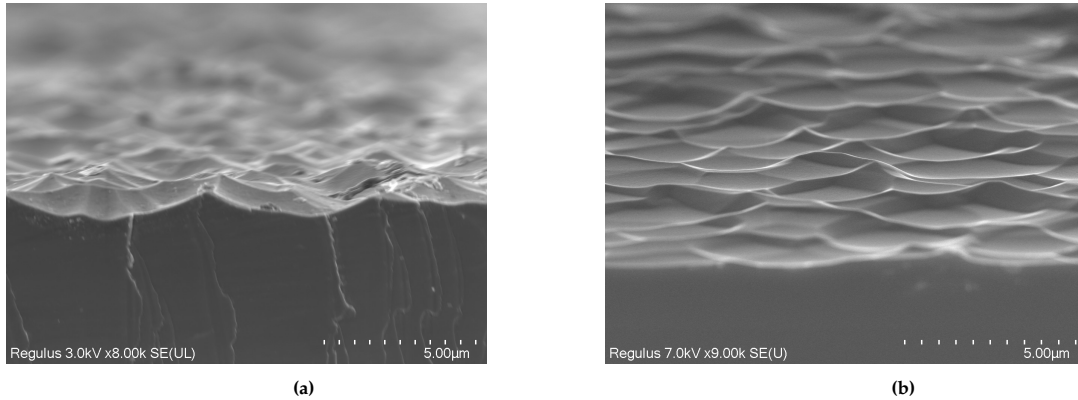


**Figure 4.4:** SEM inspection of 6 minutes poly-Si etched wafer, depicting the morphology at different instances of etching

The observed variability in the etching process is mainly due to parameters like, reactant concentration in solution, temperature, and Si dissolution. J. Acker [72] and M. Steinert [73] carried out a series of tests that revealed the solution's complexity and the involvement of intermediary processes. Contrary to common belief, the creation of NO and other chemicals does not take place directly through a precise process as mentioned previously in Equations 4.1-4.3. Where it begins with an  $\text{HNO}_3$  reaction, causing oxidation on the surface of Si, later with the removal of oxide by HF. However it occurs primarily, when nitric acid is reduced to N(III) compounds during this oxidation process, such as nitrite compounds ( $\text{NO}_2^-$ ). When these compounds come into contact with oxygen in the air at room temperature, a crucial

characteristic appears. The  $\text{NO}_2$  compound dissociates as a brown gas and further reduces to  $\text{NO}$  (a colorless gas), which no longer take part in the etching. As more amount of Si is immersed, the  $\text{HNO}_3$  is consumed and finally degasses as nitrous oxide causing the etching rate to change rapidly at room temperature conditions. Finally, to be able to maintain a constant etching rate it is required for these N(III) compounds to remain in solution. This is possible at lower temperatures like  $1^\circ\text{C}$ , where the nitride compounds are observed to be stable [73].

Another, important topographical variation noted from the SEM and AFM characterization is the shift in the pyramidal shapes to crater-like formations between the peaks. This transition occurs as a result of the etching solution's isotropic behavior, which uniformly etches the surface in all directions. Despite the presence of pyramidal peaks, etching produces recognizable craters between the pyramid and rounding of pyramid peaks. This rounding effect can be referred to as chemical-rounding [63],[74]

#### 4.1.2. Optical characterization

As the chemical rounding effect is affecting pyramidal texture samples to change their morphology. It is imperative to know the reflectance results for such changes. As shown in Figure 4.5, the reflectance measurements were performed for a wavelength range of 350-1200 nm. These results showcased an increase in reflection with increasing etching time. This reduction could be occurring because of the chemical rounding effect.

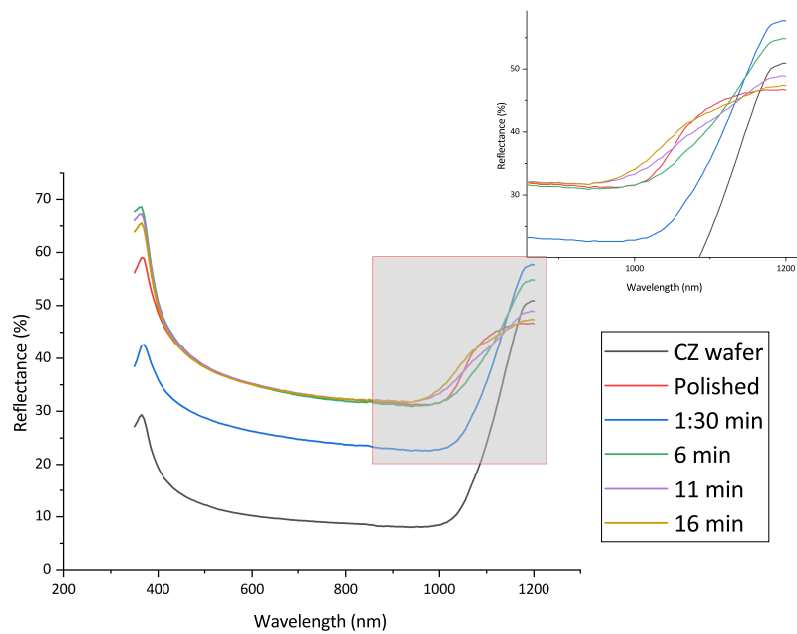


Figure 4.5: Reflectance measurement for poly-etched wafers at different etch timing

The steepness of pyramids as mentioned earlier in Chapter 2 plays a major role in increasing the light trapping with pyramidal features at the front surface. However, with increasing etching time this steepness gradually reduces from  $45^\circ$  to  $8^\circ$  as shown in Table 4.2, with increasing weighted reflectance (400-1100 nm). Since these reflectance measurements were only considered for the Si-air interface, a steepness of greater than  $45^\circ$  is proven for the light ray to undergo a double bounce effect.[75]. Furthermore, this increase in reflectance can be attributed to the aspect-ratio of these features (height/depth), which can exhibit reflectance similar to a flat sample if the ratio is less than 0.2 based on an experiment performed by Nishimoto [51] at a wavelength of 600nm . Moreover, the reflectance at a wavelength range of 1100-1200 nm is much higher compared to polished wafers. These could be occurring because of interference effects, resulting in higher reflection. But they are in particular much higher for textured samples, both CZ and poly-etched because of the light bending. Though this could not be verified, Angular reflectance measurements performed could provide a better understanding of these effects.

Etching times	Weighted Reflectance	Mean slope
Minutes	%	deg
0	10.749	47.9
6	35.44	25.6
11	35.88	12.5
16	35.831	9.52

Table 4.2: Effect of mean slope variation on weighted average reflectance

### 4.1.3. Passivation testing

To improve the minority carrier lifespan of Si wafers, an (*i*)a-Si:H passivated layer was deposited over the poly-Si etched wafer. The passivation process and operating conditions applied are as mentioned in Section 3.1.2.

It should be noted, however, that the above method passivation layer was originally optimized for a (100) oriented double-side polished c-Si surface with 5nm (i1) + 5nm (i2) layer thickness. But, the wafers utilized in this study have (111) oriented pyramids, resulting in features with a facet angle of 54.7 °C, which increases the effective area by 1.73 times. To accommodate for the increased effective area, the passivation layer deposition time was increased by 1.73<sup>1</sup>, allowing for 10nm bi-layer deposition.

The initial test was carried out on a wafer with no poly-Si etching, yielding a minority carrier lifetime of 223  $\mu$ s, as shown in Figure 4.6a. However, after etching the wafer in the poly-Si solution for 1.5 minutes with a peak height of 1.89 $\mu$ m as shown in Figure 4.3, the lifetime was drastically reduced to 2.4  $\mu$ s. The lifetime was reduced to 6.5  $\mu$ s when (*i*)a-Si:H was deposited on a 6-minute etched poly-Si sample with a peak height of 1.2  $\mu$ m.

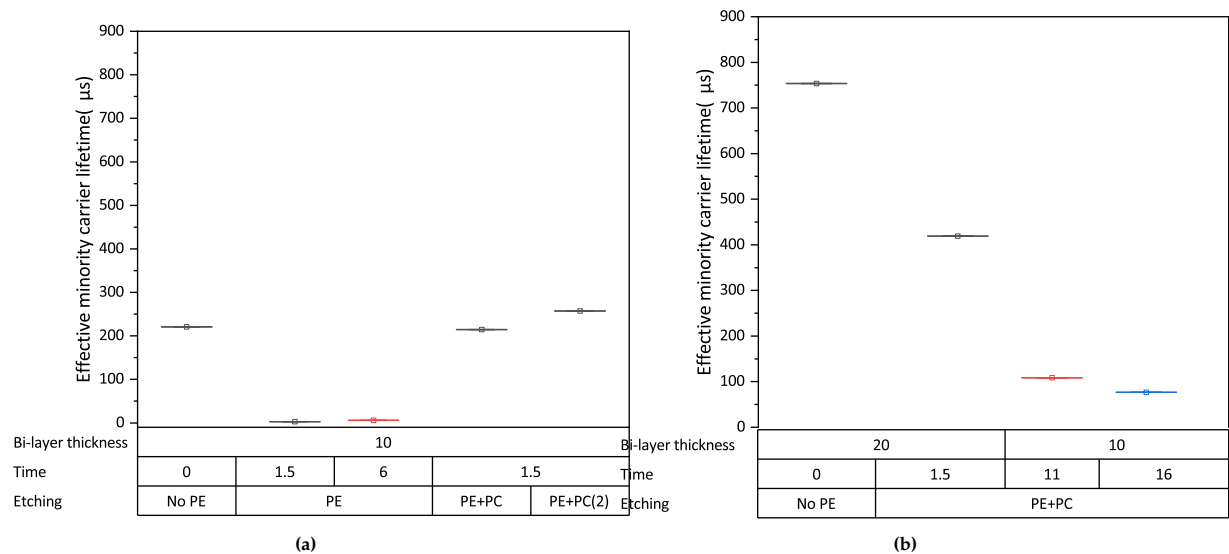
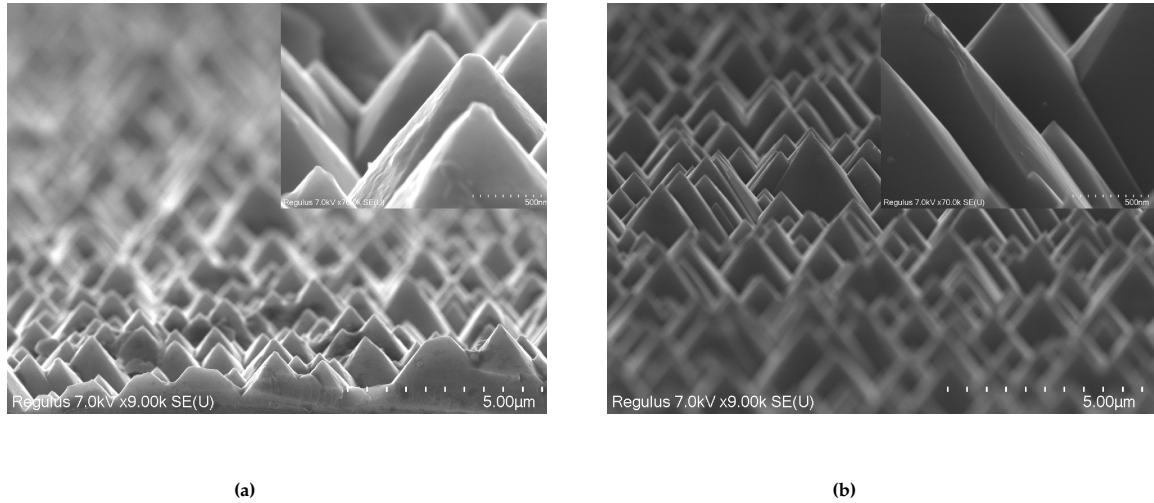


Figure 4.6: Lifetime measurements for poly-etched (PE) and post-cleaned (PC) samples with varying etching time and thickness.

In order to investigate the cause of this reduction, SEM images were analyzed for all etch timings after poly-Si etching and passivation layer deposition. The pyramids of the CZ samples that had not been cleaned had a minor roughness as shown in Figure 4.7. While utilizing the RCA-II cleaning process and depositing the (*i*)a-Si:H layer showcases a reduced roughness as shown in Figure 4.7b. After implementing the cleaning procedure and passivation layer deposition to the 1.5-minute etched sample as observed in Figure 4.8 still showcased a bumpy surface on the pyramids. But, the Lifetime of the sample as shown in Figure 4.6a has improved to 212  $\mu$ s. Which is a 98% increase in lifetime in comparison to the 1.5 minutes poly-etched wafer without any cleaning.

<sup>1</sup>It's important to emphasize that the mean slope of the pyramids changes with varied poly-etch times, making deposition of a comparable (*i*)a-Si:H thickness difficult, at the same enhancement factor



**Figure 4.7:** Cross-sectional SEM images of textured LONGI CZ wafers before cleaning (a) and after cleaning (b).

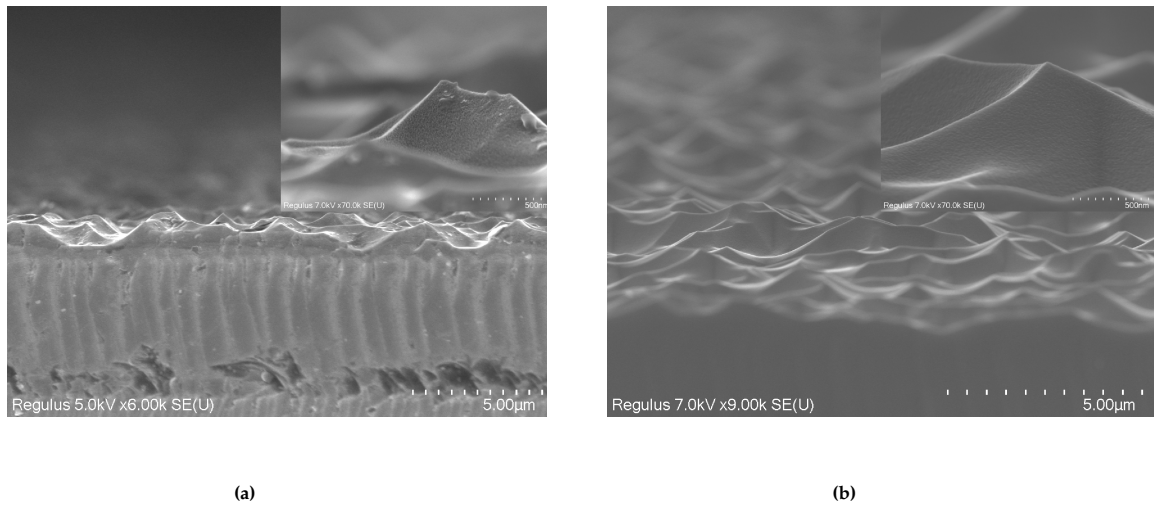


**Figure 4.8:** Cross-sectional SEM images of Poly-Si etched wafer after 1.5 minutes of etching, before cleaning (a) and after cleaning + passivation (b).

This emphasized the importance of chemical cleaning, as stated in the previous Section 3.4.1. As it proves to dramatically improve lifetime by reducing surface roughness. Passivation experiments were then performed on poly-Si etched wafers for 11 and 16 minutes, which resulted in the necessary sub-micrometer height. Given the topographical characterization results in Figure 4.3 and Table 4.2. They indicated that the difference in peak height and mean slope for these two samples was not significant, it was anticipated that applying the 1.73 factor would result in equivalent (*i*)a-Si:H thickness for both cases.

However, as seen in Figure 4.6b, the lifetime of these samples decreased as the etching time increased. This decrease in lifetime might be related to surface roughness that persisted after cleaning as observed in Figure 4.10. This was similar to the SEM inspection for 1.5 and 6 min etched samples. Most, importantly it could also be due to defects in the c-Si/(*i*)a-Si:H layer interface. Since at longer etching times, the sample had a lower peak height and a virtually flat surface, indicating a more favorable position for epitaxial growth [74]. Furthermore, due to the texturing present, the thickness of the a-Si:H layer presented was not calculated and is assumed to be around 13-15 nm considering the mean slope of the poly-etched sample. Because, deposition settings such as power, pressure, temperature and etc. were not optimized for the significantly thicker (*i*)a-Si:H, which may have contributed to the reported drop in a lifetime.

Moreover, the pyramid surface evaluated after the cleaning and (i)a-Si:H deposition showcased bumpy surface or nano-scale roughness for 1.5 minutes to 16 minutes etched samples in comparison to the wafer after cleaning and no (i)a-Si:H layer as shown in Figure 4.7. Though the minority carrier lifetime achieved at 1.5 minutes was almost similar for the poly-etched and without poly-etched wafer. It is speculated that the roughness scale present could be the (i)a-Si:H layer itself. But, the deposition of (i)a-Si:H is conformal and it occupies the shape of features present on Si unless it has a different growth mechanism.

Further, there is a possibility that the RCA-II cleaning was ineffective in removing this roughness for a poly-etched sample due its side-effects previously stated in Section 3.4.1. Also, the cleaning process could only remove the roughness of a few nano-meters in scale, which led to incomplete removal after cleaning. To evaluate if implementing more cleaning steps could remove this issue the 1.5 minutes poly-etched wafer was subsequently cleaned twice (PE+PC(2)). This resulted in a similar lifetime of 232  $\mu$ s as shown in Figure 4.6a. It reveals that apart from the roughness present, the c-Si/(i)a-Si:H interface has other defects limiting their improvement.

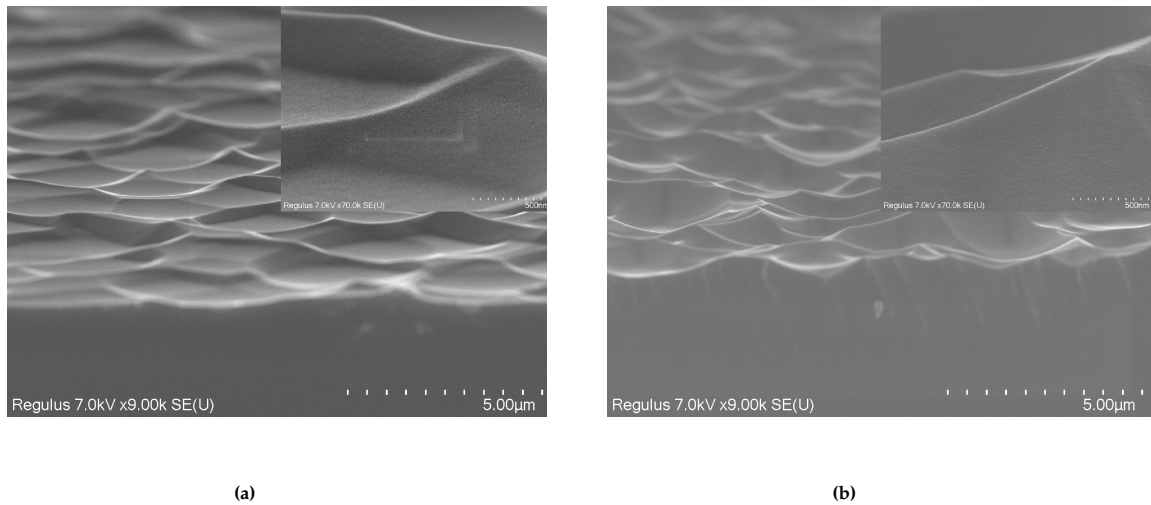


**Figure 4.9:** Cross-sectional SEM images of Poly-Si etched wafer after 6minutes of etching, before cleaning (a) and after cleaning + passivation (b).

It is also significant to note that for all poly-Si etched wafers the same enhancement factor was applied. This particular observation suggests that due to the variation in mean slope from  $47^\circ$  to  $9^\circ$ , the deposited thickness is likely to be between 10-20 nm of thickness for reducing mean slope. An investigation on the effect of (i)a-Si:H was performed by Deligannis [70]. They indicated that the lifetime increases with higher passivation layer thickness, as it becomes less dependent on the surface recombination.

To further understand if a higher thickness of (i)a-Si:H could provide better lifetime results to the poly-etched wafer. The previously considered (i)a-Si:H layer thickness (10 nm) was doubled to 20 nm (10nm (i1) + 10nm (i2)), which indicates that the enhancement factor was changed to 3.46. First, the passivation test was performed on a sample that had not been etched with poly-Si, and the lifetime practically tripled, reaching 750  $\mu$ s, as shown in Figure 4.6b. When compared to the previous deposition example of a 10nm bi-layer, these results showcased an improvement. This increase could be attributed to the effect of thicker passivation layers, which reduce the surface recombination[70]. Moreover, a 1.5-minute poly-etch solution that was cleaned has also indicated an increased lifetime to 450  $\mu$ s as shown in Figure 4.6b. Though the lifetime increased in comparison to the previously experimented 10 nm passivation layer, it could not reach the lifetime of 750  $\mu$ s for the CZ wafer with RCA-2 cleaning. This could be occurring because of the deviations in deposition conditions and the previously attributed nano-scale roughness.



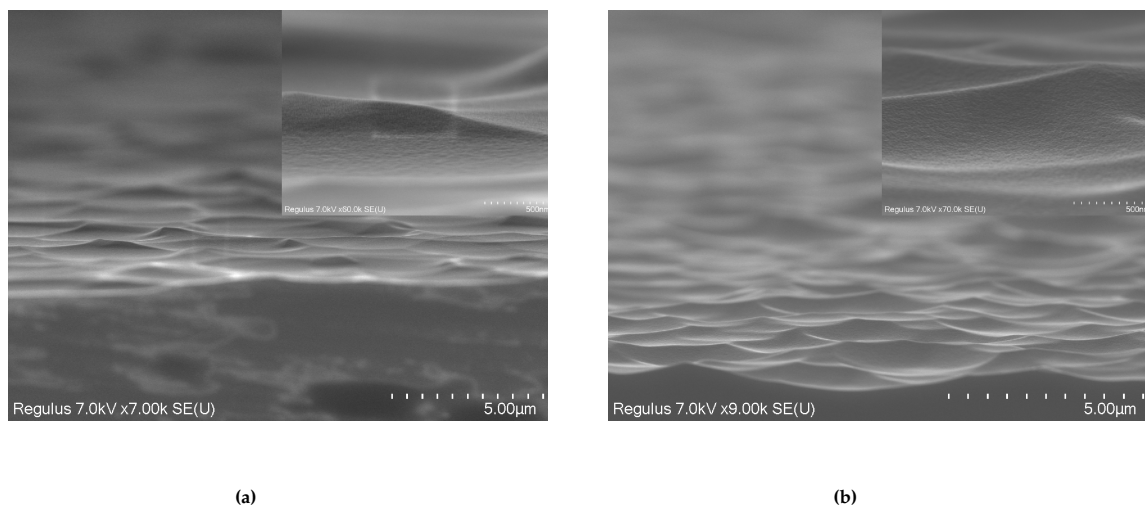


**Figure 4.10:** Cross-sectional SEM images of Poly-Si etched wafer after 16 minutes of etching, before cleaning (a) and after cleaning + passivation (b)

Due to time constraints, these previously mentioned deviation factors could not be fully investigated. Nevertheless, the results obtained strongly suggest that raising the *(i)*a-Si:H layer's thickness can produce passivation that is both efficient and effective. But comparing the results for 10 nm bi-layer deposited for 1.5, 11 and 16 minutes poly-etched wafer. The 11 and 16 minutes sample have showcased lower lifetimes despite cleaning and having a slightly higher thickness (due to a lower slope).

This indicates further verification is required to find the potential reason behind this decline in lifetime with increasing etching time by optimizing the process parameters (Pressure, temperature and etc.) and cleaning technique. Therefore, it was decided to focus on investigating alternate approaches to eliminate the flaws (roughness) generated by poly-Si solutions by changing the solution concentration.

#### 4.1.4. HNA etching

The acid-texturing process is not limited to the consideration of HF and HNO<sub>3</sub> for isotropic etching, additions of chemicals like CH<sub>3</sub>COOH (acetic acid) and H<sub>3</sub>PO<sub>4</sub> can be used for making smooth surfaces [76]. With the hydrophobic nature of Si wafers these solutions, provide better wettability and inhibit better etching[77].

Considering the drop in passivation after poly-Si etching due to surface roughness, it is understood that the solution is introducing or forming a defective surface which led to lower lifetimes. This could also be the same reason for the 1.5 minutes poly-etched sample could not reach the lifetime similar to CZ wafer without any poly-etching as shown in Figure 4.6b. To understand if better surface wettability agents in the solution can reduce the vigorous oxidation process causing high surface-induced roughness. It is necessary to change the constituents of poly-Si etching. Subsequently, the poly-Si etching was replaced with hydrofluoric acid (40% HF), nitric acid (69.5% HNO<sub>3</sub>) and acetic acid (99.5% CH<sub>3</sub>COOH in the ratio 1:6.3:1 [76] and is referred to as the HNA etching.

#### Topographical characterization

Compared to the previous poly-Si etching solution which was able to reduce with longer etching times greater than 6 minutes. The HNA solution showcased a much faster etching with the initial tests performed for 25s and 50s. Hence, it was decided to perform etching at 1.5, 2, 2.5, 3, and 4 minutes to observe the peak height reduction. These solutions require a pre-etching to activate the oxidizing agents for etching to take place [72]. So, a pre-etching was done for 10 minutes similar to the poly-Si etching scenario.

To find out, if the previous issue of solution etch regime varies with more Si being etched. It was first experimented to find if there exist any deviations in peak height, in the same solution. It was observed that with reducing peak height as shown in figure 4.11 for 2 min and 1.5 min there is considerable height deviations of 0.238 and 0.138 µm as shwon in Table A.6 and A.5 respectively. Eventually, as the peak height dropped, the deviation in height gradually decreased, to approximately 0.08 µm for 2.5 min and

3 min of etching time as shown in Table A.7 and A.8 respectively. These results in comparison to the poly-Si etching showcase a similar offset in etch regime, where only the samples initially etched for 1.5 minutes suffered the largest deviation.

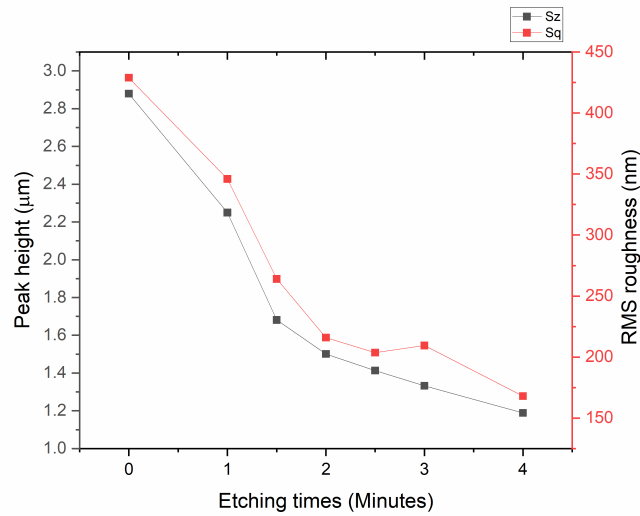


Figure 4.11: Variation in peak height and RMS roughness for HNA etched wafers.

### Optical characterization

Illustrating the optical property (reflection) measured for the varying etch rate of HNA etching from 1.5 min to 4 minutes. As showcased in Figure 4.12, an increasing etching time resulted in a higher reflection. This could be related to the reduced mean slope as previously stated in poly-Si etching, which was also observed to decrease for HNA as shown in Table 4.3. However, comparing the optical properties of these two etching solutions. The weighted average reflectance was the same in the wavelength range of 400-1100 nm. But when compared in the regime of 800 - 1100 nm, the HNA etch solution has relatively lower reflectance at a smaller peak height. This could be because of the higher mean slope the HNA solution has, which might have resulted from a slightly higher crater depth causing reflected light to undergo a second bounce. Also reduced interference effects at longer wavelengths, which are yet to be verified.

Table 4.3: Effect of weighted average reflectance and mean slope variation for HNA etched sample

Etching time	Weighted Reflectance	Mean slope
Minutes	%	deg
1.5	31.8582	29.6
2	32.122	24
2.5	34.08	17.2
3	35.465	17.2
4	35.815	16.6

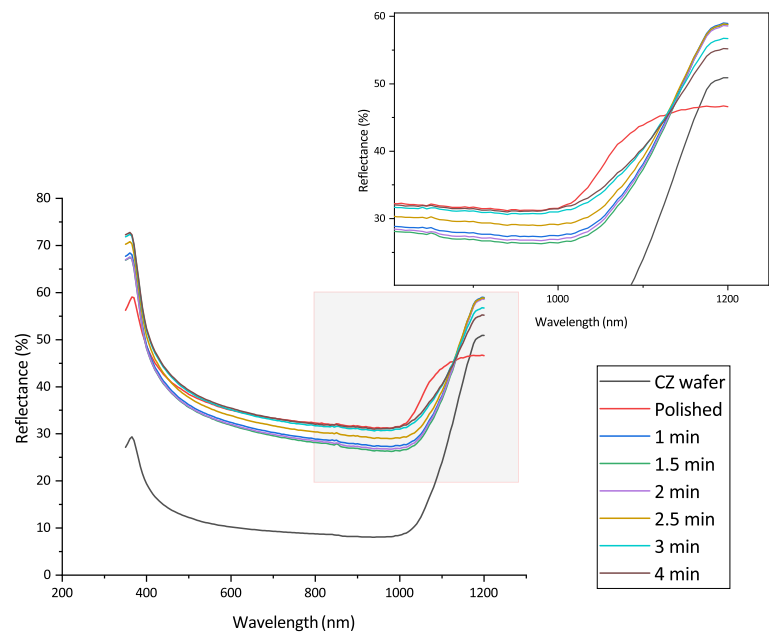


Figure 4.12: Reflectance measurement for HNA-etched wafers at different etch timing

Intriguingly, comparing these reflectance measurements to those of a polished flat FZ wafer for the wavelength range of 900-1100nm in Figure 4.12. Indicate that HNA modestly lowers optical losses for wavelengths of 1050 - 1100 nm by 4% at 2.5 min of etching in comparison to flat samples. The poly-etch samples, as seen in Figure 4.5, show no signs of a reduction as of 6 minutes and higher etching time.

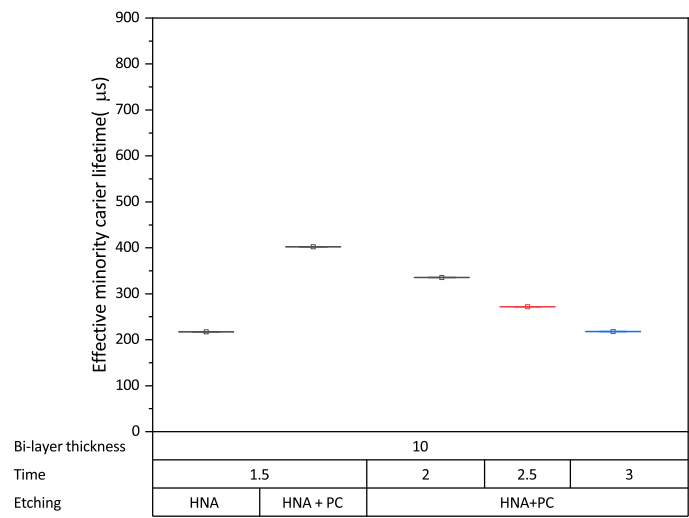
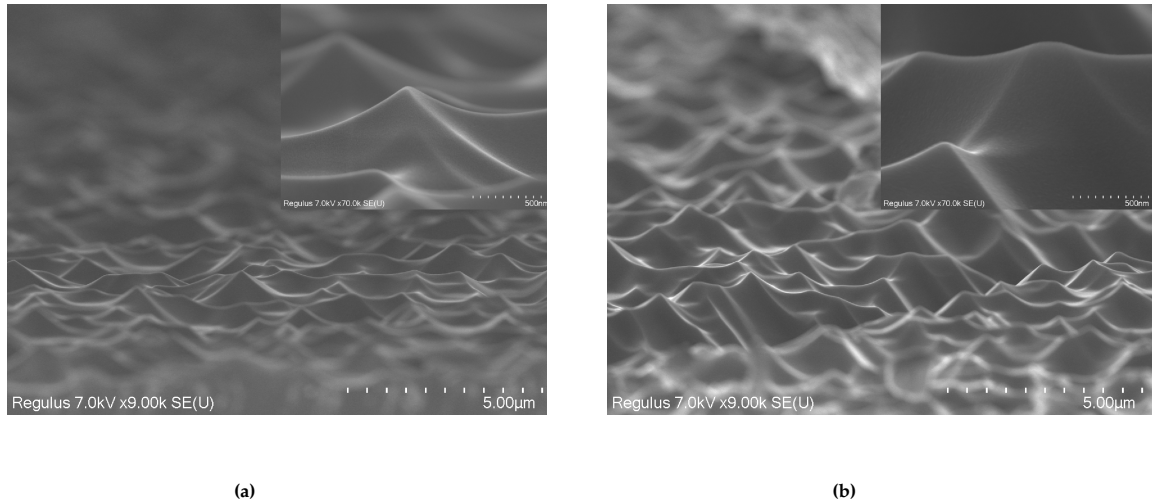


Figure 4.13: Lifetime measurements for HNA etched samples with 10nm bi-layer thickness.

Passivation testing

The main reason for adding acetic acid ( $\text{CH}_3\text{COOH}$ ) was to investigate if it can reduce the surface-induced roughness and result in lifetime improvements. This experiment began with an etching time of 1.5 minutes and an enhancement factor of 1.73. Intriguingly, Figure 4.13 shows that the lifetime observed in this example was 192  $\mu\text{s}$ . According to Figure 4.6a, this value was significantly larger than the lifetimes observed for any poly-etched sample that had not been cleaned. This evident improvement

can be attributed to the surface roughness being reduced, as seen in the SEM picture of the 1.5-minute HNA-etched sample shown in Figure 4.14. The lifetime subsequently increased significantly to 402  $\mu$ s after the cleaning method was integrated, as shown in Figure 4.13. This improvement might also be attributed to the sample's surface being noticeably smoother in the SEM picture taken after the passivation layer was deposited, as seen in Figure 4.14b. After the passivation layer was deposited, the HNA-treated sample still had some bumpiness, but it was noticeably less obvious than the features that the 1.5-minute poly-etched wafer displayed (see Figure 4.8b). This demonstrates that the presence of surface roughness has led to high bumpiness rather than the (i)a-Si:H growth that was speculated. To further know if this increase in lifetime is related to surface-induced roughness, it is necessary to investigate NAOC cleaning after poly-Si etching which showcased a higher lifetime [74],[66].



**Figure 4.14:** Cross-sectional SEM images of HNA etched wafer after 1.5 minutes of etching, before cleaning (Left) and after cleaning + passivation (Right).

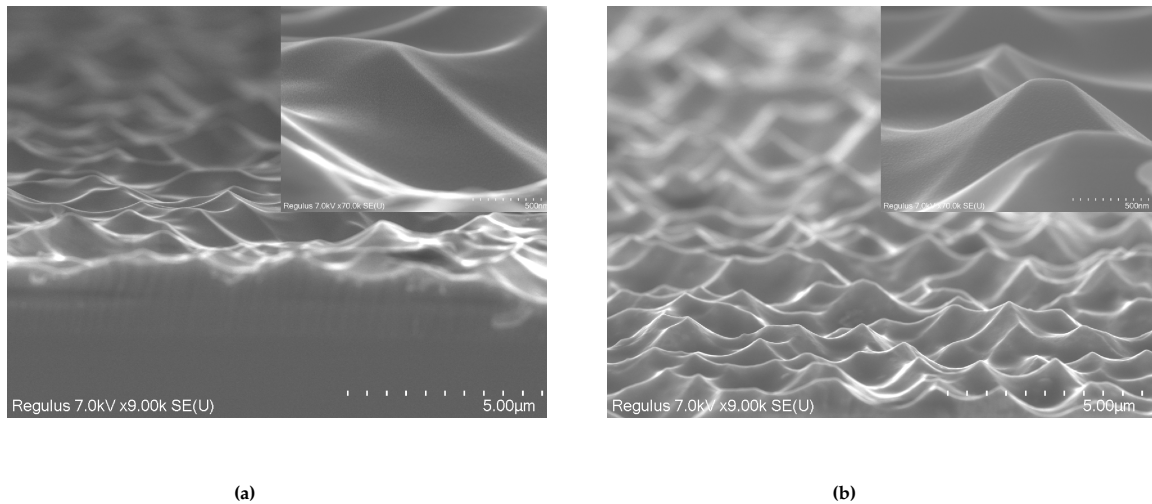


**Figure 4.15:** Cross-sectional SEM images of HNA etched wafer after 2 minutes of etching, before cleaning (Left) and after cleaning + passivation (Right).

Though, the HNA has proven to reduce the surface-induced roughness by reducing the evolution of different intermediaries and providing a uniform wettability of oxidizing agents on the Si surface. The effect of minority carrier lifetime for the desired texture height at 2, 2.5, and 3 minutes after cleaning and passivation layer deposition was investigated. Interestingly, the lifetime was comparatively higher than for 2 and 2.5 minutes etched compared to 3 minutes etched sample as shown in figure 4.13. The similar

effect of the lifetime decrease for poly-Si etched wafers was also observed with increasing time in the HNA solution. This can again be attributed to the insufficient passivation of the deposited layer due to improper deposition conditions. Moreover, by investigating the surface roughness for these HNA samples after 2 and 3 minutes of etching as shown in figure 4.15 and 4.16 has similar roughness..

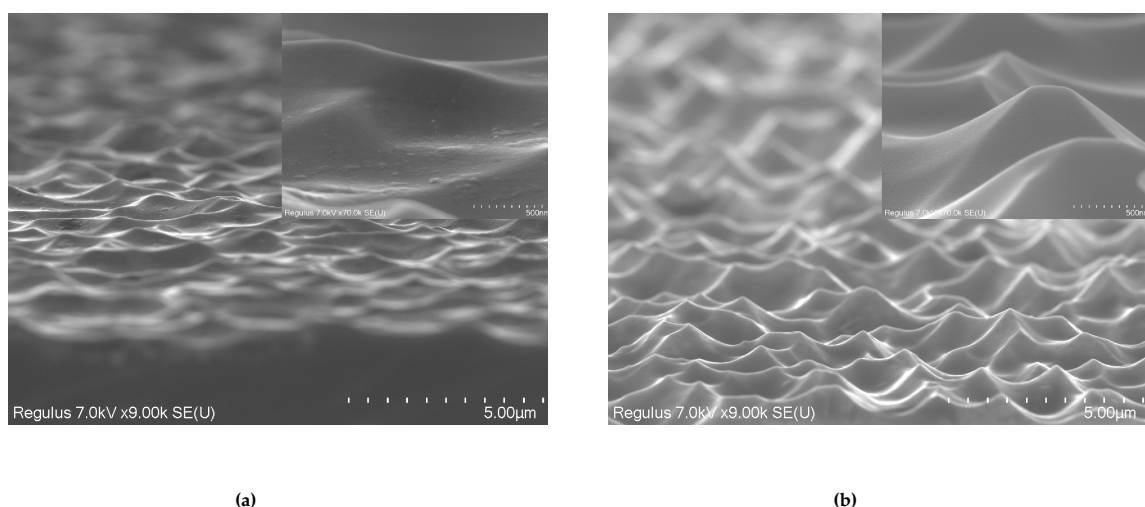


**Figure 4.16:** Cross-sectional SEM images of Poly-Si etched wafer after 3 minutes of etching, before cleaning (Left) and after cleaning + passivation (Right).

From the above observations made it can be summarized for poly-Si etching and HNA etching that a reduction in peak -height is achievable but with an increase in the overall reflectance for the wavelength range of 350-1200 nm. This is attributed to the decreased mean slope which reduced the double-bounce effect. Later, the passivation test performed for the poly-Si etched samples indicated that a bumpiness on Si surface existed after cleaning and deposition. This is speculated to be occurring either due to (i)a-Si:H growth or insufficient roughness removal. But, the results from HNA etching indicated a reduced roughness with slightly lower bumpiness. This confirms that the bumpiness is more prevalent because of the roughness still present rather than the (i)a-Si:H growth. These results necessitate the investigation of introducing better cleaning and optimized deposition conditions.

## 4.2. Creation of nano pyramids though chemical texturing

It is important for us to develop nano textures on flat Si substrate as presented in 1.2 and chemical techniques are a preferred way to do so for cost-effectiveness and industry compatibility. Metal-assisted chemical etching (MACE) which was introduced in 1997 with aluminum, is a process typically involving metal particles that withdraw electrons from the vicinity of silicon (catalyzing <sup>2</sup>), these also act as a mask that allows for anisotropic etching by relevant chemicals to create pyramidal etch.[78].

The development of nucleation sites is crucial for the creation of nano pyramids, as they directly relate to the number of pyramids being formed. Metal nanoparticles play a crucial role in creating such nucleation sites through a bottom-up approach. The experiments performed using the MACE process involve the following chemicals AgNO<sub>3</sub>, CuNO<sub>3</sub> and etc which have been used to create sub-micrometer features [79],[80]. The mechanism behind this process which was considered using AgNO<sub>3</sub> solution involves, firstly, the reaction of the Si with an alkaline solution. This reaction produces H<sub>2</sub> bubbles and these are undesirable as they prevent further chemical reactions, resulting in poor nucleation. So to destroy these bubbles generated certain surfactants such as TK-81, whose chemical composition is undisclosed are used. Further, the Ag nanoparticles which were present on the Si surface act as a masking material to allow for pyramidal features to be created. Through this process, an average pyramid size of 500nm was achieved. [79]. Also based on a similar mechanism CuNO<sub>3</sub> particles are used to create nano textures[80]. Since these Cu and Ag particles have a smaller size they have been reported to reduce the size of pyramids created.

<sup>2</sup>It facilitates that charge transfer between silicon and metal which acts as an oxidizer

However, metals are eventually undesired particles on a Si substrate as they induce shockley-read-hall recombination due to which the cell performance degraded[81]. So it was decided to investigate other chemicals which can be used to create nano textures without compromising the electrical performance of the device. Based on the literature study, certain chemicals like  $\text{Na}_2\text{SiO}_3$  and  $\text{K}_2\text{SiO}_3$  were experimented with and have produced reliable performance adjacent to the creation of nano textures [82],[13],[36].

The experiment, done by mixing  $\text{SiO}_2$  based glass particles and SUN-X600 (a mixture of KOH), led to submicron textures with size ranging from 0.3-2  $\mu\text{m}$ . The glass particles helped to reduce the  $\text{H}_2$  bubbles providing a better height reduction. Since the solution without glass beads generated  $\text{H}_2$  bubbles due to the chemical process as in Equation 4.4, which act as a mask preventing texturing to proceed.



While experiments done with addition of  $\text{K}_2\text{SiO}_3$  indicated much more promising results as the texturing height was further reduced. Initially, this experiment was carried out on a p-type CZ wafer with (100) orientation by the SERIS group in Singapore. [83][84]. The results indicated that by tuning the alkaline solution concentration, temperature of solution and  $\text{K}_2\text{SiO}_3$  concentration the texturing height varied from 5 to 8  $\mu\text{m}$ , with average efficiencies ranging from 18.4-18.6%. Most importantly, it was observed that the addition of  $\text{K}_2\text{SiO}_3$  led to a reduced etching rate.

Further experiments performed with  $\text{K}_2\text{SiO}_3$  and solution containing KOH and ALKA-TEX (a commercial additive) yielded sub-micron scale features[85]. By varying the concentration of  $\text{K}_2\text{SiO}_3$  an average pyramid size ranging from 62 to 512 nm was obtained. Further, the passivation results with (i)a-Si:H resulted in a value from 1.5 to 3 ms. So based on these results, it was decided to consider  $\text{K}_2\text{SiO}_3$  for experiments as it showcases to be a promising alternative to achieve the objective of creating sub-micrometer texture with optimum passivation.

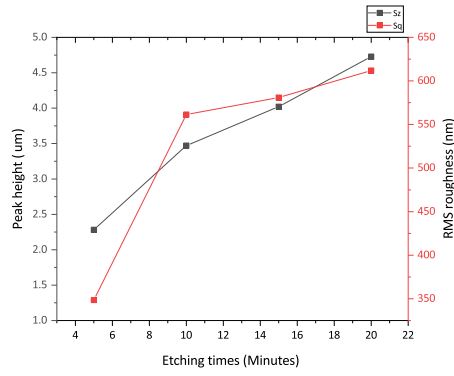
#### 4.2.1. Texturing process

In the texturing process involving KOH, the Si wafers react with the KOH to produce  $\text{K}_2\text{SiO}_3$  and  $\text{H}_2$  bubbles as shown in equation 4.4. As briefly discussed in Section 3.4, how the alkaline texturing process works. A similar mechanism also seems to be applicable here. Moreover, the  $\text{H}_2$  bubbles which are generated as a byproduct of the reaction process are undesirable as they act like a mask preventing the etching process to continue. Hence commercial additives from Rena GmbH are used to achieve a better uniform texturing process.

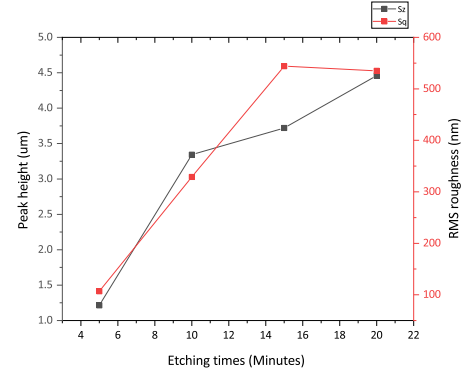
This experiment involves using the chemicals  $\text{K}_2\text{SiO}_3$ , KOH and surface additive monoTEX H3.5 and H2.6 from RENA GmbH. These surface additives were used for a certain set of experiments, which will be indicated at those sections. Unlike the previous, where we have reduced the peak-height through a top-down approach, the texturing process investigates in the growth of pyramids which have a smaller height. For this reason experiments were performed using n-type FZ wafers (double-side polished) with a thickness of 280  $\mu\text{m}$ . The solution was prepared in a 4.2 L beaker placed on a hot plate with respective concentrations. All the initial experiments were conducted at 80°C to optimize the concentration of additives in the solution before moving to the temperature dependence. To optimize the sub-micrometre textures the chemical compounds KOH,  $\text{K}_2\text{SiO}_3$  and monoTEX concentrations impacting the etching parameters are first analyzed to find their appropriate weightage. Moreover, the physical state of the KOH and  $\text{K}_2\text{SiO}_3$  chemicals is solid hence their presence in the solution is expressed through wt / vol(%) metric. It is important to note that the surface additive was added 5-10 mins before the immersion of wafers for effective additive usability. During this process, it is also necessary to place a dummy wafer inside the bath to activate the solution.

In addition, to provide a more complete depiction of the impact of  $\text{K}_2\text{SiO}_3$  and KOH concentrations within the solution, the F-ratio was considered. This F-ratio effectively represents the ratio of  $\text{K}_2\text{SiO}_3$  and KOH (wt./vol %) in the solution. Understanding how fluctuations in the concentrations of these components affect the overall texturing process may be achieved will be detailed in the coming sections.

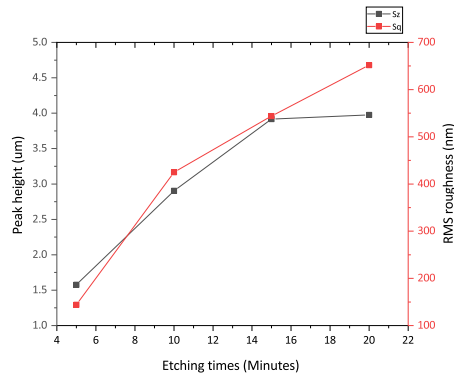
It's worth mentioning an essential factor that influenced the experimental strategy, the impacts of  $\text{K}_2\text{SiO}_3$ . Since the experiments performed made it visibly clear that  $\text{K}_2\text{SiO}_3$  did not become soluble in water until the temperature crossed 80°C. Hence, it was decided to examine the effects of temperature once the solution concentration is optimized for sub-micron height features.



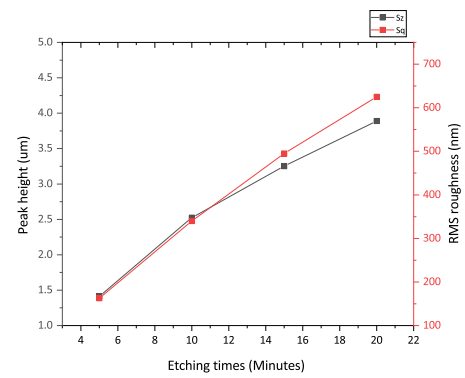
(a) Variation in surface morphology for F=0.5.



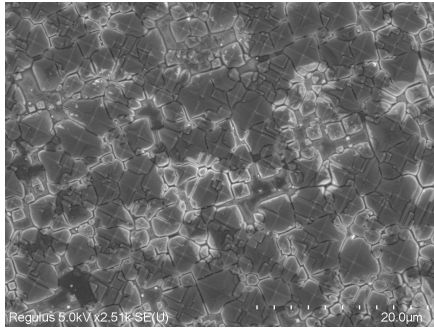
(b) Variation in surface morphology for F=1.0.



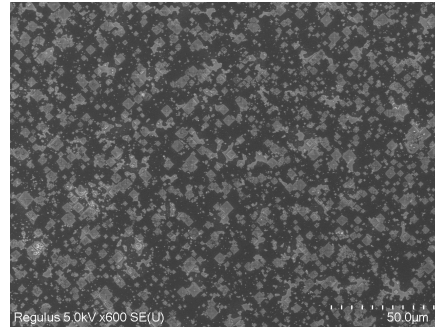
(c) Variation in surface morphology for F=1.5.



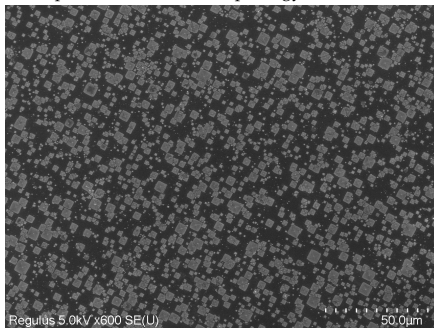
(d) Variation in surface morphology for F=2.0.

**Figure 4.17:** Variation in peak height and RMS roughness for increasing  $K_2SiO_3$  addition.

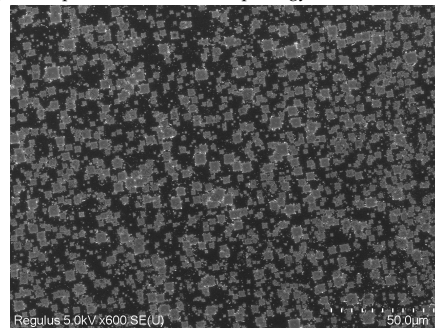
(a) Inspection of surface morphology for F=0.5 after 10 minutes of etching.



(b) Inspection of surface morphology for F=1.0 after 10 minutes of etching.



(c) Inspection of surface morphology for F=1.5 after 10 minutes of etching.



(d) Inspection of surface morphology for F=2.0 after 10 minutes of etching.

**Figure 4.18:** SEM inspection of surface morphology at different  $K_2SiO_3$  concentrations.

### 4.2.2. Effect of $K_2SiO_3$

It is crucial to first understand how texturing variables like the etching rate and density of pyramids affect regulating the height of the etched features. To achieve the optimum weight-to-volume (wt/vol) ratios of KOH,  $K_2SiO_3$ , and the surface additive must be carefully taken into account. As a first step, the impact of  $K_2SiO_3$  on the pyramid height and density must be carefully considered while keeping the KOH concentration constant, despite the fact that this material has been found to contribute to reducing the peak height

So the experiments were performed in four batches from  $F = 0.5$  to  $F = 2.0$ , with 4 samples per batch to find the variation on pyramid formation for every 5 minutes. The result for the height distribution with varying etching time at  $F = 0.5$  as shown in Figure 4.17 indicate that there is an increasing etching rate, which is evident from the increased peak height. Moreover, the RMS roughness also correlates with the increase in height, which showcases that the height deviation of pyramid size increases with etching time. Inspecting the density of the pyramids as shown in Figure 4.18a and 4.19a for 5 and 20 minutes of etching indicate a good pyramid homogeneity as the etching time increases. However, the peak height for these samples is above  $3\ \mu m$  which is not the ideal case required to be obtained. Further, by observing the result at the highest  $K_2SiO_3$  concentration considered,  $F = 2.0$  as shown in Figure 4.17d. Indicate that peak height has increased from  $2.6\ \mu m$  after 5 min of etching to  $3.2\ \mu m$  after 10 minutes. Moreover, the RMS roughness has slightly reduced in comparison to  $F=0.5$ , due to the lesser etching rate. Yet, the reduction in roughness indicated is still higher than the minimum thickness limit of perovskite, which would not support the deposition of the perovskite layer.

These results showcase the effect of increasing the peak height with etching time, similar to the  $F=0.5$  results. However, a reduction in peak height is observed for an increase in  $F$ -ratio from 0.5 to 2.0. This clearly correlates to the effect that a higher  $K_2SiO_3$  concentration results in reduced peak height. which is 44% and 16% at  $F=2.0$  after 10 min and 15 min of etching. But, by verifying the SEM images as shown in Figure 4.18d and 4.19d for etch timing after 10 and 20 minutes respectively. The pyramid density still seems to be non-homogeneous after 20 minutes.

To verify these results, experiments for  $F = 1.0$  and  $F = 1.5$  were conducted. Observing the peak height variation with etching time as shown in Figure 4.17b and 4.17c. They do indicate a reduction in peak height observed up to 10 minutes of etching relative to the  $F=0.5$  results as shown in figure 4.17a. Further verifying the SEM images for 20 minutes for  $F=1.0$  and  $F=1.5$  as shown in Figure 4.19b and 4.19c respectively. There is still non-homogeneous pyramids formation at  $F=1.5$  still has plenty of non-homogeneity in pyramid formation similar to  $F=2.0$  as shown in Figure 4.19d. These observations illustrate that  $K_2SiO_3$  concentration is only able to reduce the etching rate and not the size of pyramids. Since the pyramid height increases further with longer etching time and providing a good pyramid homogeneity.

To decipher these effects of reduced peak height and nucleation of pyramids it is necessary to look back at the chemical reaction of KOH etching as mentioned in Section 3.4. where  $OH^-$  ions is one of the reaction product, causing the oxidation to occur. It is clear from the above results that with increasing  $K_2SiO_3$  concentration, there is a lower etching rate and bad pyramid density. In the first case, a lower growth rate is achieved due to the increase in reaction-by-product ( $K_2SiO_3$ ), shifting the reaction equilibrium to the right-hand side. Along with a reduction in the homogeneity of pyramids nucleation, due to hindrance of  $OH^-$  ions from participating in the reaction effectively [83].

From these observations, it is evident that  $K_2SiO_3$  can limit the oxidation process, but cannot control the homogeneity of pyramids. Since this is based on the reaction of  $OH^-$  ions with Si and it requires the desorption of products from the surface.



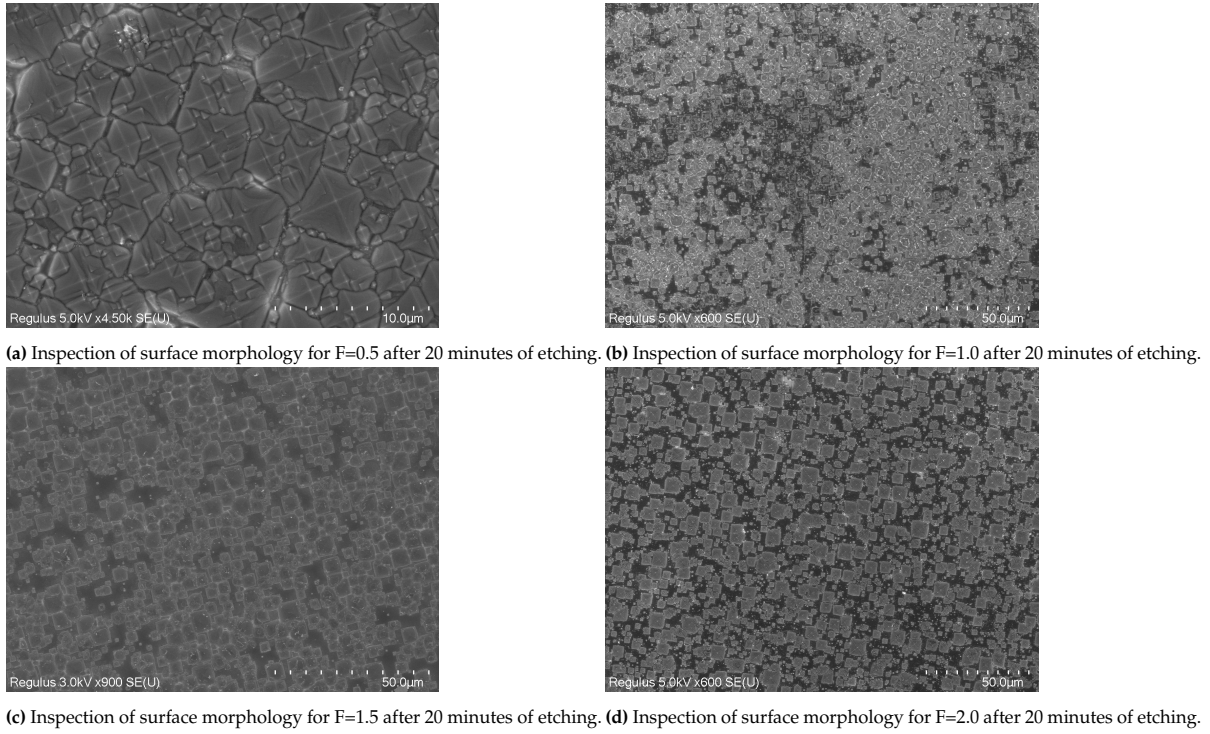


**Figure 4.19:** SEM inspection of surface morphology at different  $K_2SiO_3$  concentrations.

Further, the analysis of the optical property, as shown in Figure 4.20 on the reflected light from Si wafers etched at various concentrations and etching times. It adds back to the previous notion that increasing etching time provides reduced reflection, due to more homogeneous pyramid formation. This pattern is visible in the majority of the graphs, as the reflectance steadily drops as the etch rate increases.

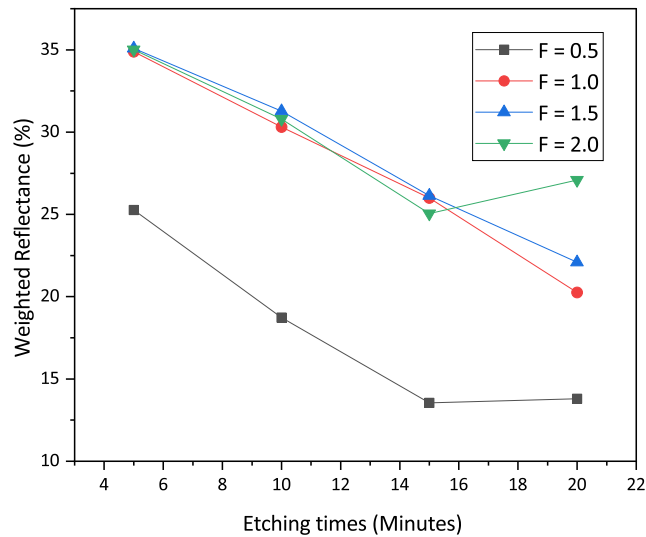


**Figure 4.20:** Weighted average reflectance variation for different F-ratio concentration.

It is crucial to note that, the reflectance rapidly jumps from F=0.5 to F=1.0 and then steadily decreases at longer etching periods. First, the slower etching rate that began after F=1.0 is the likely source of

this rapid increase where many non-homogeneously spread pyramids are present. Despite the fact that increasing etching time can provide better pyramid density, it is not apparent when measuring reflectance until 15 minutes. But after 20 minutes, a noticeable change can be observed, due to the increase in pyramid density with increased etching time. This was also visible in the 20-minute SEM pictures, as seen 4.19. Where the nucleation seems to be lesser for  $F=1.5$  and  $F=2.0$  and also have a higher reflectance.

### 4.2.3. Effect of additive concentration

To understand the impact of the surface additive monoTEX (MT) H3.5 and H2.6 on the Si etching and wettability, the experiment was conducted at  $F = 0$  (the  $K_2SiO_3$  concentration is 0) while the KOH concentration was maintained at 0.7%. In the following experiments to be mentioned in this section, the monoTEX H3.5 concentration was varied from 1.4% to 2.4%, while including MT H2.6 for 5.5% of additive to understand the effect of pyramid peak height and etching. As shown in Figure 4.21 the peak height was observed to be highest for MT concentration of 1.4% which further increases with higher etching time. However, this peak height is comparatively lower than the solution without any additive concentration as shown in Figure 4.17 for  $F$ -ratio from 0.5 to 2.0. Moreover, the nucleation of pyramids at 1.4% MT through the SEM analysis performed as in Figure 4.23a for 10 minutes, showcases homogeneous pyramids. This is the main advantage of having a surface additive to allow better wettability of silicon surfaces. Because it allows for the desorption of  $H_2$  bubbles along with other molecules. ions hindering the reaction of  $OH^-$  ions.

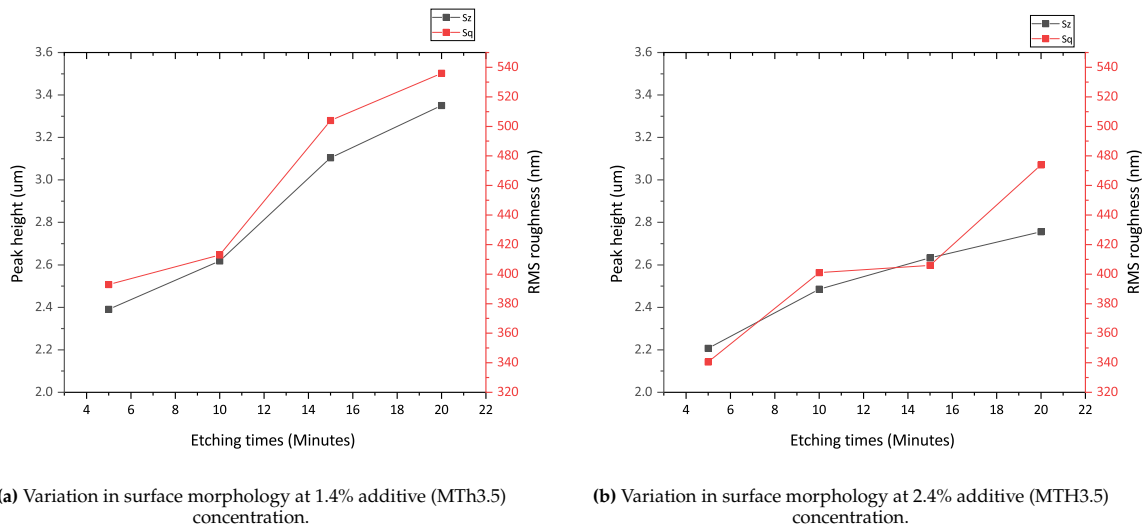


**Figure 4.21:** Variation in peak height and RMS roughness at different additive concentrations.

Further, the MT concentration was increased to 2.4% and it was found to have slightly reduced peak height at certain etch timings as shown in Figure 4.21b. Moreover, comparing the RMS roughness for both concentrations of 1.4% and 2.4% there is an almost 100 nm decrease in RMS roughness as shown in Figure 4.21. Limiting this roughness deviation to as low as possible seems to be correlated to the peak height. So reducing the peak height can further provide lesser vertical height deviations of pyramids. This slight reduction in peak height with increasing additive concentration provides information that with increasing additive, the peak height decreases to less than  $2\ \mu m$ , much better than without monoTEX. However, the constituents of the surface additive are classified making it difficult to understand the chemical reaction behind this process. Moreover, the nucleation at additive concentration of 2.4% has showcased been uniform throughout the process unlike increasing  $F$ -ratio for  $MT=2.4\%$  as shown in Figure 4.23b.

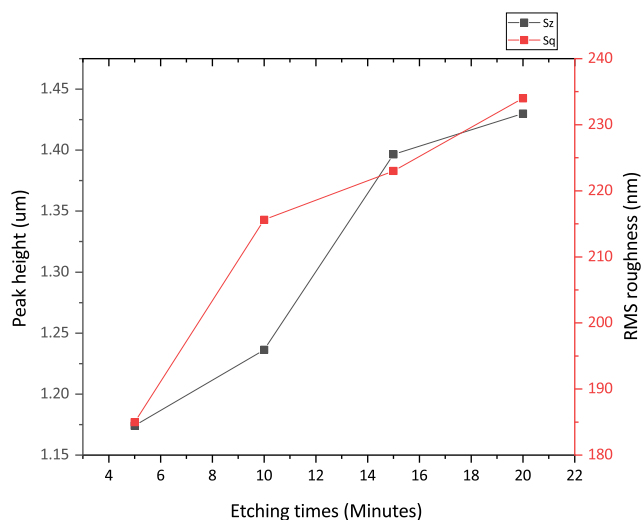


**Figure 4.22:** Variation in peak height at 5.5% additive (MTH 2.6) concentration.

Based on the evidence that increasing the monoTEX additive concentration can minimize peak height, the concentration was increased to 5.5%. However, owing to a lack of H3.5, the monoTEX additive H2.6 was utilized in subsequent experiments instead of H3.5. Surprisingly, the peak height, as shown in Figure 4.21, dropped to 1.361 and 1.407 for 10 and 15 minutes of etching, respectively, from 2.5 and 2.6  $\mu\text{m}$  for an additive concentration of 2.4%. Because of the unknown effects of the new surface additive similar to H3.5, it makes a direct correlation with previous results difficult. Therefore, to overcome this studies with a monoTEX (MT H3.5) concentration of 5.5%, as shown in Figure B.2 were performed. It revealed a peak height of 0.982 and 1.246 for 10 and 15 minutes of etching, respectively. In terms of peak height decrease, this minor difference shows that H2.6 operates similarly to H3.5.

This reduction in peak height mainly occurs because of the higher adsorption of the molecules/ions from the monoTEX additive, considering it performs similarly to Iso-Propanol Alcohol (IPA). At higher concentrations, they are well adsorbed onto the surface and prevent the fast oxidation reaction with the hydroxyl ( $\text{OH}^-$ ) group ions. [58],[79]. Moreover, it allows for the  $\text{H}_2$  bubbles formed to be desorbed from the surface at a much quicker rate and break them into smaller sizes. This has resulted in a good homogeneity of the pyramids nucleated and also reducing the size of the pyramids.

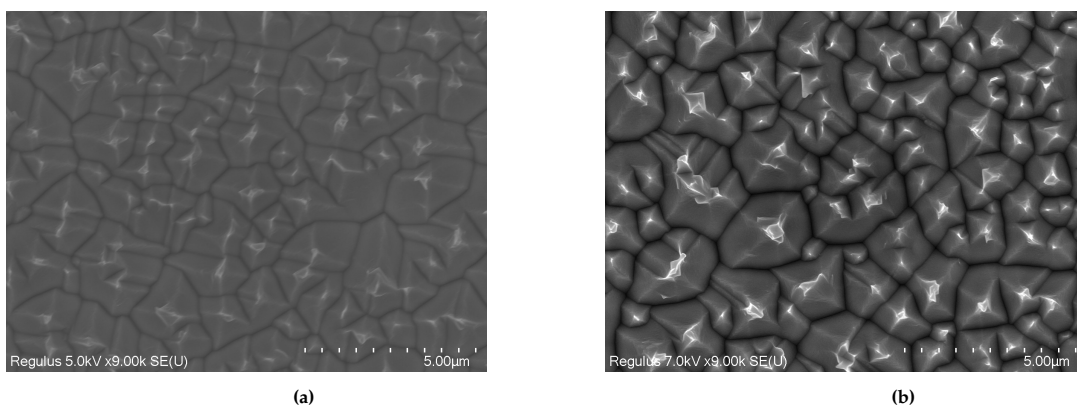


**Figure 4.23:** Surface morphology inspection at different additive concentrations of 1.4% (a) and 2.4% (b) after 10 minutes of etching.

Further, by verifying the nucleation of pyramids for MTH2.6 (5.5%) at different etching times. It was observed that at 5 minutes of etching, there are many non-uniformly spread pyramids, indicating the least homogeneity as shown in Figure 4.24b. By etching for a longer time, 20 minutes a better pyramids nucleation can be observed as shown in Figure 4.25. But, it showcases many nano-scale

features (appearing as bright spots) in the image, which increase gradually with etching time. This can also be attributed to the etching time, as it induces nano-scale features onto the pyramids.

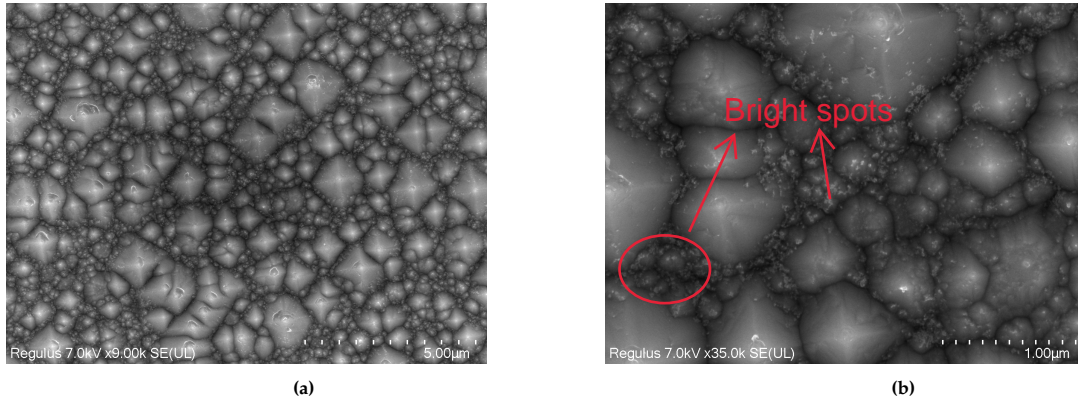


**Figure 4.24:** Surface morphology inspection for 5.5% additive concentration after 5 minutes of etching at lower magnification (a) and higher magnification (b).

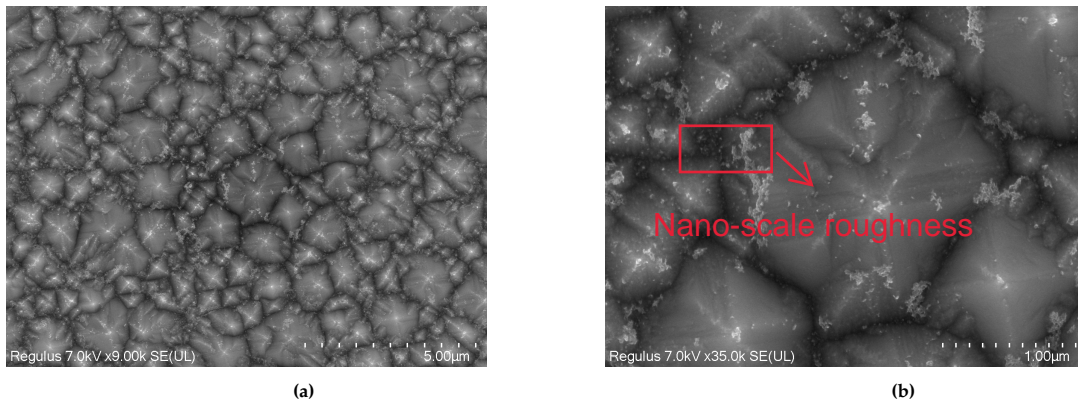


**Figure 4.25:** Surface morphology inspection at 5.5% additive concentration after 20 minutes of etching at lower magnification (a) and higher magnification (b).

While verifying the optical measurements (reflection) for different concentrations of monoTEX. It is evident that at 5 min of etching for MT 1.4% and 2.4% has a very low reflectance as shown in figure 4.26. Which gradually decreases until 15 minutes. This indicates that a more homogeneous pyramid formation is achieved at 10 and 15 minutes of etching, as the difference in weighted average reflectance is very low. Despite a slight increase in reflection observed at an additive concentration of 2.4% significant difference in pyramid homogeneity could not be found. Indicating there might be flat surfaces present for 20 minutes etched wafers, that were not noticeable in the Figure. A similar trend in decreasing reflectance as shown in Figure 4.26 is also observed at 5.5% additive concentration but with much higher reflectance due to the impact of pyramid homogeneity and size of pyramids. As mentioned in Section 2.4.2 about the AID performed for smaller pyramids [11] that showcased a higher reflection due to the decrease in mean slope. Due to time constraints, these AID measurements could not be verified. But the peak height similarity in both cases can correlate with the effects of reflection.

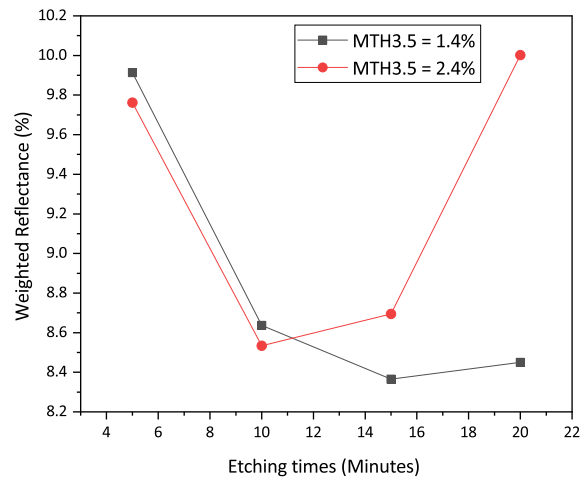


Figure 4.26: Weighted average reflectance variation for additive concentration of 1.4% and 2.4%.

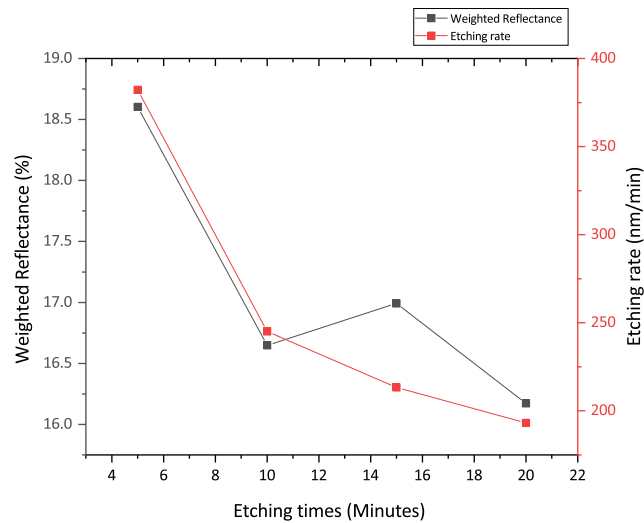
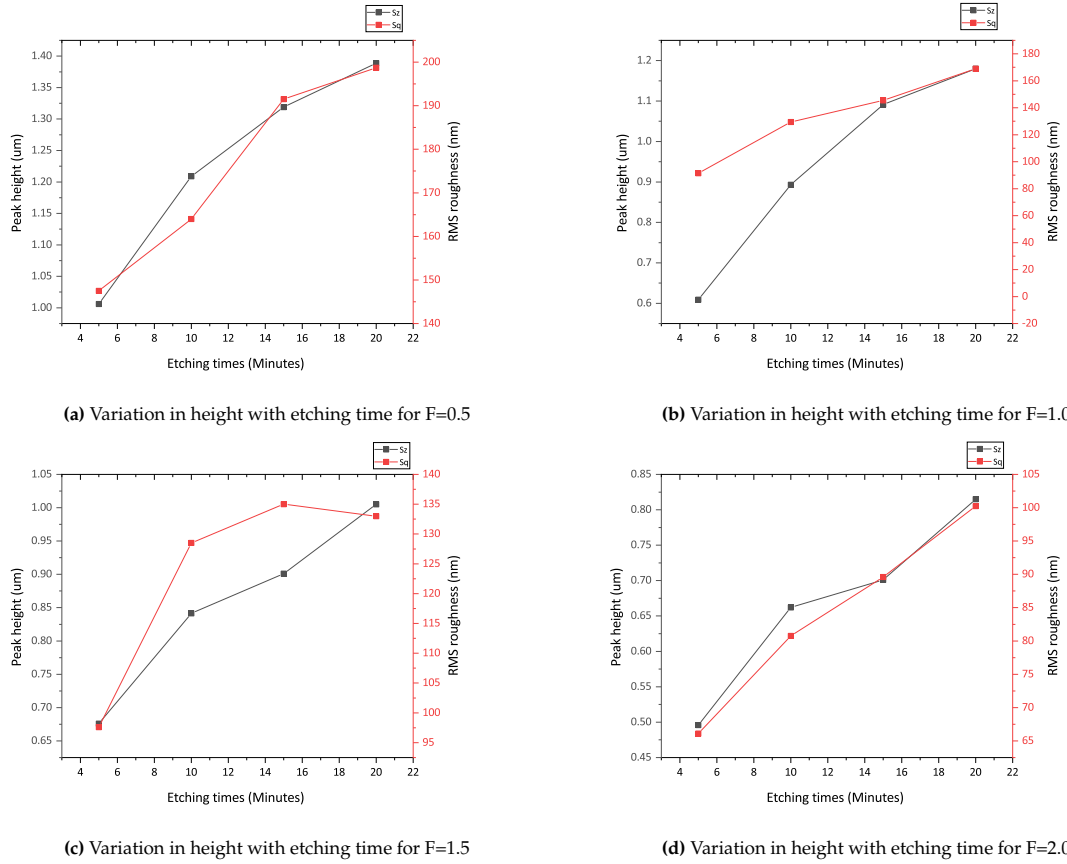


Figure 4.27: Optical and mean slope relation for 5.5% additive concentration at  $F=0$ .

#### 4.2.4. Effect of KOH+K<sub>2</sub>SiO<sub>3</sub> with surface additives

The experimental results including the application of a surface additive showed a favorable effect on peak height reduction at a concentration of 5.5%. Based on these results, it was decided to conduct a further study at the same concentration by including K<sub>2</sub>SiO<sub>3</sub>. To first determine if the chosen KOH concentration (0.7%) is the optimum a combined impact of K<sub>2</sub>SiO<sub>3</sub> and the additive was evaluated using varied KOH concentrations, as indicated in B. The results showed that KOH=0.7% obtained the least peak height. A further reduction in KOH concentration to 0.45% has produced similar results. But, such a low concentration may result in inefficient etching in the solution. It was decided to continue the experiments with a mixture of 5.5% MT and 0.7% KOH.





**Figure 4.28:** Variation in peak and height and RMS roughness at varying F-ratio and 5.5% additive concentration.

The experiment comprised of increasing the F-ratio from 0.5 to 2.0 in increments of 0.5 and was carried out at 80°C. In the case of F=0.5, as shown in Figure 4.28, the peak height was 1.006 μm after 5 minutes and steadily increased to 1.389 μm after 20 minutes. At the 20-minute etching time, the difference in peak height between F=0.5 and F=0 was only 3%. Given the relatively tiny amount of additional K<sub>2</sub>SiO<sub>3</sub>, major changes in peak height were not expected. However, when the SEM pictures for F=0.5 at 5 were examined as shown in Figure 4.29a and Figure 4.29b, a homogeneous pyramid formation was observed. This showcases an improvement in pyramid homogeneity at 5 minutes of etching for F=0.5, compared to F = 0 at the same time as shown in Figure 4.24. This improvement can be related to a decrease in the etching rate after the first 5 minutes.

Further, this pattern emphasizes K<sub>2</sub>SiO<sub>3</sub> efficient function in lowering the etching rate. However, an increasing etching time which is expected to contribute to improved pyramid homogeneity similar to F=0, was not detected with F=0.5. Since, increasing the etching time to 20 minutes as shown in Figure 4.29d many small pyramids were observed in between the larger facets. This showcases a variation in etch regime between F = 0 (MTH2.6 = 5.5%) and F=0.5 mentioned in previous section

The reflectance measurements further confirm the non-uniformity in pyramid formation as shown in shown in Figure 4.33a. This issue can be attributable to over-etching, as evidenced by the etching rate measurements. Where an excessive etching rate has led to this issue, with small or distorted pyramids being observed in Figure 4.29c.

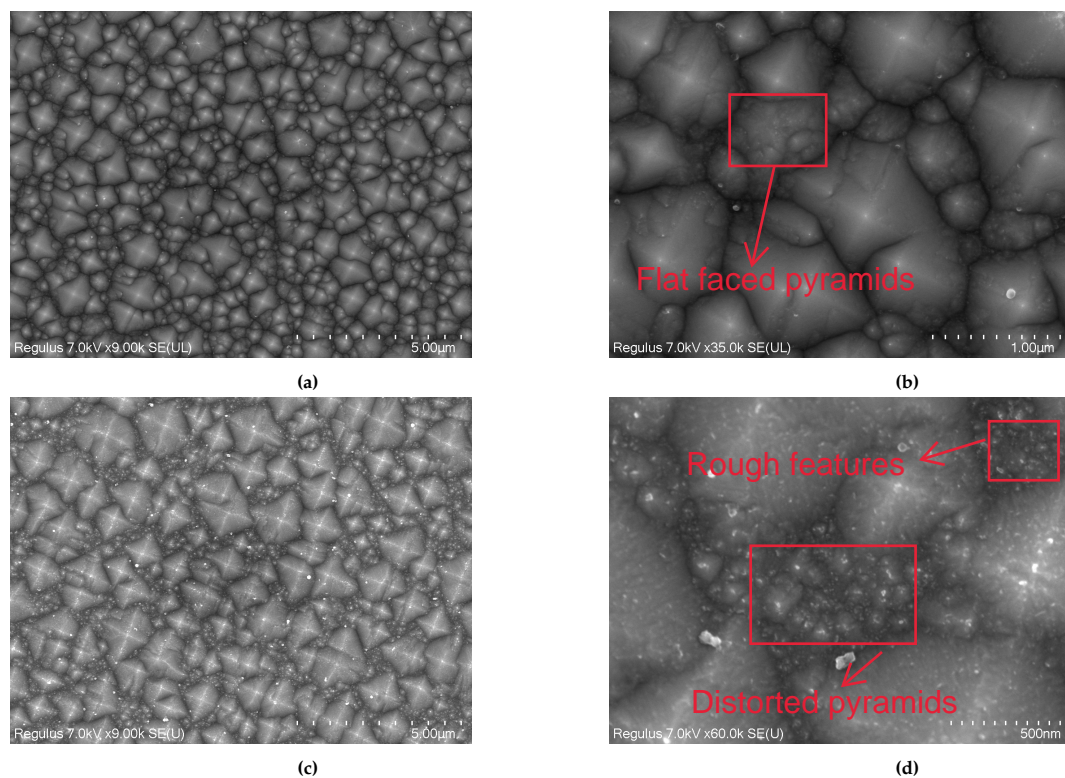


**Figure 4.29:** Surface morphology variations for  $F=0.5$ ,  $80^{\circ}\text{C}$  after 5 minutes of etching at lower magnification (a) and higher magnification (b) and 20 minutes of etching at lower magnification (c) and higher magnification (d).

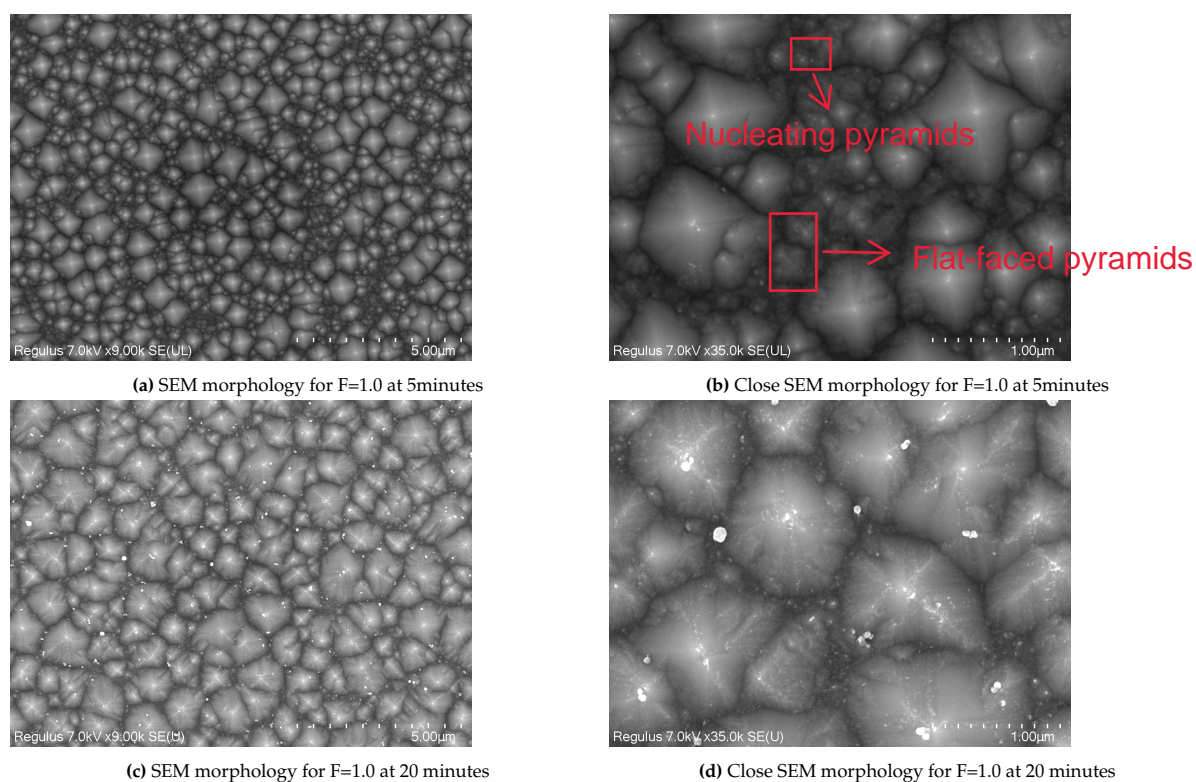


**Figure 4.30:** Surface morphology variations for  $F=1.0$ ,  $80^{\circ}\text{C}$  after 5 minutes of etching at lower magnification (a) and higher magnification (b) and 20 minutes of etching at lower magnification (c) and higher magnification (d)

However, for  $F=1.0$  as shown in Figure 4.30 similar features as  $F=0.5$  are not observed. As there are many non-pyramidal surfaces visible at 5 minutes of etching time, indicating an insufficient etch time for the surface to be well nucleated. It asserts to the previous statement in Section 4.2.2 that the  $K_2SiO_3$  reduces the etching rate due to its hindrance of  $OH^-$  ions to take part in the oxidation. Further, With etching extended for 10 minutes of etching as shown in Figure B.3, a good homogeneity of the pyramid was observed and also without any disorientations or nano-scale roughness. But, at further higher etching times over-etching causes distortions in pyramids, this was clearly visible after 20 minutes of etching time as shown in figure 4.30d. This can also be confirmed with the optical results that reflection was highest for 5 minutes and 20 minutes due to the non-pyramidal or distorted areas present in Figure 4.33d. This could also be an effect of the reduced difference in etching rate that was observed for  $F=1.0$  and  $F=0.5$  after 10 minutes of etching, 228 and 270 nm/min respectively. This difference narrows down with further increase in etching time as shown in Figure 4.33b and Figure 4.33a. But this difference was much higher at 5 minutes of etching, 240 and 332 nm/min. This indicates that the  $K_2SiO_3$  at lower  $F$ -ratios is more effective until 5 minutes, after which there might be  $OH^-$  ions available at the surface of Si that shift the kinetics back to normal.

This over-etching occurs when large pyramids (greater than  $2\ \mu m$ ) are densely spread over the (100) Si substrate orientation. Due to this, the Si substrate orientation disappears and we observe (111) pyramid facets. As mentioned in Section 3.4 the etching rate for (111) oriented pyramids is much lower than (100). For, such pyramids with higher peak height it is difficult to observe over-etching for the 20 minutes of etching time considered [61]. But, for the increased monoTEX concentration, the peak height is relatively lower and it is much easier for the solution to attack the [100] surface. Therefore, it takes much lesser time for the pyramids to be dis-oriented, and the reason for observing pyramid-free areas and distorted pyramid facets.

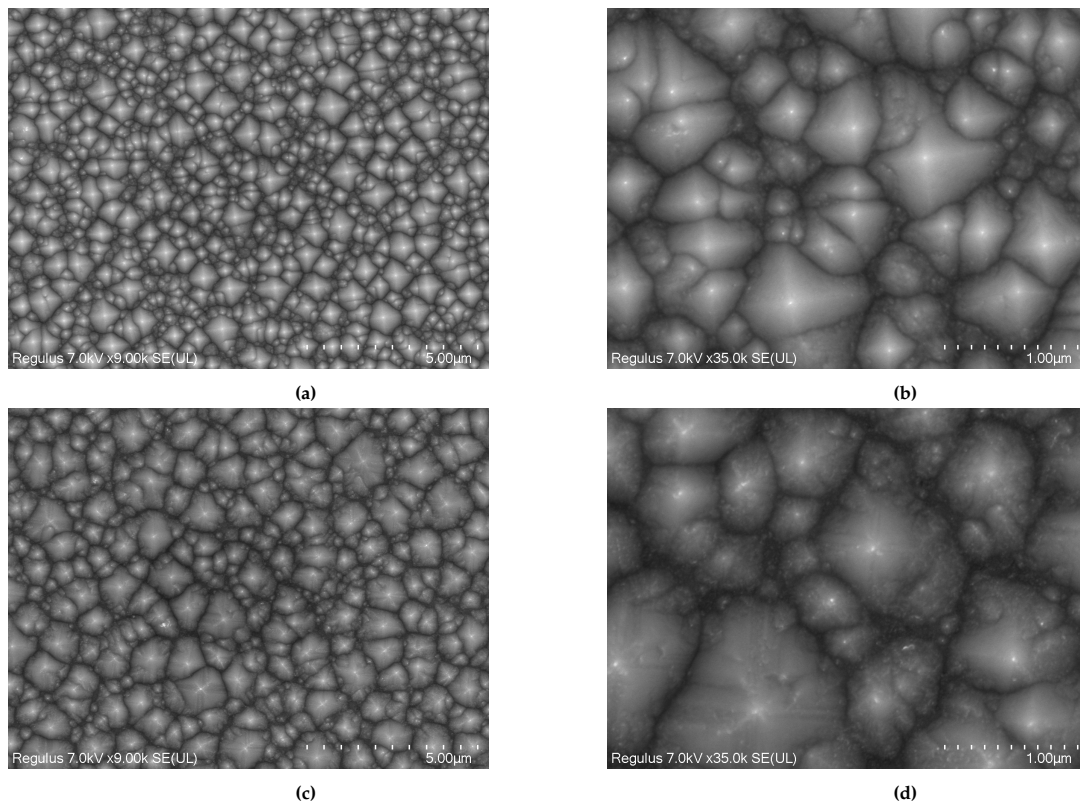


**Figure 4.31:** Surface morphology variations for  $F=1.5$ ,  $80^\circ C$  after 5 minutes of etching at lower magnification (a) and higher magnification (b) and 20 minutes of etching at lower magnification (c) and higher magnification (d).

Further, at  $F=1.5$  the peak height as shown in Figure 4.28c reduced to less than a micrometer at 15 minutes and 20 minutes of etching, indicating a desired height reduction to less than  $1\ \mu m$ . However, this reduction comes at a trade-off with reduced pyramid homogeneity. As observed from both the SEM and reflectance variation in Figure 4.31 and Figure 4.33c respectively. It is observable that for 5



minutes there are few distorted or flat-faced pyramids present in between the valleys, which indicates an under-etching present. But in comparison to the 5 minutes etched wafer at  $F=1.0$  as shown in Figure 4.30b, there is slightly less pyramid distortion observed at  $F=1.5$ . This could be occurring due to an error in the time the wafer was etched (6-7 minutes), resulting in a better pyramid density. Moreover, the peak height difference between  $F=1.0$  and  $F=1.5$  is almost similar as shown in Figure 4.28b and Figure 4.28c. Nevertheless, the effect of a slower etching rate until 10 minutes of etching is shown in Figure B.4 for  $F=1.5$ . Which showcased lesser pyramid distortions and pyramid-free surfaces until 10 minutes of etching. But, a further increase in etching time led to over-etching being observed again as shown in Figure 4.31d at 20 minutes of etching.

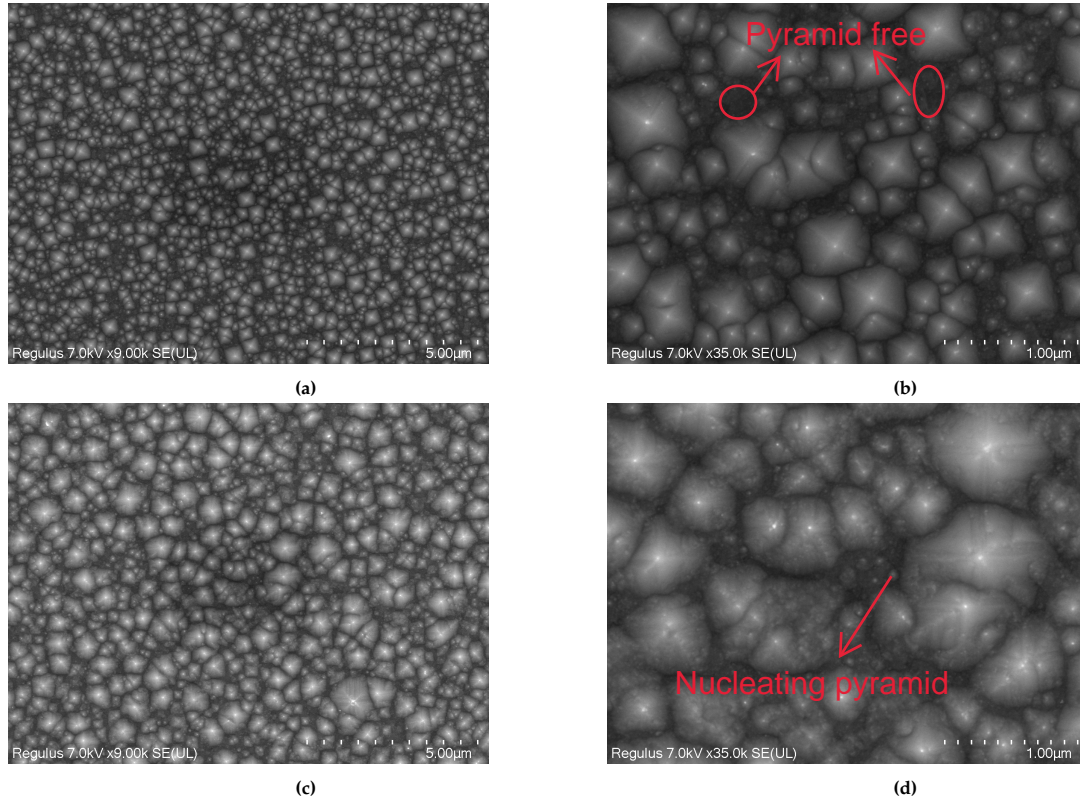


**Figure 4.32:** Surface morphology variations for  $F=2.0$ ,  $80^{\circ}\text{C}$  after 5 minutes of etching at lower magnification (a) and higher magnification (b) and 20 minutes of etching at lower magnification (c) and higher magnification (d).

However, with increasing the F-ratio to  $F=2.0$  a slower etching rate is observed. This has reduced the peak height to less than  $0.5\text{ }\mu\text{m}$  at 5 minutes of etching as shown in figure 4.28d. Unlike the previous cases of F-ratio from 0.5 to 1.5 many flat-faced pyramids are present initially at 5 minutes of etching. At  $F=2.0$  there are many pyramid-free areas observed as shown in Figure 4.32b. This indicates bad nucleation, which is assumed to be occurring because of reduced  $\text{OH}^-$  ions required for the etching. But, despite the increase in etching time a good nucleation affect was not observed from figure 4.32 and reflectance measurements as shown in Figure 4.33d has also increased. Since the additive concentration is maintained at 5.5% compared to others, its desorption rate of  $\text{H}_2$  bubbles on the Si surface remains the same. Therefore, it could be interpreted that the reduced  $\text{OH}^-$  ions are not able to react with the Si surface. Because more ions/molecules are hindering their reaction, which might have been lesser (at lower F-ratios) allowing for good pyramid nucleation. This might create an imbalance between the desorption of the products (slower) and oxidation of reactants, as such an issue might cause irregularities on the surface [86].

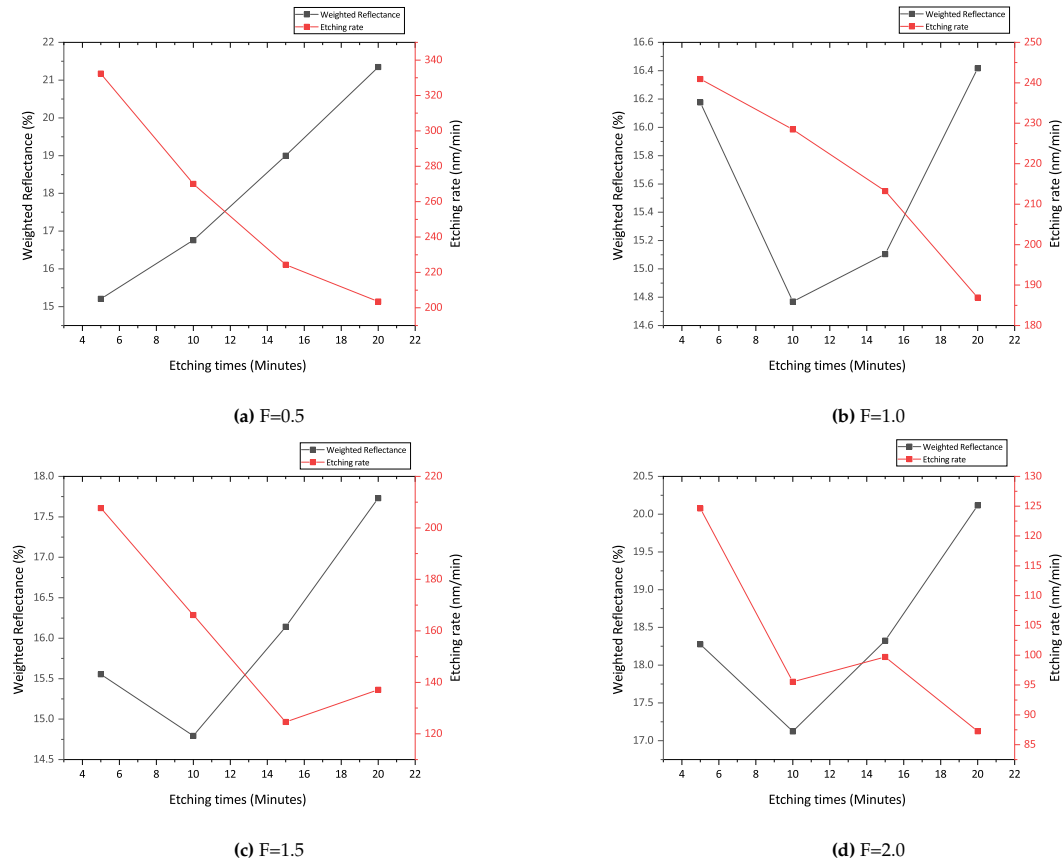


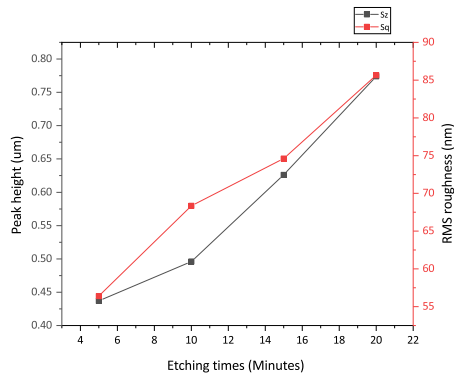
Figure 4.33: Weighted average reflectance and etching rate variations at different F-ratios

#### 4.2.5. Effect of temperature

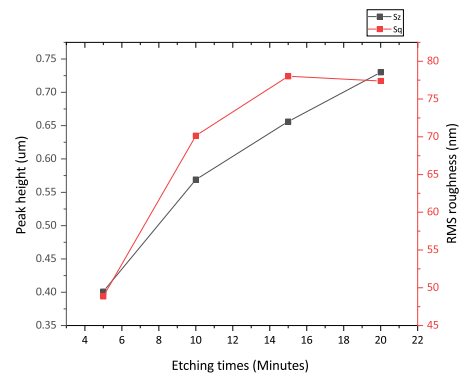
It is important to note that for  $F=0$  at  $80^\circ\text{C}$  as shown in SEM images Figure 4.24 and Figure 4.25 for 5 and 20 minutes of etching respectively. Many nano-pores or very small pyramids were observed (bright spots). This roughness has been observed to have gradually reduced at  $F=1.0$  as shown in the previous Section 4.2.4. It is the etching rate which has mainly differed between  $F=0$  to  $F=1.0$  at  $80^\circ\text{C}$ . So it could be understood that a lower etching rate is resolving this issue.

Further, a reduction in temperature can provide similar results, due to lower etching rate [58]. It was decided to understand the effect of temperature which was evaluated for  $F=0$ . Because of the solubility issues with  $\text{K}_2\text{SiO}_3$ , the experiments performed earlier were conducted at  $80^\circ\text{C}$ . However, increasing the temperature to above  $80^\circ\text{C}$  and allowing for the  $\text{K}_2\text{SiO}_3$  to dissolve well enough in the solution, could allow us to continue the experiments at lower temperatures.

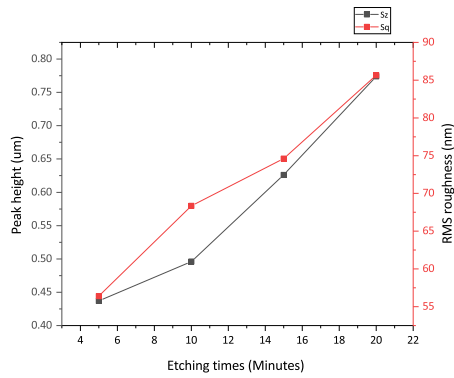
First, the experiments were performed at  $F=0$  at  $75^\circ\text{C}$  and later at  $70^\circ\text{C}$ , while maintaining rest of the parameters the same (solution concentration of KOH and  $\text{MTH}_2.6$ ). It is interesting to note that by reducing the temperature to  $75^\circ\text{C}$ , a slight reduction in peak height was observed as shown in Figure 4.34a. This difference in peak height reduction for  $F=0$  at  $70^\circ\text{C}$  as shown in Figure 4.34b in comparison to  $80^\circ\text{C}$  is around 16.35% at 10 minutes of etching. While at  $75^\circ\text{C}$  a noticeable change was not observed, but a decrease in surface roughness was noted. This reduction in peak height and RMS roughness can be related to the slow nucleation kinetics of Si reaction with the water molecules, which is also confirmed by the etching rate variation as shown in Figure 4.38a and 4.38b



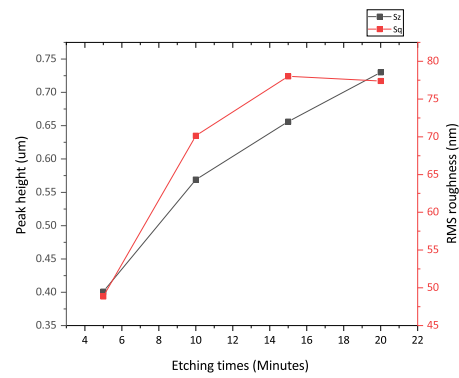
(a) Variation in height with etching time for F=0 at 75°C



(b) Variation in height with etching time for F=0 at 70°C



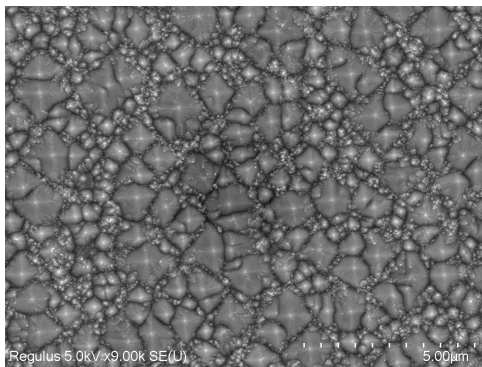
(c) Variation in height with etching time for F=2.0 at 75°C



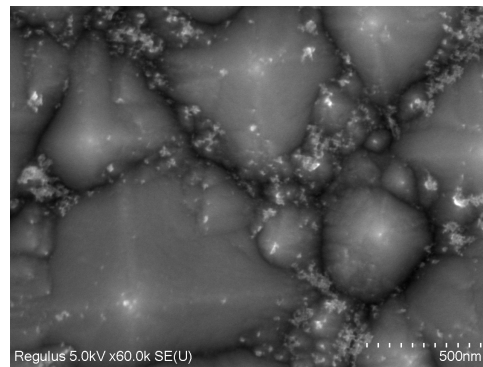
(d) Variation in height with etching time for F=2.0 at 70°C

**Figure 4.34:** Variation in peak and height and RMS roughness at 70°C and 75°C temperatures

Previous investigations at 80°C with F=0 revealed the presence of small areas or nanoscale roughness in the SEM illustrations. Similar results were obtained from studies employing F=0 at 75°C, as shown in Figure 4.35. Despite the effect being slightly lessened at the lower temperature, it is clear that distortions still exist in these circumstances. These deformities may be caused by the ineffective removal of certain masking elements ( $H_2$ ,  $Si(OH)_4$ , etc.)



(a) SEM morphology for F=0 at 10 minutes



(b) Close SEM morphology for F=0 at 10 minutes

**Figure 4.35:** Surface morphology variations for F=0 at 75°C

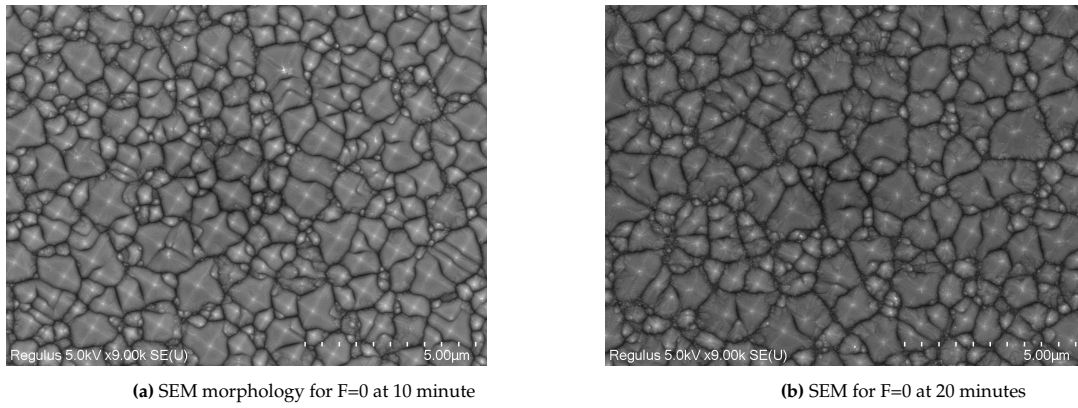


**Figure 4.36:** Surface morphology variations for F=0 at 70°C

During the anisotropic etching process,  $H_2$  bubbles serve as masks for etching into the Si [82]. These bubbles are eventually reduced to a smaller size by the surface additive, allowing for the formation of sub-micrometre textures observed with good pyramid nucleation. But, to achieve this quick removal rate, the process requires a higher amount of surface additive to be used. This is also the reason a surface additive concentration of 5.5% or higher is required. Moreover,  $H_2$  is not the only byproduct present in the solution it also contains other ions/molecules ( $K^+$ ,  $Si(OH_4)$ ). It could be possible that these ions are not being removed effectively and are contributing to the observed roughness by acting as a mask.

This slowdown in the removal of respective ions/molecules is related to the desorption process that was previously mentioned in section 3.4. This slower desorption rate impacts the oxidation process resulting in reduced  $OH^-$  ions participating in the oxidation process. Moreover, at F=0 the solution is working more effectively and has more  $OH^-$  ions available for oxidation. But, the slow desorption process is affecting the oxidation process to continue, creating an imbalance. This results in the observed nano pore roughness [58].

At a temperature reduction of 70°C after 5 minutes of etching, this effect of nano-scale roughness is reduced as shown in figure 4.36. Along with the peak height reduction as shown in Figure 4.34b. Indicating the temperature decrease allows enough time for the additive to remove the  $H_2$  bubbles from the Si surface, which carries away other byproducts with it. Therefore, maintaining an equilibrium rate with oxidation and desorption. Further, the effectiveness of good nucleation can be verified with the lower reflectance as shown in Figure 4.38b. But the over-etching continues after 10 minutes, which indicates an etching period beyond 20 minutes is required to have a good pyramid homogeneity again.

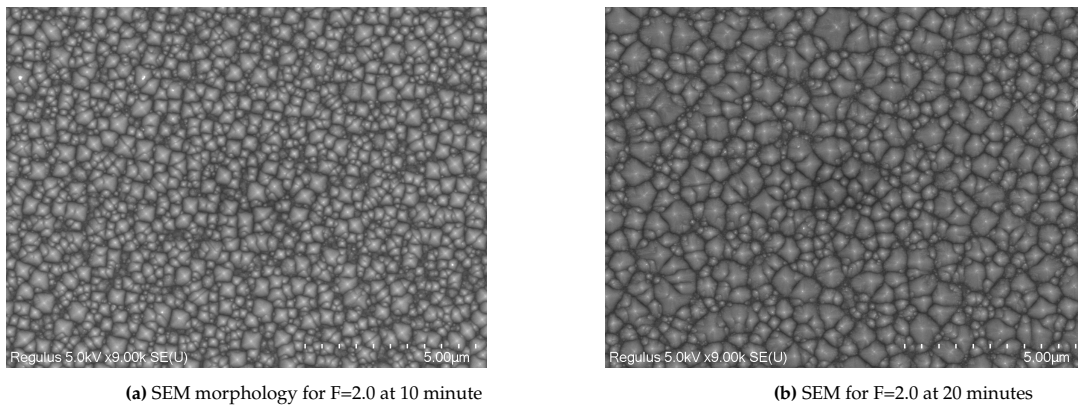


**Figure 4.37:** Surface morphology variations for F=2.0 at 70°C

Moreover, the issue of nano-pore roughness was resolved due to maintaining a balance between oxidation and desorption of products. It could also be possible that this reaction rate imbalance is also causing the observed ineffective etching at F=2.0 at 80°C. So temperature variations were also analyzed for F=2.0.

Interestingly the peak height at  $F=2.0$  for  $75^{\circ}\text{C}$  and  $70^{\circ}\text{C}$  as shown in Figure 4.34d and 4.34c. These values are almost similar to the peak height noted for  $F=2.0$  at  $80^{\circ}\text{C}$  as shown in Figure 4.28d. Comparing the pyramid homogeneity, for  $F=2.0$  at  $80^{\circ}\text{C}$ , many non-uniformities on the surface could be noticed, like pyramid-free areas and over-etched regions. But at  $70^{\circ}\text{C}$ , no such non-uniformities are predominantly observed as shown in Figure 4.37. This can be asserted with the previous explanation of the presence of unknown ions hindering the  $\text{OH}^-$  ions from reacting with Si. Further, the reduction in temperature has allowed for the removal of these unknown ions, restoring the surface with a good amount of nucleation resulting in a reduced reflection as shown in Figure 4.38d. So, it is clear that in order to achieve good pyramid homogeneity, a lower temperature is more beneficial at a slower etching rate.

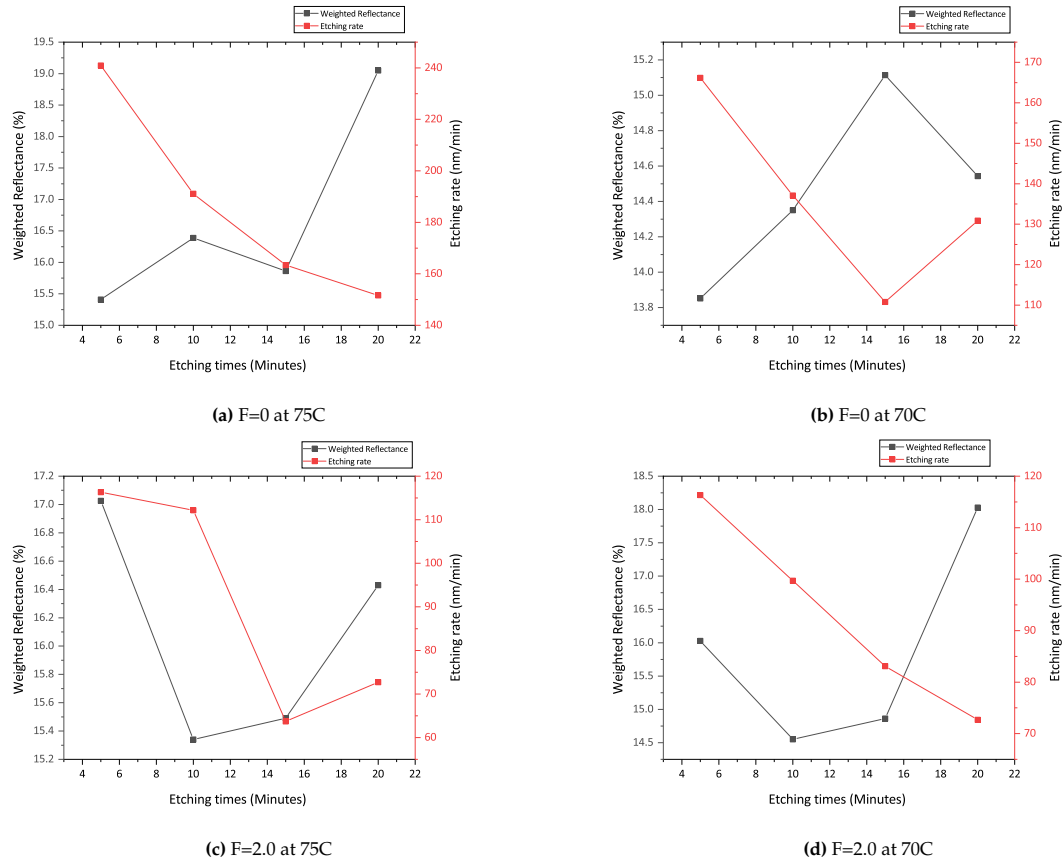


**Figure 4.38:** Weighted average and etching rate variations at different F-ratios and temperature

# Lithography technique to vary the surface morphology

## 5.1. Introduction

Lithography is a widely used technique in semiconductor industry and as explained in section 3 about the difference in general lithography techniques. The objective of using this technique for this thesis lies in creating 2D periodic features that can provide angle-selective light trapping. It is feasible to create such features using lithography equipment, and already experiments have been performed in creating such features.

As mentioned in Section 3.2 and 3.3, the reason behind experimenting with lithography techniques to implement sub-micron surface features. Similar technique is also evaluated in creating periodic nano scale features on the bottom cell of a state-of-the-art perovskite/SHJ tandem device fabricated by HZB [10]. This device yielded an efficiency of 29.5% by incorporating nano-imprinting lithography to create sub-micron features on the bottom cell. This involved preparing a master mold using interference lithography. Later, transferring the pattern from master onto a PDMS stamp, which used a soft-mold to replicate the pattern during the UV-NIL step. Finally, a reactive ion etching step was performed to anisotropically etch into the Si substrate. They were able to demonstrate that the  $J_{sc}$  increased from 39.15 to 39.47 mA/cm<sup>2</sup> for the nano-structured feature and less non-radiative recombination losses.

Similar process flow of replicating the patterns as shown in Figure 5.1 was also demonstrated by Sutter J. [87]. This procedure involved features with depth less than 400 nm implemented onto SHJ solar cell, is also compatible for a tandem device. They demonstrated an improved efficiency from 17.9% for planar structures to 21.9% for pyramidal features. Most importantly, they were able to showcase that the light reflectance in comparison to industrial textured pyramids, has greatly reduced for their pyramidal features above a wavelength range of 750 nm, showcasing its potential to use in monolithic tandem devices.

Hence it was put forward to develop a process flow to allow fabrication of such nanometre scale-features onto SHJ devices. By optimizing the nano-imprinting lithography process steps, which

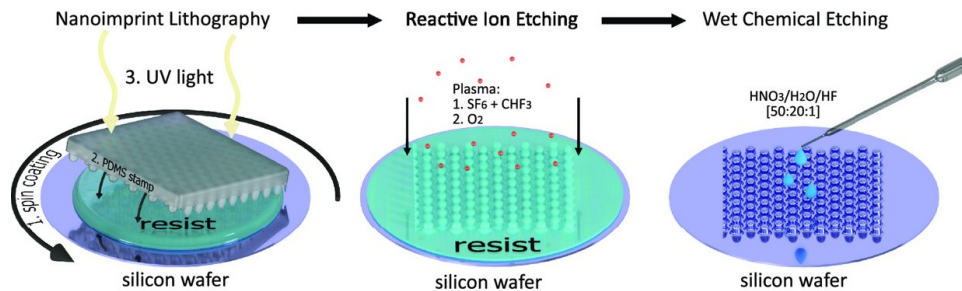


Figure 5.1: Process flow description for replication of nanometer scale features. Adapted from [87]



will be detailed in the next part.

### 5.1.1. Nano-imprinting lithography

This technique consists of two methods for replicating the patterns, namely T-NIL (Thermal nano-imprint lithography) and UV-NIL (Ultra violet nano imprint lithography). These two methods mostly involve the same processing steps of using soft molds to replicate the pattern, but they differ in the usage of resist for transferring those patterns [88]. As T-NIL technique is carried out at elevated temperatures, it requires a thermoplastic resist. Whereas UV-NIL requires a resist that is curable under UV light at room temperature conditions, this technique was considered in the previously mentioned literature of Sutter J.[87].

The main parameters to be considered for the T-NIL process is the selection of resist as they need to be deformable under an applied pressure and higher temperature. For this to occur, the elastic modulus of resist should be lower than the NIL mold during pressing [89]. To allow for this reduction in the elasticity of resist, it's temperature needs to be elevated above their glass transition temperature ( $T_g$ ). Later, the template is pressed at a certain pressure to allow the resist to flow into the cavities of the mold. Finally the template is separated after the patterned resist cools down to below its glass transition temperature.

Though, UV-NIL process has proven to have a lower lead time for pattern replication than T-NIL. It was decided to perform a T-NIL process due to the lack of equipment available at TU delft to perform an UV-NIL process. However, selecting the imprinting step is not the sole step, it requires manufacturing a master mold, a soft mold to be used in NIL process for pattern replication on the resist and subsequent pattern transfer into Si substrate.

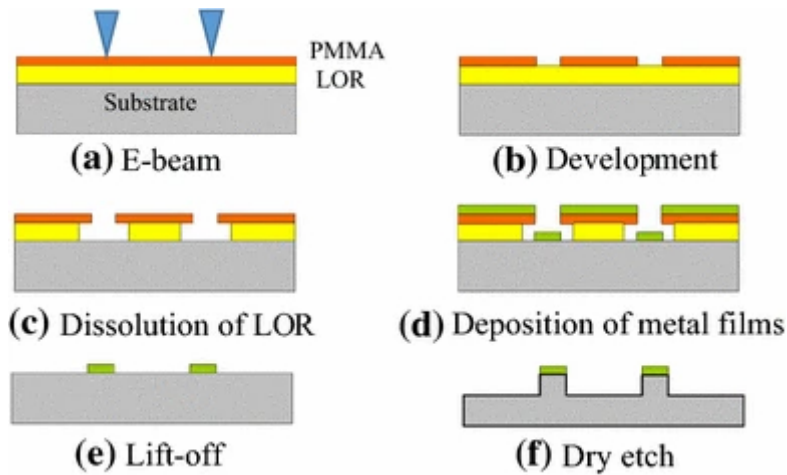


**Figure 5.2:** Schematic representation of a Lift-process used to fabricate master mold for nano imprinting. Adapted from [88]

A general process flow for nanofabrication of features through T-NIL with lift-off technique is as shown in figure (5.2). Here, the first step involves deposition of a hard mask which allows etching into the Si without worrying about the consumption of resist. Later, a subsequent resist like PMMA suitable for e-beam lithography is deposited by spin-coating. After exposure at the required dosage parameters, the resist is developed, which provides an opening to the underlying hard mask. In order to open the hard mask a Reactive-Ion-Etching (RIE) or wet etching is done, opening the Si layer. To process with the subsequent lift-off process, a suitable metal layer is sputtered on the substrate. This way the underlying hard mask can now be removed, allowing the metal to stay at rest of the places. Finally, with a dry etching technique, the Si is etched by masking the areas covered with metal. This process flow is mostly referred as a metal lift-off technique and is widely used for better control over the pattern dimensions and materials which are difficult to etch due to selectivity issues.

However, following this process is inconvenient for master mold fabrication, as it involves additional steps like sputtering and metal lift off that consumes more amount of time. Therefore, it is necessary to avoid these additional steps and investigate ways to transfer patterns in much simpler processing steps. Research was carried out by Razzaq [90] in replicating nano scale feature without lift-off procedure, to implement light trapping structures on SHJ bottom cell using the T-NIL method. This process involves

the following steps as shown in Figure using <CZ> n-type wafers with SiO<sub>2</sub> hard mask deposited by PECVD technique on both sides of the wafer. It is usually deposited on both the sides to prevent metal contamination in subsequent processing. Followed by spin-coating of photo-resist, which is used for pattern transfer from a soft mold. Though the soft mold preparation is not detailed, it is prepared from a silicon elastomer (Sylgard 184 dow). Later, a thermal imprinting step is performed by a hydraulic press at 130C. The transferred pattern onto the resist provides an opening for SiO<sub>2</sub> to be etched anisotropically by RIE etching process. Finally, the provided hard mask openings with 800 nm of pitch gratings allow for creating inverted nano pyramids through TMAH wet-chemical etching. The results indicate that inverted nano pyramid features fabricated have showcased a J<sub>sc</sub> of 38.1 mA/cm<sup>2</sup> compared to a random pyramid textured device which exhibited 39.3 mA/cm<sup>2</sup>. Based on the reflection results it could be understood that more photons are being reflected in the wavelength range of 400-800 nm causing a reduction in short-current. This occurs, primarily, due to the diffraction of light at selective angles observed due to pyramid gratings. Where the light path enhancement at 800nm led to NIR photons to be deflected at greater angles. Such an enhancement in NIR wavelength range is highly favourable for monolithic tandem devices.

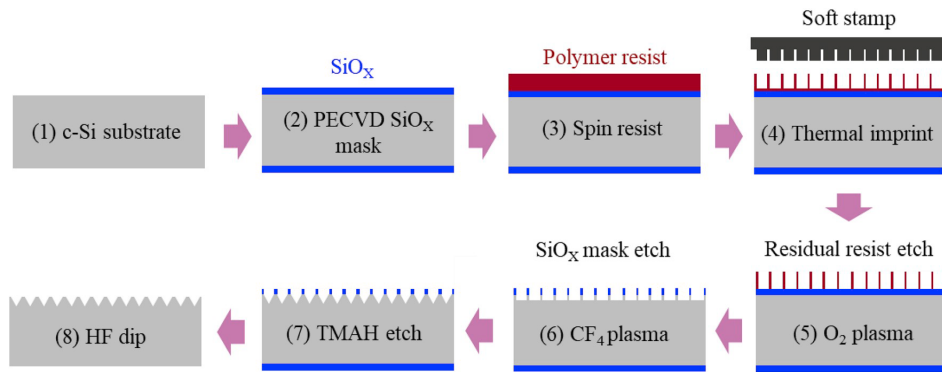


Figure 5.3: Process for fabrication of inverted nano pyramids using T-NIL technique. Adapted from [90]

Based on these research finding a process flow has been devised to experiment for the replication of nano-scale features that would allow for the creation of Inverted nano pyramids as shown in Figure 5.4.

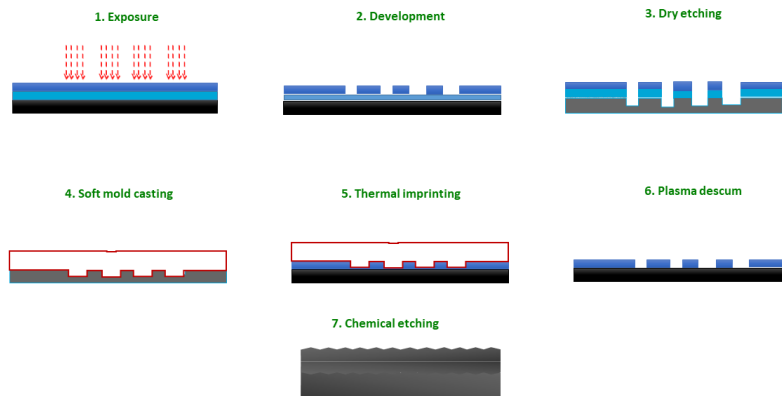


Figure 5.4: Schematic of process flow devised for fabricating Inverted nano-pyramids

## 5.2. Master mold fabrication

First, to create a master mold with 2D periodic features, a FZ-Si wafer was used which has a thickness of 280 ± 20 μm. Later it involves depositing a SiO<sub>2</sub> layer of 200nm by PECVD. Since the etch selectivity of



Si and most e-beam resists is too low. It was decided to deposit a hard mask layer like  $\text{SiO}_2$ , preventing the consumption of mask before the Si layer is etched.

The next step involves choosing a suitable electron beam (e-beam) resist. Three positive e-beam resists were chosen for this approach which include, PMMA, CSAR-62 and ZEP 520-A. Further, it is required to determine the suitable resist based on their resistance to different gas recipes that would be used to etch  $\text{SiO}_2$  and Si. Evaluating different recipes that were used by several personnel in Kavli Institute of Nanoscience, TU Delft, the respective etch rates for each of the resists as shown in table 5.1 were obtained.

**Table 5.1:** Etch rate (nm.min) of resist materials at different gas mixtures in dry-etching

	O <sub>2</sub>	SF <sub>6</sub> & O <sub>2</sub>	CHF <sub>3</sub> & O <sub>2</sub> (DC Bias-50W)	CHF <sub>3</sub> & O <sub>2</sub> (DC Bias-100W)
CSAR 62	66	93	29	54
PMMA	104	133	44	71
ZEP 520A	64	86	27.5	48

Based on this data CSAR-62 has showcased a better resistance to etching, and it was decided to use this as suitable positive resist for mask opening.

To deposit this resist, using a manual spin coater with a speed of 2000 rpm for 2 minutes allows 550 nm of ARP.6200.13 (CSAR-62) resist being deposited onto the master substrate. Later it is transferred onto a hot-plate and pre-bake it for 3 minutes at 150 °C. To verify the thickness of the resist deposited a dektak profilometer was used with a tip radius of 0.8 µm. The measurements showcased a resist thickness of 430± 25 nm of resist thickness.

The next step involves optimizing the right exposure dosage for the resist deposited. Initially, a dosage test was performed on the EBPG writing tool from 180 - 330 µC/cm<sup>2</sup>, with a frequency of – and applied proximity effect correction. After exposure the samples were developed in a solution of pentyl acetate for 1 minute and 5s in xylene. This xylene rinse is a very crucial step as it allows to develop the resist without many resist residuals. Finally, it was rinsed in iso-propanol alcohol (IPA) for 1 minute before inspecting them under SEM, which yielded the following results as shown in Figure 5.5. For dosage test performed up to 260 µC/cm<sup>2</sup>, we were able to see residues of resist being gradually decreasing. For the dosage applied below 240 µC/cm<sup>2</sup>, there were excessive residues due to the inability of electrons to reach the dedicated area uniformly. However, when a higher dosage is applied than required, it could lead to a variation in wall width and sensitivity of resist. Hence, a dosage lying between 260 and 280 seemed to provide optimum results without any resist residuals.

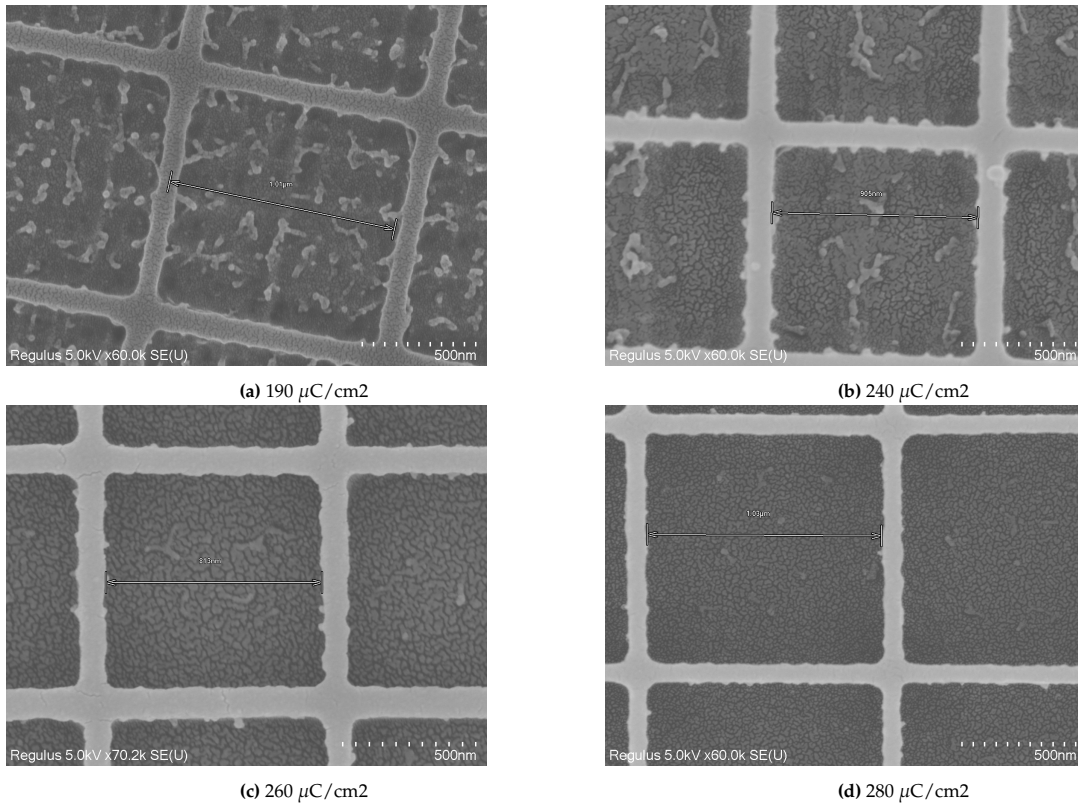


**Figure 5.5:** 2D periodic gratings dosage test

It should also be noted that for these dosage tests proximity effect correction [91], which provides a varied dosage in the exposed area by simulating the forward and scattered electrons as mentioned in 3.2 was considered. This makes the writing task slightly time-consuming. However, the frequency at this dosage, calculated based on the equation described in 3.1, is very low. This also means that a higher writing time would be required. Since time and frequency are inversely proportional. Such a low frequency also limits the system's computational power to perform PEC for large pattern exposure. Considering these, a change in frequency was considered as recommended by the system for a PEC. But still, the exposure time with a PEC for  $160 \times 40 \text{ mm}^2$  sample is higher than 16 hours. Therefore, a dosage test was performed again from 185 - 220  $\mu\text{C}/\text{cm}^2$  without any PEC. Finally, an optimum arrived at 220 Do with a base frequency of 71MHz with lesser residuals obtained as shown in Figure (5.6).

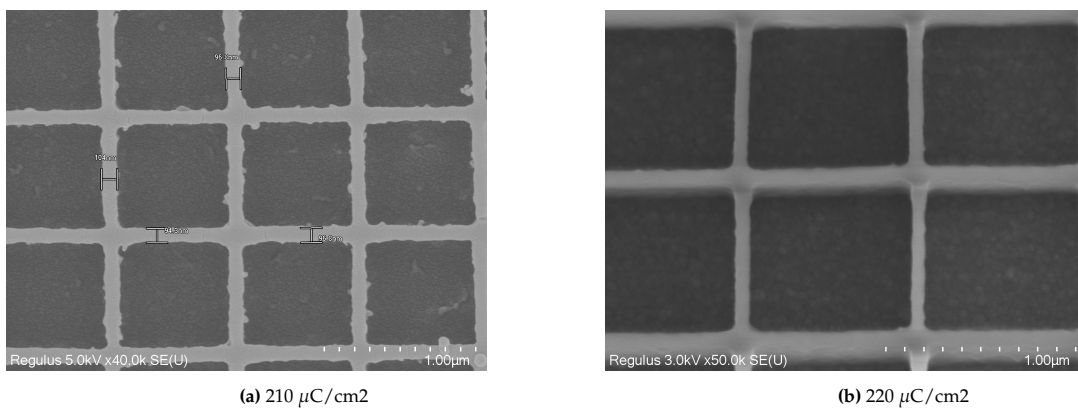


**Figure 5.6:** 2D periodic gratings dosage test without any PEC

### 5.2.1. Dry etching

Apart from the mentioned alkaline texturing process (wet etching), dry etching is also an important process that is used in the semiconductor industry to etch layers. This anisotropic texturing is interesting as it tends to solve some of the problems in wet etching. Some of these are related to sub-micrometer feature transfer through the mask or resist layers. Where temperature and solution concentration affect the size of such features [92]. This is due to the surface tension exhibited by the liquids that cause the creation of adjacent features that prevent further etching in the area. Also making it difficult to control the size of features formed. So, with the dry texturing process, we can obtain better nano and micro detailing of features. Hence, this method is chosen over wet etching process to fabricate the master mold.

After optimizing the dosage of resist layer without any resist residuals, it is necessary to open the hard mask for subsequent etching into Si. However, to etch anisotropically into SiO<sub>2</sub> the process parameters of RIE need to be optimized.

Gas characteristics	SiO <sub>2</sub> removal	Si removal	Plasma descum
O <sub>2</sub> (sccm)	-	20	20
C <sub>4</sub> F <sub>8</sub> (sccm)	17/15	-	-
CH <sub>4</sub> (sccm)	17/15	-	-
He (sccm)	150	-	-
SF <sub>6</sub> (sccm)	-	100	-
RF Source power (W)	2800/2500	1000	2500
RF DC Bias (W)	250	10	50
Temperature (C)	0	-120	0
Pressure (bar)	1e-5	1e-5	4e-5
Etch rate	1.2 um/min	0.85 um/min	-

**Table 5.2:** Parameters used for RIE etching of SiO<sub>2</sub>, Si and resist

As mentioned earlier in Section 3.1 that there are different radicals which are used to etch selective materials. For SiO<sub>2</sub> CHF<sub>3</sub>/CH<sub>4</sub>/He gases are found to provide a good etch selectivity for SiO<sub>2</sub> over resist and Si [93]. The process parameters used for the dry etching are as described in table 5.2. Most importantly, the previously mentioned cryogenic process in section 3.1.1 was not used. Due to the lack of gas mixture available for processing. Hence, ICP-RIE AMS 110 (Adixen) at Else Kooo Laboratory (EKL), TU delft was used. The process parameters used for the dry etching at a source power of 2800 W as described in table 5.2. With these parameters set, the SiO<sub>2</sub> was etched without consuming the resist. However, on inspection of the samples without any resist stripping as shown in figure 5.7a. The sample showcased distorted walls, indicating excessive undercut of the underlying SiO<sub>2</sub> layer. Which is called the bowing effect.

The reason behind this bowing effect could be mainly related to the mask faceting, where the resist mask is tapered at a certain angle. Though the e-beam resist mask after developing did not exhibit any facet angle as shown in Figure 5.6b. It could still be possible to exhibit this issue due to ion bombardment [94]. This effect could be reduced by having a lower ion-bombardment. Since the accelerating voltage of ions is controlled by DC bias power. A high bias power could lead to a strong ion bombardment, causing excessive damage to the sidewall. To investigate different DC bias power was experimented.

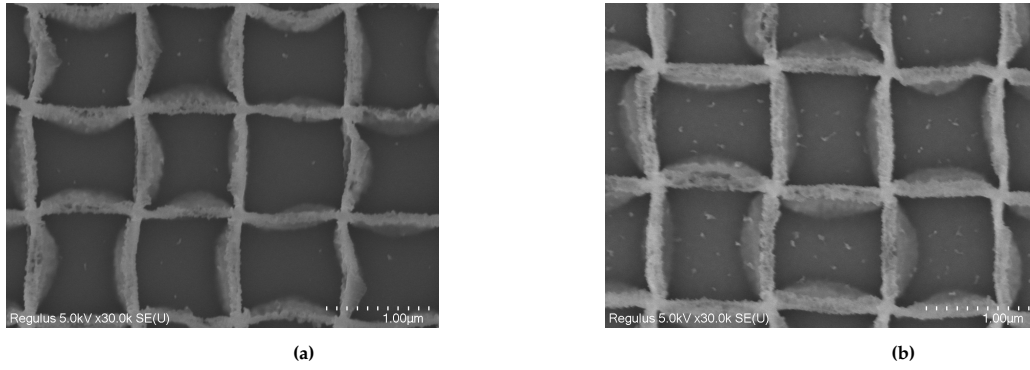


**Figure 5.7:** Stress-induced deformation of resist sidewalls at 250W DC bias (a) and 150W DC bias (b).

So, a test was performed with similar parameters as defined earlier. By performing an experiment with a reduced DC bias power to 150 W. Also, the time for etching is kept constant at 30s to observe the effect of the etching rate. As shown in figure 5.7b the sidewall damage is still present without much significant improvement visible. Moreover, the stress on the resist sidewalls still remains, resulting in deformation. With further reduction in DC bias power to 75W, slightly reduced sidewall damage or bowing effect is visible as shown in figure 5.8a. Compared to earlier experiments with higher DC bias, this experiment had lesser sidewall curvature. However, with reduced power comes a reduced etch rate, so based on AFM measurements after the resist removal the etch rate of  $\text{SiO}_2$  was determined. It was found that for the 30s, 30 nm of  $\text{SiO}_2$  is being removed. Therefore, to remove 200 nm of oxide an etching time of 2 minutes was considered to check the removal of the oxide layer. But, after this subsequent timing, the resist deformation reappeared as shown in Figure 5.8b. Further, reducing the DC power bias has induced polymer deposition, as the power required to accelerate these ions is insufficient to create an etching.

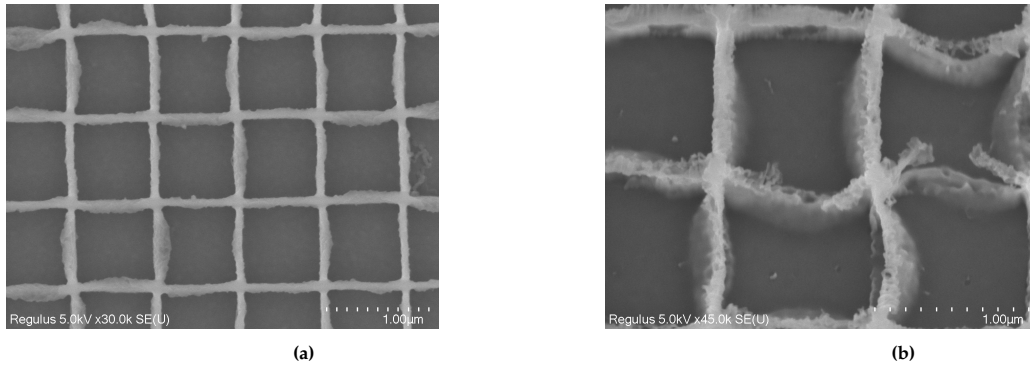


**Figure 5.8:** RIE etching at 75W DC bias after 30s (a) and 2 minutes (b) of etching.

A similar experiment was conducted on the ICP-RIE equipment with similar ions' chemistry but by changing the source power and DC bias process flow condition as shown in the table 5.2, which yielded an etch rate of 1.2  $\mu\text{m}/\text{min}$  into fused silica silicon. [56]. It proceeded to use a similar process to check for any variation. However, after etching for 10s no difference in the sidewall damage was reported as in figure 5.9a. Moreover, based on the cross-sectional SEM image it has a  $\text{SiO}_2$  sidewall height of around 180 nm, considering the 10-degree tilt correction applied to the measured height. Nevertheless, to find out its effect after Si etching, a different process equipment (Cryo etching) was used. Temperature plays a major role in providing good anisotropy and lesser sidewall roughness. It was considered to do the processing at -120 deg C for the Si etching using  $\text{SF}_6$  and  $\text{O}_2$  ions with their respective process conditions according to the parameters mentioned in Table 5.2. The performed etching for 1 minute as showcased in Figure 5.9b has resulted in complete damage to sidewalls, with many hanging  $\text{SiO}_2$  layers. These structures are deemed ineffective for usage as master mold as they tend to collapse when a PDMS layer is cast.

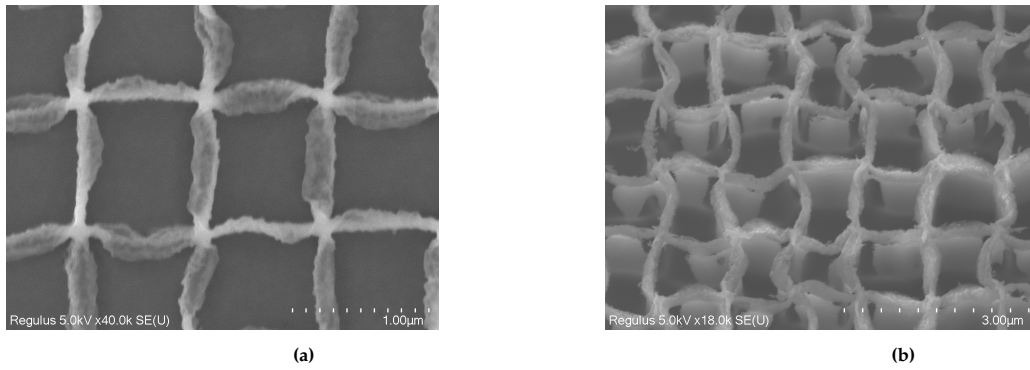


**Figure 5.9:** Inspection of the master mold after SiO<sub>2</sub>(a) and Si (b) etching.

An alternative to casting the PDMS onto the Si master mold is by using the developed e-beam resist as a mold. A similar experiment performed by Pandey [95] indicated that developed e-beam resists can be used as a mold. Considering this, the previously optimized pattern on SiO<sub>2</sub> mask was used as a master mold. Further, this mold will be used to cast the PDMS layer.

### 5.3. Thermal imprinting

For a hot embossing process, the stamp is a crucial component for the replication of patterns onto the substrate. Using hard molds like Si or SiO<sub>2</sub> for this pattern replication onto a thermally curable resist can have significant drawbacks like resist adhesion and non-uniform replication[96]. Due to these issues, soft molds made from siloxane materials are mostly prepared with their ability to overcome the previously mentioned drawbacks and provide nm scale accuracy. Polydimethylsiloxane (PDMS) is the most popular soft mold used for such nano-imprinting applications because of its good elastic properties and its thermal stability upto 200C[96][89]. However, the elastic modulus for PDMS made from Sylgard 184 Dow chemicals, is 2Mpa. During, the imprinting process the mold has to undergo mechanical and capillary forces which might cause severe deformation to mold at such low elasticity [97][95]. To overcome this issue, Schimd[98] developed a siloxane polymer hPDMS that can provide good flexibility and also increase elastic modules to 8Mpa [89].

To check this effect of features being distorted for a critical dimension of < 1µm. The PDMS layer was prepared by mixing the elastomer with a curing agent in a ratio 10:1 and cast on the master mold. After, casting the mold was placed in a curing oven for 2 hours at 100 C. Later, the soft mold is peeled off carefully. The obtained mold showcases a few disorientation (bending of pattern) as shown in figure 5.10. Since such a bending of mold might induce deformities as previously stated due to its low elasticity. To reduce these deformations it was decided to proceed with the preparation of a h-PDMS.

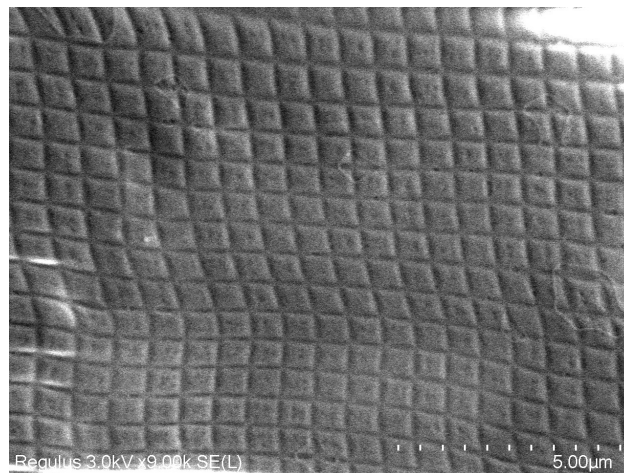


**Figure 5.10:** PDMS mold inspected for a 900 nm periodic pattern

Importantly, before the PDMS layer is cast on the master mold, an anti-sticking layer is necessary. This anti-sticking layer allows for enhancing the demolding of the mold without damaging the patterns. In this work, 1H,1H,2H,2H-perfluorooctyl-trichlorosilane [99] was used for reducing any adhesion between the soft mold and master mold (with resist). This is done by pouring 2 droplets of the solution into a petri dish placed inside a vacuum desiccator. The material has self-assembling characteristics indicating that it can occupy the morphology of the samples used for deposition under a vacuum environment. Leaving the sample inside the vacuum desiccator for 16 hours allows for the creation of the self-assembled monolayer (SAM) layer, where the height of this layer is expected to be around 1-2 nm [100]. Later, this sample is used for depositing the hPDMS.

To improve the properties of soft mold the hPDMS involves mixing chemicals such as 3.4 g of vinyl PDMS pre-polymer (VDT-731, Gelest corp.), 18 uL of platinum catalyst (SIP6831.2 LC, Gelest Corp.) and 5 uL of modulator 2,4,6,8-tetramethyl tetravinylcyclotetrasiloxane (Sigma Aldrich) and adding 1g of hydrosilane polymer (HMS-301). These chemicals are mixed and was spin coated on the master mold at 1000 rpm for 40s. Later, the previously mentioned Sylgard 184 (Dow Inc.) was mixed with a curing agent in 10:1 ratio and cast on the spin-coated master mold. Followed by a degassing process for 20-30 min, longer if needed until all the bubbles are removed. Then the mold is placed in an oven at 60 C for 2 hours. After which the mold is peeled carefully using a razor blade. The transferred patterns are observed to be as shown in Figure 5.11.

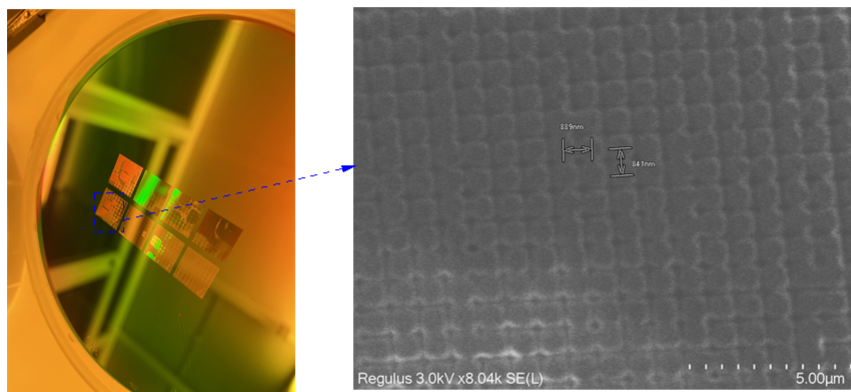


**Figure 5.11:** Inspection of a hPDMS mold (Right) casted from the master mold (Left)

Later, the substrate to be used for creating inverted nano pyramids is spin-coated with a PMMA layer. Since PMMA has good anti-sticking characteristics with the PDMS layer to be used and has a glass transition temperature ( $T_g$ ) ( $108^\circ\text{C}$ )<sup>1</sup> within the thermal limits of PDMS mold. This makes using PMMA suitable for thermal imprinting.[? ]. Further, the PMMA layer is spin-coated using PMMA 950A3 (3 % Anisole) at 4250 rpm for 55s. This allows for the deposition of 100 nm of layer on the Si substrate. To provide a better hardening of the layer, it is pre-baked for 20 minutes at  $175^\circ\text{C}$ . Later, the sample is mounted or loaded into the EVG-501 thermal imprinting equipment with the following procedure mentioned in 3. The substrate was sputtered with 5nm of Gold (Au) to allow for SEM inspection of the pattern replication. The replication turned out to be good as shown in Figure 5.12.

<sup>1</sup>The glass transition temperature ( $T_g$ ) is a crucial parameter that indicates the transition of a solid material into a deformable substance

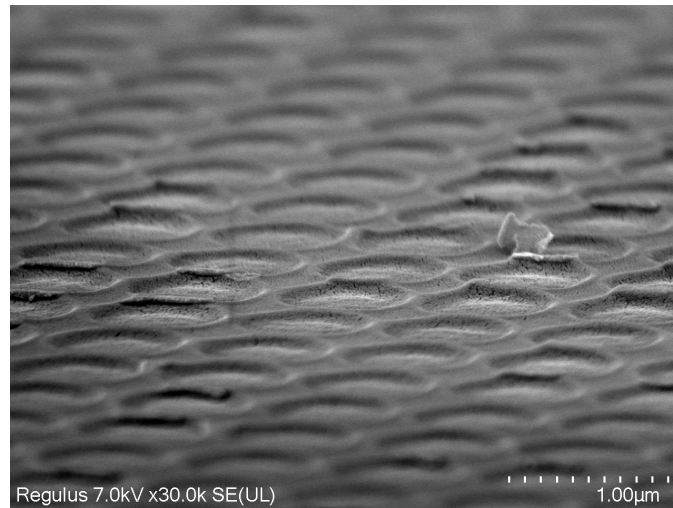


**Figure 5.12:** Inspection of imprinted features onto the substrate after TNIL

Surprisingly, while structures made on the soft mold are circular in shape as shown in Figure 5.11 these were replicated onto the Si substrate as shown in Figure 5.12, those made on the master mold are rectangular. This suggests that the hPDMS was unable to adequately cover the rectangular features, because of the rounded sidewalls present. Their presence is related to the neglected PEC mentioned in Section 3.2 required for adjusting the right dosage to the corners. Failure to do so results in circular patterns, due to inadequate development on the corners of resist. Although these circular patterns can still be utilised to make nano pyramids, such patterns changes should be expected without a PEC.

After the imprinting process, the samples have to undergo a plasma descum process with the mentioned parameters in 5.2 to remove any resist residuals. During the imprinting process, the resist pattern flows through the free space available. This creates a resist wall to be developed, which can act as the mask for subsequent chemical etching. But, the plasma descum process which does involve high ion bombardment induces a chemical reaction with the resist. This can help reduce any ion bombardment on the Si wafer further removing any roughness from being induced. This helps in the deposition of the subsequent support layer like a-Si:H and doping layers with high quality on the Si substrate.

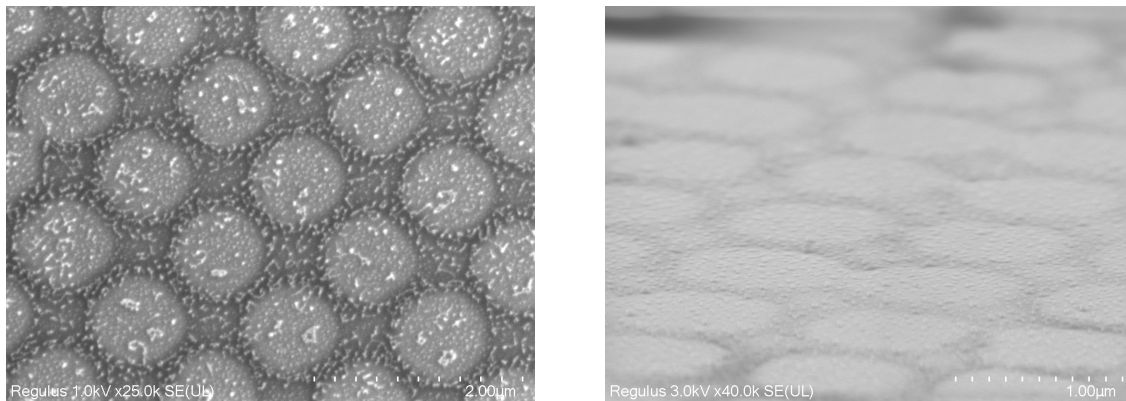


**Figure 5.13:** Plasma descum process performed for 5s on the Si substrate top-view (left) and Cross-sectional (Right).

Usually, resists are not equipped as masks in inorganic chemical processing techniques. But, resists that undergo such plasma processing become hard enough and difficult to be removed by wet-chemical processing techniques. Based on this reason it was experimented to find out if resist can act as a mask withstanding the texturing chemical solution (KOH or TMAH).

After the patterns were successfully replicated onto the resist layer on Si substrates, a 5-second plasma descum process was carried out. The analysis of the pattern that followed produced the findings shown in Figure 5.13. These images demonstrated that very little resist was present across the surface,



implying that the planned wet chemical etching process would be insignificant. Contrary to expectations, the wafer did, in fact, exhibit a recognizable diffraction pattern. This indicates that a recognizable 2D periodic pattern is still prevalent on the wafer, which could be due to the slight periodic grating still present as shown in Figure 5.13. Further, the question of whether the resist could withstand the subsequent chemical processing became evident as a result. Therefore, the wafers were etched for 5 minutes in a 0.7% KOH solution. The results showed that the wafer lacked a diffraction pattern as shown in Figure 5.14 and did not create an inverted pyramid.

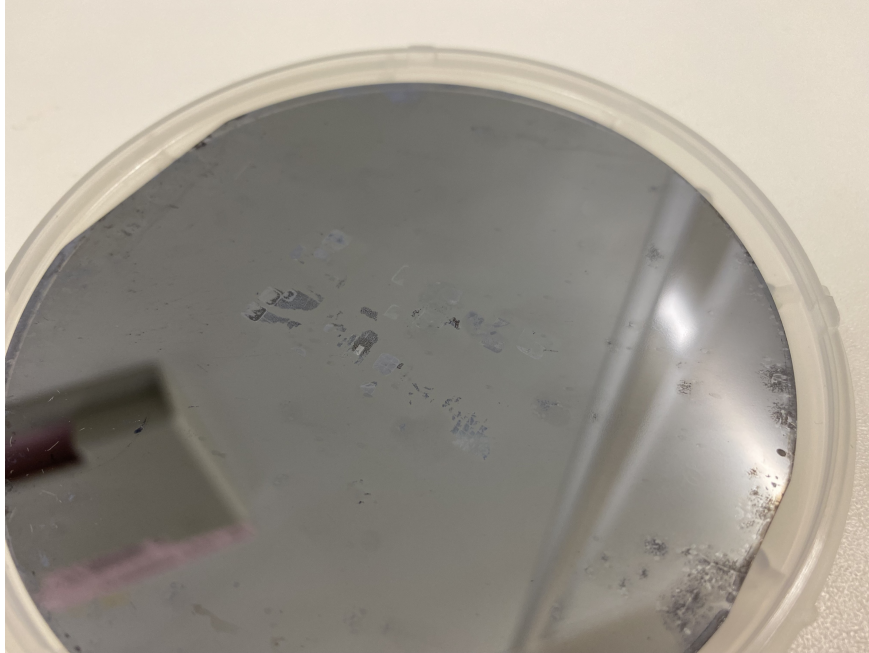


**Figure 5.14:** Lack of diffraction pattern on the Si substrate after chemical etching

This series of findings emphasizes an important point: resist cannot be utilized as a direct mask on its own. Instead, a hard mask made of  $\text{SiO}_2$  or Cr that is substantially more chemically resistant is required. They also stress the significance of optimizing relevant RIE process conditions that can allow for a good opening of the hard mask.

Due to the lack of a functional mask opening that is necessary for the execution of the essential wet chemical for realizing inverted nano pyramids. The established process flow previously indicated could not be fully studied. Given this restriction, it is crucial to evaluate the aforementioned experiments. Which can allow for reliable replication of pattern structures. Fortunately, the results from creating a soft mold and successfully replicating a pattern using nano-imprinting are trustworthy. These results serve to highlight that the utilization of nano-imprinting offers substantial time-saving advantages in the production of sub-micrometer scale features.



## Conclusions

The technology of monolithic perovskite/SHJ tandem cells offers promising potential for overcoming the theoretical efficiency limit of 29.1%. Since bottom cell texturing provides a further improvement for light trapping and improving the efficiency of the device. However, realizing this texturing causes defects in the fabrication of the top cell due to the larger height of the features present. This challenge requires modifying the conventional texturing methods used so far for most single junction devices with new approaches. These techniques should be able to provide uniform texturing and reduced peak height that can allow for uniform deposition of the top cell. Considering this challenge, this thesis has investigated suitable strategies that can allow for the creation of sub-micrometer features. These involved wet-chemical and lithography techniques to achieve such light-trapping features.

### 6.1. Poly-Si etching - Top-Down approach

The first techniques investigated followed a top-down approach where an already textured 180  $\mu\text{m}$  thick CZ wafer was used for experimentation in achieving a texturing height 1  $\mu\text{m}$ . This has been possible through the isotropic chemical processing technique referred to as poly-Si etching. Performing an etching technique at etching times of 6, 11, and 16 minutes provided the peak height reduction to less than 1  $\mu\text{m}$ . However, a deviation in the peak height of 0.3  $\mu\text{m}$  was observed at a lower etching time of 6 minutes. Which indicates the vigorous deviation in etching by the solution at lower Si dissolved or consumed. However, the peak height deviation observed achieved after 11 and 16 minutes of etching is lower. Due to this, it is challenging to achieve reproducibility when using the same solution for consecutive processing at the same etching time. Nevertheless, the obtained features at different etch timing are investigated for reflection comparison. The results indicate that the reflectance increased gradually with etching time, due to the impact of chemical rounding that reduced the mean slope of these features. Also, the depth of craters present is not high enough to provide the necessary light-trapping effect.

Further, it evaluates the effect of subsequent layer deposition on the poly-Si etched wafers. It was revealed that the wafers have a deteriorated minority carrier lifetime without any post-cleaning (PC) techniques implemented. This was also confirmed from the SEM images that the facets of these pyramids have a very high nano-scale roughness. Which eventually impacted the lifetime. Therefore a feasible cleaning technique involving  $\text{HNO}_3$  (99%) and RCA-II were considered. This cleaning technique helped to restore the lifetime back to a level of 224  $\mu\text{s}$ . Despite, his improvement a reasonable roughness scale was present that limited the lifetime again. This indicates that the cleaning technique was not sufficient enough to remove the roughness. Further verifying the similar cleaning strategy for 11 and 16-minute etched samples showcased a decreasing trend. This indicates that passivation layer deposition conditions need to be verified for the poly-Si etched samples, to better understand the deterioration.

But, it was obvious that the poly-Si etching is inducing very high roughness. It requires investigating other chemical methods to remove this. It was found that acetic acid replacing the water in the poly-Si solution can provide a good surface wettability and faster etching rate, suitable characteristics for inducing lesser roughness. First, the AFM measurements were conducted, which also led to a deviation

in the peak height. Hence the main reason behind these deviations could be related to the deterioration of nitrous oxide chemicals when exposed to ambient temperature conditions. Nevertheless, it still provided a height reduction to 1.2  $\mu\text{m}$ . But, most importantly, it succeeded in reducing the effective surface roughness that was previously present. This was also reflected in the minority carrier lifetime measurements when a 1.5-minute etched HNA wafer was tested without any post-cleaning. This wafer yielded a lifetime of 192  $\mu\text{s}$ . Subsequently, apply the post-cleaning technique to 2 2-minute and 3-minute HNA etched wafer. Showcased a decreasing trend in lifetime.

Therefore from these observations, it can be concluded that HNA etching provides the optimal carrier lifetime due to lesser surface-induced defects. But, also the etching time required to provide the essential sub-micrometre height provided the least lifetime. This could be due to the higher surface-induced defects formed by etching it for a longer time or the passivation layer-induced defects. These need to be further analysed to find out the critical reason behind the drop in lifetime at higher etch timing.

## 6.2. KOH +K<sub>2</sub>SiO<sub>3</sub> etching : Bottom up approach

The second technique investigated is a bottom-up approach. Where polished FZ wafers were considered for growing double side sub-micrometre textures. It was found that the addition of K<sub>2</sub>SiO<sub>3</sub> can provide in a reduction in etching rate of pyramids. The initial experiment performed investigating the effect of K<sub>2</sub>SiO<sub>3</sub> with KOH confirmed that a higher K<sub>2</sub>SiO<sub>3</sub> indeed reduced the peak height. But, it also impacts the nucleation or homogeneity of the pyramids. This effect of homogeneity can however be alleviated with the help of surface additives. Where in this thesis a commercially available additive monoTEX (RENA GmbH.) MTH2.6 and MTH3.5 were used. The following experiments were concentrated on verifying this effect, and how it impacts the peak height. Interestingly, the peak height reduced with increasing additive concentration. This is related to the adsorption of additive molecules to the Si surface which limits the reaction of hydroxyl ions (OH<sup>-</sup>). This indeed reflects in the reduced peak height which reduced to 1.3  $\mu\text{m}$  at 5.5% MTH2.6 concentration after 15 minutes of etching.

Further, investigating the effects of a combination of KOH+K<sub>2</sub>SiO<sub>3</sub> and surface additive. It was revealed that at, increasing F-ratio, the etching rate or peak height growth dropped. But, this comes with reduced nucleation at certain instances which was overcome by having increased etching times. But, it should be noted that too long etching time might cause over-etching of pyramids causing distorted pyramids to be present. This was also observed from the optical measurement (reflection) which showcased an increasing reflection after a period of time. Comparing these results with F=0 at 80°C, the pyramids formed at F=0 had a very high nanoscale roughness. This high roughness scale was interpreted to be occurring because of an imbalance between the oxidation and desorption rate of by-products. By decreasing the temperature, it was observed that this rate was restored. This mainly occurred due to the increasing surface additive effect, which removed H<sub>2</sub> bubbles more effectively along with other by-products.

The studies with F=2.0 at 80 ° C ran into a similar problem with byproduct desorption, as there were many un-nucleated regions. In this instance, prolonging the etching time did not result in enough advancement in the nucleation process. This result can be attributable to the observation that the etching rate at F=2.0 was the lowest across all of the trials that were run. As a result, there aren't as many OH<sup>-</sup> ions available to support the oxidation process. Pyramid formation was also observed to have reduced by the Si surface being affected by the adsorption of several other ions or molecules. A comparable finding was made earlier with F=0, when it was apparent that a drop in temperature increased the overall effectiveness of the surface additive. This pattern continued in this instance as well. Therefore, by lowering the temperature, the surface additive might perform better. This resulted in a significant improvement in the uniformity of the pyramid, which in turn improved the reflectance and light-trapping capabilities. So, it can be inferred from these results that a balance in KOH concentration, F-ratio and surface additive is required to allow for the oxidation rate and desorption to stay in equilibrium.

Therefore, F=2.0 at 70° C provided the optimum results of reduced height and very good nucleation. Since the average height for the wafers etched after 10 minutes was around 300 nm, it provides very good deposition of perovskite top layer. Which usually has a thickness ranging from 0.5 - 1  $\mu\text{m}$ . This texturing strategy was also proven to provide reliable texturing height even of CZ samples, which further helps integrate the experimented process conditions to be applied without many modifications.

However, the subsequent layer deposition like the a-Si:H and other n and p-doped layer is yet to be investigated. Usually, these pyramidal features have an increased surface area which could impact the surface recombination velocity. For this reason, optimization of subsequent layer development needs to be investigated.

### 6.3. Nano imprinting lithography

The final technique, investigated in achieving inverted pyramids features on Si substrate through nano-imprint lithography technique. Compared to the previously performed experiments, these techniques differentiate in terms of creating 2D periodic features that can provide angle-selective scattering at certain wavelengths of light propagation. The process flow defined for this involves using e-beam lithography to expose the photoresist with nano-scale accuracy. This photoresist provides the required structures to be used as a master mold for creating a soft mold. Since hard mold made from SiO<sub>2</sub> and Si suffer from adhesion issues, a soft mold helps to provide a better replication of features without much deformation. However, creating the soft mold from PDMS polymer is not suitable for features < 1  $\mu\text{m}$ . Hence a modified approach involving hPDMS was used. This addition helps to provide a much higher modulus of elasticity and prevents the features replicated from the master mold from staying with less deformation.

Subsequently, these soft molds are employed in the thermal imprinting stage to replicate the intricate features onto Si substrates, which have been spin-coated with a suitable thermally curable resist like PMMA. This replication process was successfully tested on 8 Si substrates and yielded minimal to no deformation of the patterns. This underscores the impressive reusability of the soft mold for numerous wafers, considerably enhancing the throughput of the entire process. This stands in contrast to relying solely on e-beam lithography, a method that can be time-consuming, sometimes requiring hours to complete.

A crucial objective of this study was to investigate whether the photoresist layer could effectively function as a mask for subsequent wet-chemical processing. It's worth noting that in many techniques, hard masks are typically deposited to serve as masks, often necessitating a reactive ion etching (RIE) step to open them up. However, this RIE step introduces a surface roughness due to the ion-bombardment, thereby potentially causing defects in the subsequent deposition of a supporting layer onto a c-Si wafer. Instead, it was proposed to use the plasma descum process for removing the resist residuals in the areas of mask opening. However, it was noted that these resist walls appeared to be insufficient. Because of the poor mask opening, it resulted in no inverted nano-pyramid formation.

The investigation's findings clearly show that photoresist by itself is ineffective for use as a mask in the production of inverted nano pyramids. Because the resist mask gets disoriented as a result of an inorganic chemical reaction that dissolves or removes the resist. Instead, the procedure necessitates thorough research and deposition of more strong hard mask material, such as SiO<sub>x</sub> or Cr. The integration of these additional steps into the process will also necessitate the incorporation of appropriate cleaning procedures to eliminate any induced surface roughness.

Further, the soft mold used in the thermal imprinting step to replicate the features onto the Si substrate with PMMA resist has produced a reliable pattern without many deformations. Moreover, this soft mold prepared was used in the thermal imprinting process nearly 8 times and showcased no deformations on the substrate. This indicates the advantage of using hPDMS with a higher modulus of elasticity for good pattern replication and extended usage.

It's critical to understand that this complex method entails a multi-step procedure that calls for additional understanding and process parameter optimisation. To guarantee the hard mask opens successfully and produces the intended, 2D periodic pattern,. For which the etching parameters must be optimized well.

### 6.4. Outlook

The purpose of the thesis work was to explore appropriate methods for fabricating sub-micrometer pyramids for light trapping. While the lithography technique could not demonstrate the effective formation of these features, some results, such as those from the top-down and bottom-up approaches, exhibited it. In order to address the shortcomings identified in these results, further experiments can be conducted, and these will be covered in this section.

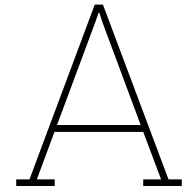
For the top-down approach followed, the optical losses (reflection) higher than a polished wafer. So it requires further evaluation through optical or experimental techniques if these wafers can be implemented into a tandem device to show any light trapping improvements. Moreover, the poly-Si etched and HNA wafers after cleaning and passivation deposition showcased slight bumpiness. Though this has gradually reduced for HNA, it requires further investigation if this is an impact of the deposition condition or wet chemical cleaning techniques. It would also be interesting to implement NAOC cleaning for the poly-Si and HNA etched wafers to understand if there is a reduction in the surface-induced roughness.

The KOH+K<sub>2</sub>SiO<sub>3</sub> etching solution has produced good results in terms of pyramid density and a significantly lower peak height, measuring less than 0.7  $\mu\text{m}$  after 10 minutes of etching at an F-ratio of 2.0. This relatively small peak height is promising because it provides enough coverage for the perovskite layer to deposit. Thus, it becomes necessary to apply appropriate perovskite deposition methods to evaluate whether this arrangement could in reality, result in efficient coverage. Furthermore, these chemical component concentrations have produced similar results on CZ wafers. This implies that it may be possible to investigate the supporting layer deposition process further and improve the production of sub-micrometer textured bottom cells using CZ wafers.

In the last section of this thesis, lithography methods were investigated for the purpose of fabricating inverted nano-pyramids (INPs) on silicon substrates. Finding out whether any of the reactive ion etching (RIE) processes needed for INP manufacturing may be skipped was a crucial component of this study. However, because photoresists are easily etched by inorganic solvents such as TMAH and KOH, experimental results clearly showed that they are not suited as masks for manufacturing INPs. As a result, it was clear that these conditions required a better hard mask, like SiO<sub>2</sub> or a Cr metal layer. [56], [101]

One possible way to overcome the difficulties encountered in the past while attempting to fabricate SiO<sub>2</sub> hard masks via the RIE process, was to change the interspacing distance from 100 nm to 200 or 300 nm. The purpose of this change was to see if a larger interspacing distance could minimize the sidewall damage.

Additionally, a thinner hard mask could also be a possible solution to lessen the noticeable bowing effect. Minimizing the thickness of the SiO<sub>2</sub> hard mask from 200 nm to 50 nm or perhaps 30 nm will reduce the duration of the etching process and the resist's exposure to ion bombardment. [94]



## Poly-Si etching

Poly-etching	1.5 minutes		
	<i>Average</i>	<i>Std. Deviation</i>	<i>Std.Error</i>
Peak height	2.0326	0.24364	0.140668
RMS roughness	298.6	36.936	21.3252
Mean slope	31.8	4.79	2.7667

**Table A.1:** Morphological parameters for a 1.5 minutes poly-etched sample

Poly-etching	6 minutes		
	<i>Average</i>	<i>Std. Deviation</i>	<i>Std.Error</i>
Peak height	1.431333	0.282364	0.163023
RMS roughness	210	19.67232	11.35782
Mean slope	21.73333	4.631774	2.674156

**Table A.2:** Morphological parameters for a 6 minutes poly-etched sample

Poly-etching	11 minutes		
	<i>Average</i>	<i>Std. Deviation</i>	<i>Std.Error</i>
Peak height	1.02	0.172522	0.099606
RMS roughness	172	36.86462	21.2838
Mean slope	11.66667	0.763763	0.440959

**Table A.3:** Morphological parameters for a 11 minutes poly-etched sample

Poly-etching	16 minutes		
	<i>Average</i>	<i>Std. Deviation</i>	<i>Std.Error</i>
Peak height	0.851	0.044396	0.025632
RMS roughness	125.3333	7.023769	4.055175
Mean slope	8.903333	1.005999	0.580814

**Table A.4:** Morphological parameters for a 16 minutes poly-etched sample

<b>HNA-etching</b>	<b>1.5 minutes</b>		
	<i>Average</i>	<i>Std. Deviation</i>	<i>Std.Error</i>
Peak height	1.68125	0.208578	0.104289
RMS roughness	264	16.99019	8.495097
Mean slope	29.35	0.443471	0.221736

**Table A.5:** Morphological parameters for a 1.5 minutes HNA sample

<b>HNA-etching</b>	<b>2 minutes</b>		
	<i>Average</i>	<i>Std. Deviation</i>	<i>Std.Error</i>
Peak height	1.50175	0.138141	0.06907
RMS roughness	216	17.77639	8.888194
Mean slope	24.35	0.718795	0.359398

**Table A.6:** Morphological parameters for a 2 minutes HNA sample

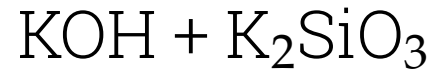
<b>HNA-etching</b>	<b>2.5 minutes</b>		
	<i>Average</i>	<i>Std. Deviation</i>	<i>Std.Error</i>
Peak height	1.413667	0.078143	0.045116
RMS roughness	203.6667	30.43572	17.57207
Mean slope	20.2	2.628688	1.517674

**Table A.7:** Morphological parameters for a 2.5 minutes HNA sample

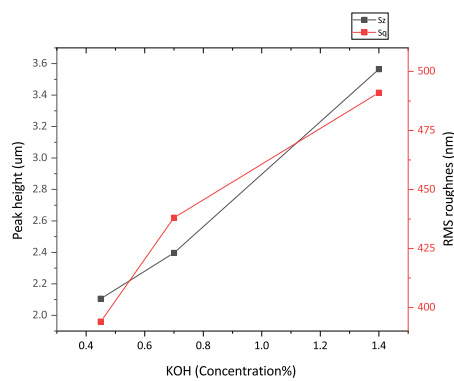
<b>HNA-etching</b>	<b>3 minutes</b>		
	<i>Average</i>	<i>Std. Deviation</i>	<i>Std.Error</i>
Peak height	1.3324	0.103727	0.046388
RMS roughness	209.4	6.107373	2.7313
Mean slope	19.7	2.072438	0.926823

**Table A.8:** Morphological parameters for a 3 minutes HNA sample

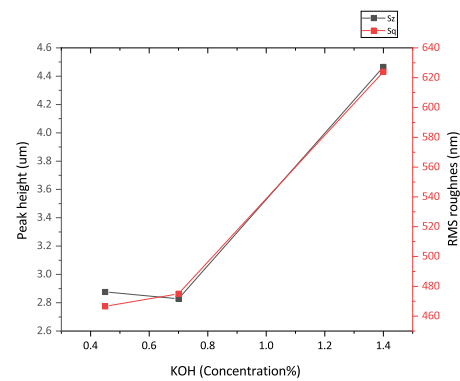
# B



To understand the effects of varying KOH concentration experiments were performed at concentrations of 1.4%, 0.7% and 0.45% at an F-ratio of 2.0 with the surface additive concentration (MTH3.5) being 1% and at 80 °C temperature. The results as indicated in Figure B.1 showcase that at 1.4% KOH concentration the solution has a very high etching rate. Making it less desirable for use in creating sub-micrometer textures. Moreover it would require very high surface additive concentration to reduce the pyramid height. Though KOH = 0.45% provide a similar height as 0.7% concentration, it might also have a lesser impact on the etching rate when more wafers are used. Hence experiemnts were performed at KOH = 0.7%.



(a) Peak height variation after 10 minutes of etching



(b) Peak height variation after 15 minutes of etching

**Figure B.1:** The variation in peak height at different KOH concentration

Further, the peak height variations were conducted at MTH3.5 concetration of 5.5% before changing the solution to MTH2.6. The peak height variations for etching time of 10 and 15 minutes showcase height less than 1 m. This is something similar to what MTH2.6 has showcases in Section 4.2.4

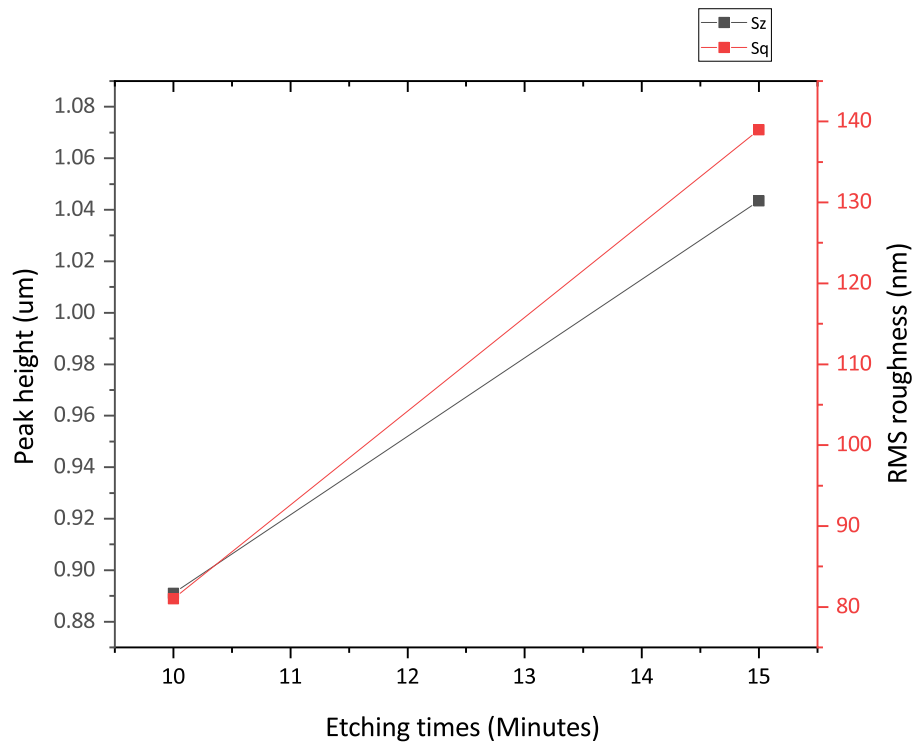
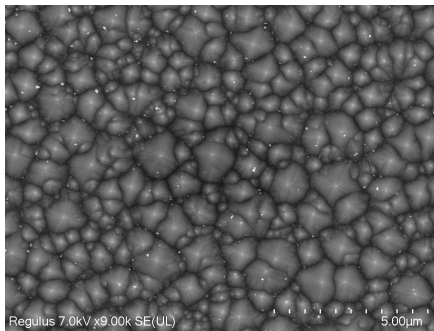
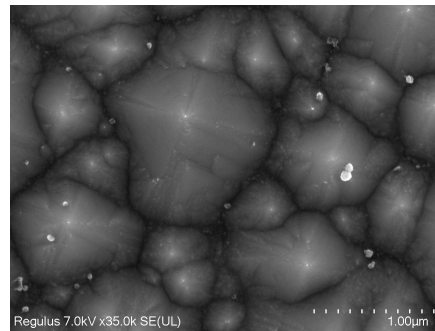


**Figure B.2:** Peak height variation for  $F=0$  at MTH 3.5% surface additive

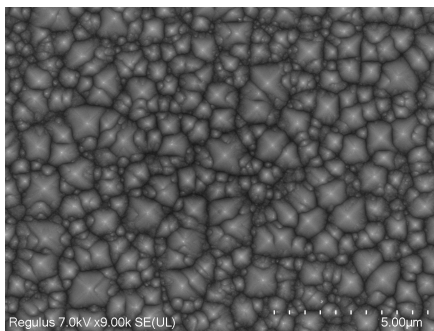


(a) SEM image after 10 minutes of etching.

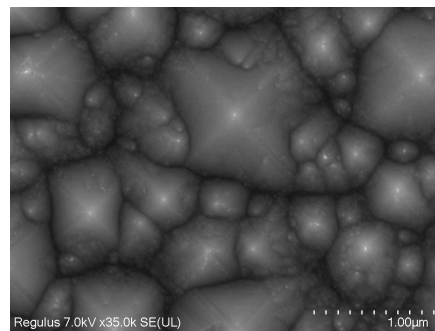


(b) close SEM image after 10 minutes of etching.

**Figure B.3:** SEM characterization of a wafer etched in  $F=1.0$  at  $80^{\circ}\text{C}$  solution



(a) SEM image after 10 minutes of etching.



(b) close SEM image after 10 minutes of etching.

**Figure B.4:** SEM characterization of a wafer etched in  $F=1.0$  at  $80^{\circ}\text{C}$  solution



<b>F=0 at MTH2.6 = 5.5%</b>	<b>Peak height</b>		
	<i>Average</i>	<i>Std. Deviation</i>	<i>Std.Error</i>
5 minutes	1.174	0.08061	0.057
10 minutes	1.236333	0.02687	0.015513
15 minutes	1.3965	0.014849	0.0105
20 minutes	1.51	0.059397	0.042

**Table B.1:** Peak height variation for F=0 at an additive concentration of 5.5%

<b>F=0.5 at MTH2.6 = 5.5%</b>	<b>Peak height</b>		
	<i>Average</i>	<i>Std. Deviation</i>	<i>Std.Error</i>
5 minutes	1.006	0.094652	0.054647
10 minutes	1.209	0.173948	0.123
15 minutes	1.319	0.275772	0.195
20 minutes	1.388	0.152735	0.108

**Table B.2:** Peak height variation for F=0.5 at an additive concentration of 5.5%

<b>F=1.0 at MTH2.6 = 5.5%</b>	<b>Peak height</b>		
	<i>Average</i>	<i>Std. Deviation</i>	<i>Std.Error</i>
5 minutes	0.609	-0.02404	-0.017
10 minutes	0.893	-0.02687	-0.019
15 minutes	1.0915	-0.02333	-0.0165
20 minutes	1.1885	-0.00919	-0.0065

**Table B.3:** Peak height variation for F=1.0 at an additive concentration of 5.5%

<b>F=1.5 at MTH2.6 = 5.5%</b>	<b>Peak height</b>		
	<i>Average</i>	<i>Std. Deviation</i>	<i>Std.Error</i>
5 minutes	0.681333	0.006807	0.00393
10 minutes	0.8415	0.019092	0.0135
15 minutes	0.901	0.007071	0.005
20 minutes	1.01	0.049497	0.035

**Table B.4:** Peak height variation for F=1.5 at an additive concentration of 5.5%

<b>F=2.0 at MTH2.6 = 5.5%</b>	<b>Peak height</b>		
	<i>Average</i>	<i>Std. Deviation</i>	<i>Std.Error</i>
5 minutes	0.487	0.012728	0.009
10 minutes	0.647	0.021213	0.015
15 minutes	0.652	0.042426	0.03
20 minutes	0.682	0.062225	0.044

**Table B.5:** Peak height variation for F=2.0 at an additive concentration of 5.5%

<b>F=0 at 75C and MTH2.6 = 5.5%</b>	<b>Peak height</b>		
	<i>Average</i>	<i>Std. Deviation</i>	<i>Std.Error</i>
5 minutes	0.992	0.084853	0.06
10 minutes	1.245	0.162635	0.115
15 minutes	1.365	0.152735	0.108

**Table B.6:** Peak height variation for F=0 at an additive concentration of 5.5% and 75C temperature

<b>F=0 at 70C and MTH2.6 = 5.5%</b>	<b>Peak height</b>		
	<i>Average</i>	<i>Std. Deviation</i>	<i>Std.Error</i>
5 minutes	0.737	0.048083	0.034
10 minutes	1.0625	0.078489	0.0555
15 minutes	1.0855	0.054447	0.0385

**Table B.7:** Peak height variation for F=0 at an additive concentration of 5.5% and 70C temperature

<b>F=2.0 at 75C and MTH2.6 = 5.5%</b>	<b>Peak height</b>		
	<i>Average</i>	<i>Std. Deviation</i>	<i>Std.Error</i>
5 minutes	0.457	0.034771	0.020075
10 minutes	0.537667	0.07333	0.042337
15 minutes	0.633667	0.027429	0.015836
20 minutes	0.778667	0.014468	0.008353

**Table B.8:** Peak height variation for F=2.0 at an additive concentration of 5.5% and 75C temperature

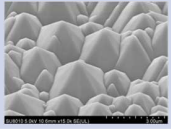
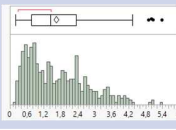
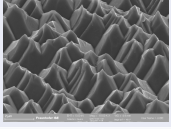
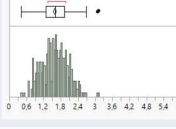
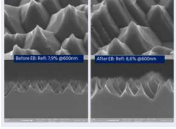
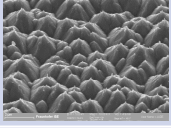
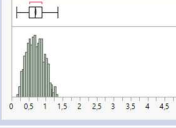
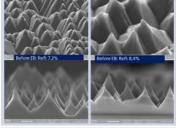
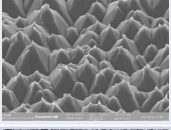
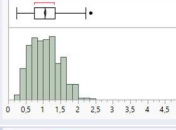
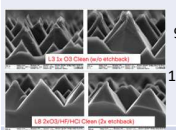
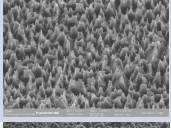
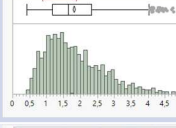
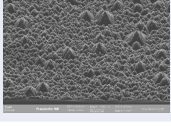
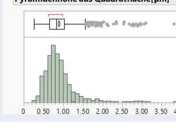
<b>F=2.0 at 70C and MTH2.6 = 5.5%</b>	<b>Peak height</b>		
	<i>Average</i>	<i>Std. Deviation</i>	<i>Std.Error</i>
5 minutes	0.409	0.016523	0.009539
10 minutes	0.606	0.066053	0.038136
15 minutes	0.751	0.057983	0.041
20 minutes	0.667	0.039661	0.022898

**Table B.9:** Peak height variation for F=2.0 at an additive concentration of 5.5% and 75C temperature

# RENA texture-additives comparison summary pyramide size and distribution



## RENA Additives Summary

Additive & Cell types	Reflectivity @600nm	SEM picture	Pyramide Distribution	Pyramide rounding Etchback
monoTex H2.6 PERC HJT	10.6%		 <ul style="list-style-type: none"><li>Pyramid height 1.14-1.47um</li><li>Pyramide per sqr.um = 0.18P/um2</li></ul>	under investigation
monoTex H3.0 TOPCon HJT	9%		 <ul style="list-style-type: none"><li>Pyramid height 1.28-1.61um</li><li>Pyramide per sqr.um = 0.35 P/um2</li></ul>	
monoTex fast MT HJT IBC	7.8%		 <ul style="list-style-type: none"><li>Pyramid height 0.56-0.7um</li><li>Pyramide per sqr.um = 1.49 P/um2</li></ul>	
monoTex H3.7 PERC TOPCon	9%		 <ul style="list-style-type: none"><li>Pyramid height 0.84-1.06um</li><li>Pyramide per sqr.um = 0.84P/um2</li></ul>	 9% Refl. 10% Refl.
monoTex H4.0 TOPCon? HJT?	6%		 <ul style="list-style-type: none"><li>Pyramid height 1.5-1.8um</li><li>Pyramide per sqr.um = 1.65P/um2</li></ul>	under investigation
monoTex H2.6-3 TOPCon? HJT?	8-9%		 <ul style="list-style-type: none"><li>Pyramid height 0.8-0.9 um</li><li>Pyramide per sqr.um = 1.04 P/um2</li></ul>	under investigation

# Bibliography

- [1] T. I. R. E. A. (IRENA), “Renewable power generation costs in 2021,” 2021.
- [2] J. Pastuszak and P. Węgierek, “Photovoltaic cell generations and current research directions for their development,” *Materials*, vol. 15, no. 16, 2022.
- [3] P. B. J. T. Markus Fischer, Michael Woodhouse, “International technology roadmap for photovoltaics (itrpv), 2022 results,” 2023.
- [4] F. Fu, J. Li, T. C. J. Yang, H. Liang, A. Faes, Q. Jeangros, C. Ballif, and Y. Hou, “Monolithic perovskite-silicon tandem solar cells: From the lab to fab?,” *Advanced Materials*, vol. 34, 6 2022.
- [5] H. Lin, M. Yang, X. Ru, G. Wang, S. Yin, F. Peng, C. Hong, M. Qu, J. Lu, L. Fang, C. Han, P. Procel, O. Isabella, P. Gao, Z. Li, and X. Xu, “Silicon heterojunction solar cells with up to 26.81% efficiency achieved by electrically optimized nanocrystalline-silicon hole contact layers,” *Nature Energy*, 5 2023.
- [6] L. C. Hirst and N. J. Ekins-Daukes, “Fundamental losses in solar cells,” *Progress in Photovoltaics: Research and Applications*, vol. 19, no. 3, pp. 286–293, 2011.
- [7] Y. Zhao, K. Datta, N. Phung, A. E. A. Bracesco, V. Zardetto, G. Paggiaro, H. Liu, M. Fardousi, R. Santbergen, P. P. Moya, C. Han, G. Yang, J. Wang, D. Zhang, B. T. van Gorkom, T. P. A. van der Pol, M. Verhage, M. M. Wienk, W. M. M. Kessels, A. Weeber, M. Zeman, L. Mazzarella, M. Creatore, R. A. J. Janssen, and O. Isabella, “Optical simulation-aided design and engineering of monolithic perovskite/silicon tandem solar cells,” *ACS Applied Energy Materials*, vol. 6, no. 10, pp. 5217–5229, 2023.
- [8] Z. C. Holman, A. Descoeudres, S. De Wolf, and C. Ballif, “Record infrared internal quantum efficiency in silicon heterojunction solar cells with dielectric/metal rear reflectors,” *IEEE Journal of Photovoltaics*, vol. 3, no. 4, pp. 1243–1249, 2013.
- [9] J. Werner, B. Niesen, and C. Ballif, “Perovskite/silicon tandem solar cells: Marriage of convenience or true love story? – an overview,” *Advanced Materials Interfaces*, vol. 5, 1 2018.
- [10] P. Tockhorn, J. Sutter, A. Cruz, P. Wagner, K. Jäger, D. Yoo, F. Lang, M. Grischek, B. Li, J. Li, O. Shargaieva, E. Unger, A. Al-Ashouri, E. Köhnen, M. Stolterfoht, D. Neher, R. Schlatmann, B. Rech, B. Stannowski, S. Albrecht, and C. Becker, “Nano-optical designs for high-efficiency monolithic perovskite–silicon tandem solar cells,” *Nature Nanotechnology*, vol. 17, pp. 1214–1221, 11 2022.
- [11] B. Chen, Z. J. Yu, S. Manzoor, S. Wang, W. Weigand, Z. Yu, G. Yang, Z. Ni, X. Dai, Z. C. Holman, and J. Huang, “Blade-coated perovskites on textured silicon for 26Joule,” vol. 4, no. 4, pp. 850–864, 2020.
- [12] F. Sahli, J. Werner, B. A. Kamino, M. Bräuninger, R. Monnard, B. Paviet-Salomon, L. Barraud, L. Ding, J. J. D. Leon, D. Sacchetto, G. Cattaneo, M. Despeisse, M. Boccard, S. Nicolay, Q. Jeangros, B. Niesen, and C. Ballif, “Fully textured monolithic perovskite/silicon tandem solar cells with 25.2% power conversion efficiency,” *Nature Materials*, vol. 17, pp. 820–826, 9 2018.
- [13] A. Harter, S. Mariotti, L. Korte, R. Schlatmann, S. Albrecht, and B. Stannowski, “Double-sided nano-textured surfaces for industry compatible high-performance silicon heterojunction and perovskite/silicon tandem solar cells,” *Progress in Photovoltaics: Research and Applications*, vol. 31, no. 8, pp. 813–823, 2023.

- [14] M. D. Bastiani, R. Jalmood, J. Liu, C. Ossig, A. Vlk, K. Vegso, M. Babics, F. H. Isikgor, A. S. Selvin, R. Azmi, E. Ugur, S. Banerjee, A. J. Mirabelli, E. Aydin, T. G. Allen, A. U. Rehman, E. V. Kerschaver, P. Siffalovic, M. E. Stuckelberger, M. Ledinsky, and S. D. Wolf, "Monolithic perovskite/silicon tandems with 28% efficiency: Role of silicon-surface texture on perovskite properties," *Advanced Functional Materials*, p. 2205557, 12 2022.
- [15] K. Jäger, J. Sutter, M. Hammerschmidt, P.-I. Schneider, and C. Becker, "Prospects of light management in perovskite/silicon tandem solar cells," *Nanophotonics*, vol. 10, no. 8, pp. 1991–2000, 2020.
- [16] T. H. Lane and S. A. Burns, "Silica, silicon and silicones...unraveling the mystery," in *Immunology of Silicones* (M. Potter and N. R. Rose, eds.), (Berlin, Heidelberg), pp. 3–12, Springer Berlin Heidelberg, 1996.
- [17] V. Sverdlov, *Basic Properties of the Silicon Lattice*, pp. 35–44. Vienna: Springer Vienna, 2011.
- [18] A. Smets, K. Jager, O. Isabella, van Swaaij Rene, and M. Zeman, *Solar Energy: The physics and engineering of photovoltaic conversion, technologies and systems*. UIT Cambridge Limited, 2020.
- [19] W. T. Rhodes, T. Asakura, K.-H. Brenner, T. W. Hänsch, T. Kamiya, F. Krausz, B. Monemar, H. Venghaus, H. Weber, and H. Weinfurter, eds., *Physics of Solar Cells*, pp. 11–21. Berlin, Heidelberg: Springer Berlin Heidelberg, 2005.
- [20] S. Cells and Modules, eds., *Solar Cells and Modules*. Springer Series in Materials Science, 2016.
- [21] L. C. Hirst and N. J. Ekins-Daukes, "Quantifying intrinsic loss mechanisms in solar cells: Why is power efficiency fundamentally limited?," vol. 7772, p. 777211, 2010.
- [22] J. Gee, "The effect of parasitic absorption losses on light trapping in thin silicon solar cells," in *Conference Record of the Twentieth IEEE Photovoltaic Specialists Conference*, pp. 549–554 vol.1, 1988.
- [23] B. V. Zeghbroeck, "Chapter-2: Semiconductor fundamentals," *2.8 carrier recombination and generation*, 2020.
- [24] A. W. Ho-Baillie, J. Zheng, M. A. Mahmud, F. J. Ma, D. R. McKenzie, and M. A. Green, "Recent progress and future prospects of perovskite tandem solar cells," *Applied Physics Reviews*, vol. 8, 12 2021.
- [25] S. Akhil, S. Akash, A. Pasha, B. Kulkarni, M. Jalalah, M. Alsaiani, F. A. Harraz, and R. G. Balakrishna, "Review on perovskite silicon tandem solar cells: Status and prospects 2t, 3t and 4t for real world conditions," *Materials Design*, vol. 211, p. 110138, 12 2021.
- [26] X. Y. Chin, D. Turkay, J. A. Steele, S. Tabean, S. Eswara, M. Mensi, P. Fiala, C. M. Wolff, A. Paracchino, K. Artuk, D. Jacobs, Q. Guesnay, F. Sahli, G. Andreatta, M. Boccard, Q. Jeangros, and C. Ballif, "Interface passivation for 31.25%-efficient perovskite/silicon tandem solar cells," *Science*, vol. 381, no. 6653, pp. 59–63, 2023.
- [27] S. Mariotti, E. Köhnen, F. Scheler, K. Sveinbjörnsson, L. Zimmermann, M. Piot, F. Yang, B. Li, J. Warby, A. Musienko, D. Menzel, F. Lang, S. Keßler, I. Levine, D. Manton, A. Al-Ashouri, M. S. Härtel, K. Xu, A. Cruz, J. Kurpiers, P. Wagner, H. Köbler, J. Li, A. Magomedov, D. Mecerreyes, E. Unger, A. Abate, M. Stollerfoht, B. Stannowski, R. Schlattmann, L. Korte, and S. Albrecht, "Interface engineering for high-performance, triple-halide perovskite-silicon tandem solar cells," *Science*, vol. 381, no. 6653, pp. 63–69, 2023.
- [28] D. D. Wolf *KAUST*.
- [29] C. S. Solanki and H. K. Singh, *Principle of Texturization for Enhanced Light Trapping*, pp. 65–82. Singapore: Springer Singapore, 2017.
- [30] P. Campbell and M. A. Green, "Light trapping properties of pyramidally textured surfaces," *Journal of Applied Physics*, vol. 62, no. 1, pp. 243–249, 1987.

- [31] C. S. Solanki and H. K. Singh, *Texturing Process of c-Si Wafers*, pp. 83–97. Singapore: Springer Singapore, 2017.
- [32] C. S. Solanki and H. K. Singh, “Principle of dielectric-based anti-reflection and light trapping,” pp. 43–64, 2017.
- [33] R. Islam and K. Saraswat, “Limitation of optical enhancement in ultra-thin solar cells imposed by contact selectivity,” *Scientific Reports*, vol. 8, 12 2018.
- [34] A. Ingenito, O. Isabella, and M. Zeman, “Experimental demonstration of 4n<sup>2</sup> classical absorption limit in nanotextured ultrathin solar cells with dielectric omnidirectional back reflector,” *ACS Photonics*, vol. 1, no. 3, pp. 270–278, 2014.
- [35] F. J. Haug, M. Bräuninger, and C. Ballif, “Fourier light scattering model for treating textures deeper than the wavelength,” *Opt. Express*, vol. 25, pp. A14–A22, Feb 2017.
- [36] B. Chen, Z. J. Yu, S. Manzoor, S. Wang, W. Weigand, Z. Yu, G. Yang, Z. Ni, X. Dai, Z. C. Holman, and J. Huang, “Blade-coated perovskites on textured silicon for 26%-efficient monolithic perovskite/silicon tandem solar cells,” *Joule*, vol. 4, pp. 850–864, 4 2020.
- [37] K. Jäger, J. Sutter, M. Hammerschmidt, P. I. Schneider, and C. Becker, “Prospects of light management in perovskite/silicon tandem solar cells,” *Nanophotonics*, vol. 10, pp. 1991–2000, 6 2021.
- [38] O. Isabella, “Light management in thin-film silicon solar cells,” 2013.
- [39] B. Bläsi, M. Hanser, K. Jäger, and O. Höhn, “Light trapping gratings for solar cells: an analytical period optimization approach,” *Optics Express*, vol. 30, p. 24762, 7 2022.
- [40] K. Jäger, C. Barth, M. Hammerschmidt, S. Herrmann, S. Burger, F. Schmidt, and C. Becker, “Simulations of sinusoidal nanotextures for coupling light into c-si thin-film solar cells,” *Opt. Express*, vol. 24, pp. A569–A580, Mar 2016.
- [41] K. Nojiri, *Mechanism of Dry Etching*, pp. 11–30. Cham: Springer International Publishing, 2015.
- [42] S. Franssila and L. Sainiemi, *Reactive Ion Etching (RIE)*, pp. 1772–1781. Boston, MA: Springer US, 2008.
- [43] M. J. Walker, “Comparison of Bosch and cryogenic processes for patterning high-aspect-ratio features in silicon,” vol. 4407, pp. 89 – 99, 2001.
- [44] J. Ramanujam and A. Verma, “Photovoltaic properties of a-si:h films grown by plasma enhanced chemical vapor deposition: A review,” *Materials Express*, vol. 2, pp. 177–196, 9 2012.
- [45] W. G. J. H. M. van Sark, L. Korte, and F. Roca, eds., *Physics and Technology of Amorphous-Crystalline Heterostructure Silicon Solar Cells*, vol. 0. Springer Berlin Heidelberg, 2012.
- [46] D. Deligiannis, “Surface passivation for silicon heterojunction solar cells0,” *TU Delft Repositories*, Jul 2017.
- [47] Y. Zhao, P. Procel, A. Smets, L. Mazzarella, C. Han, G. Yang, L. Cao, Z. Yao, A. Weeber, M. Zeman, and O. Isabella, “Effects of (i)a-si:h deposition temperature on high-efficiency silicon heterojunction solar cells,” *Progress in Photovoltaics: Research and Applications*, 2022.
- [48] M. W. Lamers, K. T. Butler, J. H. Harding, and A. Weeber, “Interface properties of a-sinx:h/si to improve surface passivation,” *Solar Energy Materials and Solar Cells*, vol. 106, pp. 17–21, 2012. SiliconPV.
- [49] G. Paggiaro, “Optimizations of high-efficiency silicon heterojunction solar cells for tandem applications,” *TU Delft Repositories*, Oct 2022.
- [50] A. Sarangan, “5 - nanofabrication,” in *Fundamentals and Applications of Nanophotonics* (J. W. Haus, ed.), pp. 149–184, Woodhead Publishing, 2016.



- [51] Y. Nishimoto, T. Ishihara, and K. Namba, "Investigation of acidic texturization for multicrystalline silicon solar cells," *Journal of The Electrochemical Society*, vol. 146, p. 457, feb 1999.
- [52] R. White Tanner Eda L-Edit (layout editor) - Tufts university, Oct 2023.
- [53] T. Groves, "3 - electron beam lithography," in *Nanolithography* (M. Feldman, ed.), pp. 80–115, Woodhead Publishing, 2014.
- [54] T. D. Kavli Institute of nanoscience, "E-beam lithography and cad documentation," 2023.
- [55] D. Resnick, "9 - nanoimprint lithography," in *Nanolithography* (M. Feldman, ed.), pp. 315–347, Woodhead Publishing, 2014.
- [56] M. Ganjian, K. Modaresifar, D. Rompolas, L. E. Fratila-Apachitei, and A. A. Zadpoor, "Nanoimprinting for high-throughput replication of geometrically precise pillars in fused silica to regulate cell behavior," *Acta Biomaterialia*, vol. 140, pp. 717–729, 2022.
- [57] Y. Zhang, B. Wang, X. Li, Z. Gao, Y. Zhou, M. Li, D. Zhang, K. Tao, S. Jiang, H. Ge, S. Xiao, and R. Jia, "A novel additive for rapid and uniform texturing on high-efficiency monocrystalline silicon solar cells," *Solar Energy Materials and Solar Cells*, vol. 222, p. 110947, 4 2021.
- [58] I. Zubel and M. Kramkowska, "The effect of isopropyl alcohol on etching rate and roughness of (1 0 0) si surface etched in koh and tmah solutions," *Sensors and Actuators A: Physical*, vol. 93, no. 2, pp. 138–147, 2001.
- [59] H. Seidel, L. Csepregi, A. Heuberger, and H. Baumgärtel, "Anisotropic etching of crystalline silicon in alkaline solutions: I. orientation dependence and behavior of passivation layers," *Journal of The Electrochemical Society*, vol. 137, p. 3612, nov 1990.
- [60] E. Vazsonyi, K. De Clercq, R. Einhaus, E. Van Kerschaver, K. Said, J. Poortmans, J. Szlufcik, and J. Nijs, "Improved anisotropic etching process for industrial texturing of silicon solar cells," *Solar Energy Materials and Solar Cells*, vol. 57, no. 2, pp. 179–188, 1999.
- [61] P. Pal, V. Swarnalatha, A. V. Rao, A. K. Pandey, H. Tanaka, and K. Sato, "High speed silicon wet anisotropic etching for applications in bulk micromachining: A review," *Micro and Nano Systems Letters*, vol. 9, no. 1, 2021.
- [62] S.-Y. Lien, C.-H. Yang, C.-H. Hsu, Y.-S. Lin, C.-C. Wang, and D.-S. Wu, "Optimization of textured structure on crystalline silicon wafer for heterojunction solar cell," *Materials Chemistry and Physics*, vol. 133, no. 1, pp. 63–68, 2012.
- [63] A. S. Kale, W. Nemeth, H. Guthrey, M. Page, M. Al-Jassim, D. L. Young, S. Agarwal, and P. Stradins, "Modifications of textured silicon surface morphology and its effect on poly-si/siox contact passivation for silicon solar cells," *IEEE Journal of Photovoltaics*, vol. 9, no. 6, pp. 1513–1521, 2019.
- [64] H. Angermann, "Passivation of structured p-type silicon interfaces: Effect of surface morphology and wet-chemical pre-treatment," *Applied Surface Science*, vol. 254, no. 24, pp. 8067–8074, 2008. V International Workshop on Semiconductor Surface Passivation.
- [65] H. Angermann, J. Rappich, L. Korte, I. Sieber, E. Conrad, M. Schmidt, K. Hübener, J. Polte, and J. Hauschild, "Wet-chemical passivation of atomically flat and structured silicon substrates for solar cell application," *Applied Surface Science*, vol. 254, no. 12, pp. 3615–3625, 2008. Special Issue on Solid State Surfaces and Interfaces.
- [66] D. Deligiannis, S. Alivizatos, A. Ingenito, D. Zhang, M. van Seville, R. A. C. M. M. van Swaaij, and M. Zeman, "Wet-chemical treatment for improved surface passivation of textured silicon heterojunction solar cells," *Energy Procedia*, vol. 55, pp. 197–202, 2014. Proceedings of the 4th International Conference on Crystalline Silicon Photovoltaics (SiliconPV 2014).
- [67] A. Martin, M. Baeyens, W. Hub, P. Mertens, and B. Kolbesen, "Alkaline cleaning of silicon wafers: additives for the prevention of metal contamination," *Microelectronic Engineering*, vol. 45, no. 2, pp. 197–208, 1999.

- [68] H. F. Schmidt, M. Meuris, P. W. Mertens, A. L. P. Rotondaro, M. M. Heyns, T. Q. Hurd, and Z. Hatcher, "H<sub>2</sub>O<sub>2</sub> decomposition and its impact on silicon surface roughening and gate oxide integrity," *Japanese Journal of Applied Physics*, vol. 34, p. 727, feb 1995.
- [69] A. Ul-Hamid, *Components of the SEM*, pp. 15–76. Cham: Springer International Publishing, 2018.
- [70] D. Deligiannis, V. Mariolas, R. Vasudevan, C. C. G. Visser, R. A. C. M. M. van Swaaij, and M. Zeman, "Understanding the thickness-dependent effective lifetime of crystalline silicon passivated with a thin layer of intrinsic hydrogenated amorphous silicon using a nanometer-accurate wet-etching method," *Journal of Applied Physics*, vol. 119, p. 235307, 06 2016.
- [71] Y. T. Cheng, J. J. Ho, S. Y. Tsai, Z. Z. Ye, W. Lee, D. S. Hwang, S. H. Chang, C. C. Chang, and K. L. Wang, "Efficiency improved by acid texturization for multi-crystalline silicon solar cells," *Solar Energy*, vol. 85, pp. 87–94, 1 2011.
- [72] J. Acker, A. Rietig, M. Steinert, and V. Hoffmann, "Mass and electron balance for the oxidation of silicon during the wet chemical etching in hf/hno<sub>3</sub> mixtures," *The Journal of Physical Chemistry C*, vol. 116, no. 38, pp. 20380–20388, 2012.
- [73] M. Steinert, J. Acker, M. Krause, S. Oswald, and K. Wetzig, "Reactive species generated during wet chemical etching of silicon in hf/hno<sub>3</sub> mixtures," *The Journal of Physical Chemistry B*, vol. 110, no. 23, pp. 11377–11382, 2006. PMID: 16771409.
- [74] T. de Vrijer and A. H. Smets, "Advanced textured monocrystalline silicon substrates with high optical scattering yields and low electrical recombination losses for supporting crack-free nano- to poly-crystalline film growth," *Energy Science and Engineering*, vol. 9, pp. 1080–1089, 8 2021.
- [75] R. Santbergen, M. R. Vogt, R. Mishima, M. Hino, H. Uzu, D. Adachi, K. Yamamoto, M. Zeman, and O. Isabella, "Ray-optics study of gentle non-conformal texture morphologies for perovskite/silicon tandems," *Opt. Express*, vol. 30, pp. 5608–5617, Feb 2022.
- [76] K. Singh, M. Nayak, S. Mudgal, S. Singh, and V. K. Komarala, "Effect of textured silicon pyramids size and chemical polishing on the performance of carrier-selective contact heterojunction solar cells," *Solar Energy*, vol. 183, pp. 469–475, 5 2019.
- [77] D. R.B. EE-527: *Microfabrication - Wet etching*.
- [78] C. Chiappini, "Mace silicon nanostructures," pp. 1–21, 2017.
- [79] Y. Li, H. Sai, T. Matsui, Z. Xu, V. H. Nguyen, Y. Kurokawa, and N. Usami, "Nanopyramid texture formation by one-step ag-assisted solution process for high-efficiency monocrystalline si solar cells," *Solar RRL*, vol. 6, 11 2022.
- [80] A. A. A. Omer, Y. Yang, G. Sheng, S. Li, J. Yu, W. Ma, J. Qiu, and W. E. Kolaly, "Nano-texturing of silicon wafers via one-step copper-assisted chemical etching," *Silicon*, vol. 12, pp. 231–238, 1 2020.
- [81] C.-H. Hsu, S.-M. Liu, S.-Y. Lien, X.-Y. Zhang, Y.-S. Cho, Y.-H. Huang, S. Zhang, S.-Y. Chen, and W.-Z. Zhu, "Low reflection and low surface recombination rate nano-needle texture formed by two-step etching for solar cells," *Nanomaterials*, vol. 9, no. 10, 2019.
- [82] C. T. Nguyen, K. Koyama, H. T. Tu, K. Ohdaira, and H. Matsumura, "Texture size control by mixing glass microparticles with alkaline solution for crystalline silicon solar cells," *Journal of Materials Research*, vol. 33, no. 11, p. 1515–1522, 2018.
- [83] P. K. Basu, A. Khanna, and Z. Hameiri, "The effect of front pyramid heights on the efficiency of homogeneously textured inline-diffused screen-printed monocrystalline silicon wafer solar cells," *Renewable Energy*, vol. 78, pp. 590–598, 6 2015.
- [84] P. K. Basu, D. Sarangi, K. D. Shetty, and M. B. Boreland, "Liquid silicate additive for alkaline texturing of mono-si wafers to improve process bath lifetime and reduce ipa consumption," *Solar Energy Materials and Solar Cells*, vol. 113, pp. 37–43, 2013.

- [85] A. Alasfour, Z. J. Yu, W. Weigand, D. Quispe, and Z. C. Holman, "Sub-micrometer random-pyramid texturing of silicon solar wafers with excellent surface passivation and low reflectance," *Solar Energy Materials and Solar Cells*, vol. 218, p. 110761, 2020.
- [86] M. Basher, M. K. Hossain, M. J. Uddin, M. Akand, and K. Shorowordi, "Effect of pyramidal texturization on the optical surface reflectance of monocrystalline photovoltaic silicon wafers," *Optik*, vol. 172, pp. 801–811, 2018.
- [87] J. Sutter, D. Eisenhauer, P. Wagner, A. B. Morales Vilches, B. Rech, B. Stannowski, and C. Becker, "Tailored nanostructures for light management in silicon heterojunction solar cells," *Solar RRL*, vol. 4, no. 12, p. 2000484, 2020.
- [88] M. Li, Y. Chen, W. Luo, and X. Cheng, "Interfacial interactions during demolding in nanoimprint lithography," *Micromachines*, vol. 12, no. 4, 2021.
- [89] L. Guo, "Nanoimprint lithography: Methods and material requirements," *Advanced Materials*, vol. 19, no. 4, pp. 495–513, 2007.
- [90] A. Razzaq, V. Depauw, J. Cho, H. S. Radhakrishnan, I. Gordon, J. Szlufcik, Y. Abdulraheem, and J. Poortmans, "Periodic inverse nanopyramid gratings for light management in silicon heterojunction devices and comparison with random pyramid texturing," *Solar Energy Materials and Solar Cells*, vol. 206, p. 110263, 2020.
- [91] N. Pala and M. Karabiyik, "Electron beam lithography (ebl)," pp. 718–740, 2012.
- [92] R. Hellborg, H. Whitlow, and Z. Yanwen, *Ion Beams in Nanoscience and Technology*. 01 2010.
- [93] M. Zhang and P. Watson, "Reactive ion etching selectivity of si/sio<sub>2</sub>: Comparing of two fluorocarbon gases chf<sub>3</sub> and cf<sub>4</sub>," *ScholarlyCommons*, Mar 2019.
- [94] J. Bobinac, T. Reiter, J. Piso, X. Klemenschits, O. Baumgartner, Z. Stanojevic, G. Strof, M. Karner, and L. Filipovic, "Effect of mask geometry variation on plasma etching profiles," *Micromachines*, vol. 14, no. 3, 2023.
- [95] A. Pandey, S. Tzadka, D. Yehuda, and M. Schwartzman, "Soft thermal nanoimprint with a 10 nm feature size," *Soft Matter*, vol. 15, pp. 2897–2904, 2019.
- [96] J. Chen, C. Gu, H. Lin, and S.-C. Chen, "Soft mold-based hot embossing process for precision imprinting of optical components on non-planar surfaces," *Opt. Express*, vol. 23, pp. 20977–20985, Aug 2015.
- [97] T. W. Odom, J. C. Love, D. B. Wolfe, K. E. Paul, and G. M. Whitesides, "Improved pattern transfer in soft lithography using composite stamps," *Langmuir*, vol. 18, no. 13, pp. 5314–5320, 2002.
- [98] H. Schmid and B. Michel, "Siloxane polymers for high-resolution, high-accuracy soft lithography," *Macromolecules*, vol. 33, no. 8, pp. 3042–3049, 2000.
- [99] H. Sun, J. Liu, P. Gu, and D. Chen, "Anti-sticking treatment for a nanoimprint stamp," *Applied Surface Science*, vol. 254, no. 10, pp. 2955–2959, 2008.
- [100] C. Huang, M. Moosmann, J. Jin, T. Heiler, S. Walheim, and T. Schimmel, "Polymer blend lithography: A versatile method to fabricate nanopatterned self-assembled monolayers," *Beilstein Journal of Nanotechnology*, vol. 3, pp. 620–628, 2012.
- [101] A. P. Amalathas and M. M. Alkaiasi, "Fabrication and replication of periodic nanopyramid structures by laser interference lithography and uv nanoimprint lithography for solar cells applications," in *Micro/Nanolithography* (J. Thirumalai, ed.), ch. 2, Rijeka: IntechOpen, 2018.